All Theses and Dissertations (ETDs)

Winter 1-1-2012

Video-Rate Fluorescence Molecular Tomography for Hand-held and Multimodal Molecular Imaging

Metasebya Solomon
Washington University in St. Louis

Follow this and additional works at: https://openscholarship.wustl.edu/etd

Washington University in St. Louis

School of Engineering and Applied Science

Department of Biomedical Engineering

Thesis Examination Committee:
Samuel Achilefu, chair
Joseph P. Culver, co-chair
Igor R. Efimov
Gregory M. Lanza
Yuan-Chuan Tai
Lihong Wang

Video-Rate Fluorescence Molecular Tomography
for Hand-held and Multimodal Molecular Imaging

by

Metasebya Solomon

A dissertation presented to the
Graduate School of Arts and Sciences
of Washington University in
partial fulfillment of the
requirements for the degree
of Doctor of Philosophy

December 2012

Saint Louis, Missouri

Contents

List of Figures

List of Tables

Acknowledgments

Dedication

To: Dinkenesh Boku.

ABSTRACT OF THE DISSERTATION
Video-rate Fluorescence Molecular Tomography for
Hand-held and Multimodal Molecular Imaging
by
Metasebya Solomon
Doctor of Philosophy in Biomedical Engineering
Washington University in St. Louis, 2012
Research Advisors: Professors Samuel Achilefu and Joseph Culver

Abstract

In the United States, cancer is the second leading cause of death following heart disease. Although, a variety of treatment regimens are available, cancer management is complicated by the complexity of the disease and the variability, between people, of disease progression and response to therapy. Therefore, advancements in the methods and technologies for cancer diagnosis, prognosis and therapeutic monitoring are critical to improving the treatment of cancer patients.

The development of improved imaging methods for early diagnosis of cancer and of near real-time monitoring of tumor response to therapy may improve outcomes as well as the quality of life of cancer patients. In the last decade, imaging methods including ultrasound, computed tomography (CT), magnetic resonance imaging (MRI), single photon emission computed tomography (SPECT), and positron emission tomography (PET), have revolutionized oncology. More recently optical techniques, that have access to unique molecular reporting strategies and functional contrasts, show promise for oncologic imaging

This dissertation focuses on the development and optimization of a fiber-based, video-rate fluorescence molecular tomography (FMT) instrument. Concurrent acquisition of fluorescence and reference signals allowed the efficient generation of ratio-metric data for 3D image reconstruction. Accurate depth localization and high sensitivity to fluorescent

targets were established to depths of >10 mm. In vivo accumulation of indocyanine green dye was imaged in the region of the sentinel lymph node (SLN) following intradermal injection into the forepaw of rats. These results suggest that video-rate FMT has potential as a clinical tool for noninvasive mapping of SLN.

Spatial and temporal co-registration of nuclear and optical images can enable the fusion of the information from these complementary molecular imaging modalities. A critical challenge is in integrating the optical and nuclear imaging hardware. Flexible fiber-based FMT systems provide a viable solution. The various imaging bore sizes of small animal nuclear imaging systems can potentially accommodate the FMT fiber imaging arrays. In addition FMT imaging facilitates co-registering the nuclear and optical contrasts in time. In this dissertation, the feasibility of integrating the fiber-based, video-rate FMT system with a commercial preclinical NanoSPECT/CT platform was established. Feasibility of in vivo imaging is demonstrated by tracking a monomolecular multimodal-imaging agent (MOMIA) during transport from the forepaw to the axillary lymph nodes region of a rat. These co-registered FMT/SPECT/CT imaging results with MOMIAs may facilitate the development of the next generation preclinical and clinical multimodal optical-nuclear platforms for a broad array of imaging applications, and help elucidate the underlying biological processes relevant to cancer diagnosis and therapy monitoring.

Finally, I demonstrated that video-rate FMT is sufficiently fast to enable imaging of cardiac, respiratory and pharmacokinetic induced dynamic fluorescent signals. From these measurements, the image-derived input function and the real-time uptake of injected agents can be deduced for pharmacokinetic analysis of fluorescing agents. In a study comparing

normal mice against mice liver disease, we developed anatomically guided dynamic FMT in conjunction with tracer kinetic modeling to quantify uptake rates of fluorescing agents.

This work establishes fiber-based, video-rate FMT system as a practical and powerful tool that is well suited to a broad array of potential imaging applications, ranging from early disease detection, quantifying physiology and monitoring progression of disease and therapies.

Preface

Chapter 1: Accurate and rapid detection of diseases is of great importance for assessing the molecular basis of pathogenesis, preventing the onset of complications, and implementing a tailored therapeutic regimen. The ability of optical imaging to transcend wide spatial imaging scales ranging from cells to organ systems has rejuvenated interests in using this technology for medical imaging. Moreover, optical imaging has at its disposal diverse contrast mechanisms for distinguishing normal from pathologic processes and tissues. To accommodate these signaling strategies, an array of imaging techniques has been developed. Importantly, light absorption, and emission methods, as well as hybrid optical imaging approaches are amenable to both small animal and human studies. Typically, complex methods are needed to extract quantitative data from deep tissues. This chapter focuses on the development of optical imaging platforms, image processing techniques, and molecular probes, as well as their applications in cancer diagnosis, staging, and monitoring therapeutic response.

Chapter 2: I have developed a fiber-based, video-rate fluorescence diffuse optical tomography (DOT) system for noninvasive *in vivo* sentinel lymph node (SLN) mapping. Concurrent acquisition of fluorescence and reference signals allowed the efficient generation of ratio-metric data for 3D image reconstruction. Accurate depth localization and high sensitivity to fluorescent targets were established in to depths of >10 mm. *In vivo* accumulation of indocyanine green (ICG) dye was imaged in the region of the SLN following intradermal injection into the forepaw of rats. These results suggest that video-rate

fluorescence DOT has significant potential as a clinical tool for noninvasive mapping of SLN.

Chapter 3: Spatial and temporal co-registration of nuclear and optical images can enable the fusion of the information from these complementary molecular imaging modalities. A critical challenge is in integrating the optical and nuclear imaging hardware. Flexible fiber-based fluorescence mediated tomography (FMT) systems provide a viable solution. The various imaging bore sizes of small animal nuclear imaging systems can potentially accommodate the FMT fiber imaging arrays. In addition FMT imaging facilitates co-registering the nuclear and optical contrasts in time. In this chapter, I combine a fiber-based FMT system with a preclinical NanoSPECT/CT platform. Feasibility of *in vivo* imaging is demonstrated by tracking a monomolecular multimodal imaging agent (MOMIA) during transport from the forepaw to the axillary lymph nodes (ALNs) region of a rat.

The fiber-based, video-rate FMT imaging system is composed of 12 sources (785nm and 830nm LDs) and 13 detectors. To maintain high temporal sampling, the system simultaneously acquires ratio-metric data at each detector. A three-dimensional finite-element model derived from CT projections provides anatomically based light propagation modeling. Injection of a MOMIA intradermally into the forepaw of rats provided spatially and temporally co-registered nuclear and optical contrasts. FMT data was acquired concurrently with SPECT and CT. Incorporation of SPECT as a prior in the FMT reconstruction integrated the optical and nuclear contrasts.

Accurate depth localization of phantoms with different thicknesses was accomplished with an average center-of-mass error of 4.1 +/- 2.1 mm between FMT and SPECT

measurements. During in vivo tests, Fluorescence and radioactivity from the MOMIA were co-localized in spatially coincident regions with an average center-of-mass error of 2.68 +/- 1.0 mm between FMT and SPECT for ALNs localization. Intravital imaging with surgical exposure of the lymph node validated the localization of the optical contrast.

The feasibility of integrating a fiber-based, video-rate FMT system with a commercial preclinical NanoSPECT/CT platform was established. These co-registered FMT/SPECT/CT imaging results with MOMIAs may facilitate the development of the next generation preclinical and clinical multimodal optical-nuclear platforms for a broad array of imaging applications, and help elucidate the underlying biological processes relevant to cancer diagnosis and therapy monitoring.

Chapter 4: Dynamic fluorescence imaging is an emerging technology that can provide enhanced non-invasive functional and molecular level detail. Optical tracer kinetic modeling combined with fluorescence dynamic tomography is a non-invasive quantification method that allows extraction of clinically or experimentally relevant parameters related to biological or molecular processes and monitoring their alterations due to pathology. Blood plasma concentration measurement of fluorescence over time is a key tool required for accurate optical tracer kinetic modeling to estimate the relevant and desired parameters. Anatomically guided dynamic fluorescence mediated tomography (DyFMT) provides a viable solution to obtain image derived input function. In this chapter, I demonstrate that video-rate FMT is fast enough to enable imaging of cardiac, respiratory and pharmacokinetic induced dynamic fluorescent signals. From these measurements, the image-derived input function and the

real-time uptake of injected agents can be deduced in normal mice and in mice with experimentally induced liver disease.

Chapter 5: Cancer-related enzyme activity can be detected noninvasively using activatable fluorescent molecular probes. In contrast to "always on" fluorescent molecular probes, activatable probes are relatively non-fluorescent at the time of administration due to intramolecular fluorescence resonance energy transfer (FRET). Enzyme mediated hydrolysis of peptide linkers results in reduced FRET and increased of fluorescence yield. Separation signal from active and inactive probe can be difficult with conventional intensity-based fluorescence imaging. Fluorescence lifetime (FLT) measurement is an alternative method to detect changes in FRET. Thus I investigated FLT imaging for in vivo detection of FRET-based molecular probe activation in an orthotopic breast cancer model. Indeed, the measured FLT of the enzyme-activatable molecular probe increased from 0.62 ns just after injection to 0.78 ns in tumor tissue after 4 hours. A significant increase in FLT was not observed for an "always-on" targeted molecular probe with the same fluorescent reporter. These results show that FLT contrast is a powerful addition to preclinical imaging because it can report molecular activity in vivo due to changes in FRET. Fluorescence lifetime imaging exploits unique characteristics of fluorescent molecular probes that can be further translated into clinical applications including non-invasive detection of cancer-related enzyme activity.

Chapter 1

General Introduction

1.1   Introduction

The application of optical imaging and spectroscopy in medicine and biomedical research has captivated the attention of many scientists, engineers, and clinicians because of the compactness, low cost, and ability of the technology to provide functional and molecular information (Hebden, Arridge and Delpy). In the process of optical imaging, light interaction with biological tissues leads to a number of photophysical events such as absorption, scattering, and emission of light. Each of these events can be utilized to obtain biochemical and morphological information about specific cell or tissue of interest. The diverse contrast mechanisms provided by optical methods constitute the basis of several optical imaging platforms that include spectroscopic, planar, diffuse, and hybrid biomedical optics methods (Tuchin; Vo-Dinh; Wang; Wax and Backman). In fact, the diversity of imaging and therapeutic platform available to researchers is a unique strength of optical technology.

Typically, optical imaging begins with the absorption of light by endogenous or exogenous chromophores to provide contrast between diseased and normal surrounding tissue. In absorption imaging, contrast is generated by the differential concentration of the chromophores in tissues (Niemz; Knappe, Frank and Rohde). The absorbed light can dissipate as heat to surrounding tissue, a phenomenon that is useful in photothermal therapy or photoacoustic imaging (Knappe, Frank and Rohde; Wang). A fraction of the absorbed light can be re-emitted at longer wavelengths than the incident. This emitted light is called autofluorescence if it originates from endogenous chromophores. Autofluorescence is widely used to characterize the metabolic status of tissue. An

2

important example is the classification of tissue as normal or benign and malignant tumors based on the optical properties of flavin adenine dinucleotide (FAD) and reduced nicotinamide adenine dinucleotide (NADH). Autofluorescence imaging and other endogenous fluorophores have easier path to human translation since the signaling biomolecules are naturally produced by the body. The term fluorescence is generally reserved for light emission generated by exogenous contrast agents. This class of optical imaging platform will be discussed in details in several sections below. In a variant of fluorescence imaging, spontaneous light emission can be induced by a biochemical reaction, such as the luciferase-catalyzed oxidation of luciferin (O'Neill et al.; Dothager et al.). This process is termed bioluminescence. Bioluminescence imaging is widely used to unravel the molecular basis of biochemical processes at the molecular levels in cells and small animals. The simplicity of the imaging method, high throughput capability, and the high detection sensitivity and specificity makes this approach attractive for drug development, monitoring treatment response, and molecular interactions in animal models of human diseases. Unfortunately, there is no clear path to human translation in the current state of the technology due to foreign genetic materials (O'Neill et al.; Dothager et al.). In addition to absorption and emission imaging, incident light is highly scattered in heterogeneous media such as tissues. Since light scattering pattern is dependent on tissue morphology, it is used to generate exquisite structural information of target tissues (Wax and Backman). For example, the up-regulation or down-regulation of structural proteins such as collagen can be used to report the invasiveness of tumors and the status of wound healing (Yeh et al.).

Beyond cell and small animal studies, the next frontier is the translation of optical imaging and spectroscopy to humans. Major advances have been made in both instrumentation and tissue-targeted molecular probes that are suitable for human use. These advances promise to change the landscape of conventional diagnostic and treatment monitoring methods (Achilefu; Arridge; Arridge and Hebden; Celli et al.; Erickson and Godavarty; Gibson, Hebden and Arridge; Hebden, Arridge and Delpy; Vo-Dinh). Interestingly, optical imaging has come a long way from the early days of diaphanography, which used simple transillumination light scanning method (Monsees, Destouet and Totty), to modern day diffuse optical tomography and spectroscopy. Unlike diaphanography, which resulted in poor sensitivity in breast cancer detection (58%, based on histologic validation of biopsied samples)(Drexler, Davis and Schofield), new techniques have incorporated state-of-the-art imaging algorithms, highly sensitive detectors, and an array of light sources to delineate scattering from absorption parameters. This approach promises to improve both sensitivity and specificity of current imaging systems in clinics. Several optical imaging methods are already used in clinical practice. Notable among these is optical coherent tomography, which furnishes exceptionally high spatial resolution of tissue structure at microscopic level (Huang et al.; Boppart et al.). The method, which was first introduced for ophthalmologic applications (Swanson et al.), has been expanded to cardiac imaging (Bezerra et al.) and cancer diagnosis (Tearney et al.). Recent studies have also demonstrated the applicability of high-resolution optical fiber-based devices for in vivo characterization of tissues (Badizadegan et al.; Flusberg et al.; VoDinh et al.). Incorporation of this technique into endoscopes will expand their applications to virtually all current endoscopic procedures

and enhance the capabilities of intravital microscopy. Thus, in addition to aiding disease diagnosis, optical imaging is anticipated to be effective in monitoring treatment response in cancer patients (Choe, Corlu, et al.; Kukreti, Cerussi, Tanamai, et al.; Choe).

This chapter focuses on the development of optical imaging platforms, image processing techniques, and molecular probes, as well as their applications for cancer diagnosis, staging, and monitoring therapies. Emphasis is placed on emerging optical methods that are translatable to humans and specific to cancer.

1.2   Optical Contrast Agents

Optical imaging techniques can measure both inherent tissue optical properties (e.g. scattering, absorption and autofluorescence) and those of exogenous molecular probes (e.g. fluorescence, photoacoustic) with high temporal resolution. The spectrally dependent light absorption and propagation properties in tissues (Figure 1.1) based on optical properties of specific molecules are used to produce imaging contrast in optical molecular imaging. A variety of optical contrast agent-mediated optical methods are widely used for preclinical imaging of cancer and monitoring of therapeutic responses.
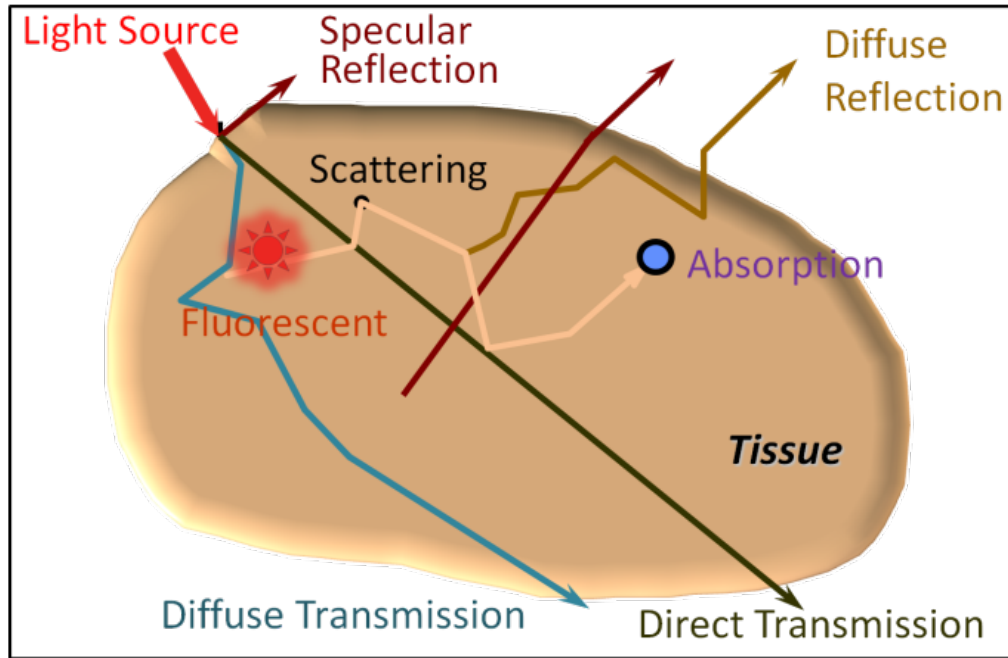
Figure 1.1: Light propagation in turbid medium such as biological tissue.

1.2.1   Endogenous Tissue Optical Contrast

Light interaction with biological tissues results in a number of photophysical events such as its absorption and scattering. Scattering is defined as the deviation of a photon path as it propagates through a heterogeneous medium such as a biological tissue. The most useful approximation describing light scattering in tissue is based on Mie's theory (Tuchin; Wang and Wu; Richards-Kortum and Sevick-Muraca). Mie's scattering relates to the scattering of light by particles of the same or larger size than the wavelength of the incident light. The intensity of Mie scattered radiation is weakly dependent on wavelength and tissue morphology (Tuchin; Wang and Wu). Diffusely reflected and transmitted photons provide diagnostic information about the tissue. For instance, the change in size and number of the major light scatterers in tissue, such as mitochondria and cell nuclei, can be used to differentiate neoplastic from healthy tissues based on the

spectral variation of the scattered light. To illustrate this point, the diameter of cell nuclei in normal epithelial tissues has been found to be approximately 4-7 μm compared to 20 μm in cancerous tissues, which also contain multiple nuclei (Tuchin; Wang and Wu). Hence, scattering properties of tissues provide insight into morphological and structural changes that can be used to identify abnormal variations of the tissue's spatial characteristics. Detailed theoretical basis and practical applications of light scattering in tissues for biomedical imaging has recently been reported (Wax and Backman).

Absorption is a phenomenon that results in the capturing of light energy by chromophores, exciting their electrons from the ground to higher energy levels (Vo-Dinh; Niemz; Tuchin; Wang and Wu). The chromophores dissipate their energy in the form of heat or by a radiative decay when their excited electrons return to the ground state (Wang and Wu; Niemz; Tuchin). Oxy-hemoglobin (HbO2) and deoxyhemoglobin (HbR), melanin, myoglobin, and water are the predominant endogenous absorbers in the 600-1000nm. Interestingly, the absorption coefficient of these chromophores are low between 700 and 900 nm relative to the visible wavelengths, creating an optimal spectral window that allows light to travel in deep tissue and the photons to undergo multiple scattering events before attenuation (Richards-Kortum and Sevick-Muraca; Tuchin; Wang and Wu). For these reasons, most optical methods for deep tissue imaging and diffuse optical tomography in particular, operate in this "transparent optical window".

As mentioned above, variations in total hemoglobin and oxygen saturation can be inferred from tissue absorption based on the differences in oxy-hemoglobin and deoxy-hemoglobin optical spectra. For tumor imaging, high level of HbO2 may suggest an increase in arterial blood supply, creation of new blood supply pathway to tumors, or

high metabolic oxygen demand reminiscent of highly proliferating tumors. In contrast, an increase in HbR concentration implies a decrease in oxygen saturation associated with the presence of hypoxic tumor or high oxygen extraction. Both HbO2 and HbR serve as important biomarkers for tumor diagnosis and monitoring the outcome of a therapeutic intervention. To illustrate this approach, Choe et al. (Choe, Corlu, et al.) demonstrated the feasibility of localizing invasive carcinoma of breast tumor with diffuse optical tomography by quantifying the total hemoglobin and oxy-hemoglobin concentrations. The authors observed that the tumor volume and total hemoglobin concentration decreased from 21.4±1.4 μM to 9.1±0.5 μM over the course of the chemotherapy. A variety of similar studies have been reported and a recent paper by Leff et al. (Leff et al.) summarized the findings of optical-based breast imaging studies from different research groups.

Tissue autofluorescence occurs when excited electrons of endogenous fluorophores emit light of different wavelength after photon absorption (Wang and Wu; Tuchin; Berezin and Achilefu). The importance of autofluorescence for studying cells and tissues lies mostly in their potential for diagnostic applications. It is also used as a research tool to understand the underlying mechanisms of molecular interactions and signaling processes under their native conditions (Berezin and Achilefu; Monici; Richards-Kortum and Sevick-Muraca). The most important fluorophores for autofluorescence in cells and tissues are amino acids (phenylalanine, tyrosine and tryptophan), which are the essential building blocks of proteins and enzymes; nicotinamide and flavins, which regulate cell metabolism; porphyrins, which are responsible for the transport of respiratory gases; structural proteins (collagen and elastin), which are responsible for rigidity and flexibility

8

of tissues and organs; and fluorescent pigments (melanin, lipofuscin), which are markers of many age-related pathologies (Berezin and Achilefu; Monici). For instance, endogenous fluorophores such as flavin adenine dinucleotide (FAD) and reduced nicotinamide adenine dinucleotide (NADH) are used to monitor changes in the metabolic level of tissues by taking the ratio of their fluorescence intensity obtained from one- and two-photon confocal microscopy (Richards-Kortum and Sevick-Muraca) as well as with diffuse spectroscopy (C. Zhu et al.). The fluorescence intensity of NADH is found to be higher than its oxidized form (NAD+), and vice versa for the FAD. However, a number of challenges associated with the complex nature of autofluorescence, such as weak fluorescence signals, the use of damaging UV light or high power two-photon visible excitation, and difficulties in interpretation of images, limits its broad applications in molecular imaging and disease diagnosis. Thus, the use of autofluorescence depends on the intended application or tissue type. For example, skin diseases and a variety of endoscope-based applications that do not require deep tissue analysis have benefited from autofluorescence imaging. Exciting studies using endoscopes for examining gastrointestinal neoplasia in clinical settings have been reported (Imaeda et al.; Falk). Note that fluorophores from diet also contribute significantly to autofluorescence. This type of autofluorescence could increase background signal during tissue imaging with exogenous imaging agents. However, several methods are available to minimize this side effect, including fasting the animal, the use of special diet with low autofluorescence, and techniques to spectrally suppress autofluorescence (Bhaumik, Depuy and Klimash; Bouchard et al.)

9

1.2.2   Exogenous Tissue Contrast Agents

Exogenous contrast agents are playing a crucial role in advancing optical molecular imaging for wide array of applications, ranging from studying cell regulation mechanisms to cancer diagnosis. The advantage of exogenous optical contrast agents lies in the ability to optimize their structure for a wide variety of disease-specific studies. This is generally accomplished by tuning their spectral properties. Optical probes that absorb and emit in the visible spectral range are mainly used for superficial tissue imaging (for example skin cancer detection) and studies of cell mechanisms. However, the signal obtained from optical probes in the visible range is biased by background tissue autofluorescence signal, which is negligible in the NIR spectral range. Therefore, molecular probes in the NIR region are primarily used for deep tissue in vivo imaging and to minimize autofluorescence. Optical contrast agents are classified into different groups based on their fluorophore structure, spectral range, and specific activity. Examples of common optical probes are cyanine dyes, boron-dipyrromethene (BODIPY) based molecules, and quantum dots (Akers and Achilefu; Berezin and Achilefu). The sources of contrast could be due to change in intensity, fluorescence lifetime or polarization associated with biological processes. Preferably, optical molecular probes should have high molar absorptivity, high fluorescence quantum yield (for fluorescence imaging), and good photo-stability. For activatable probes, they should preferably be enzymatically stable to non-target enzymes and biochemical reactions. In addition, chemical stability is important for a new generation of molecular probes carrying targeting groups for selective delivery to tumors. Such targeted conjugates further enhance the sensitivity and specificity of optical contrast agents for early detection of cancer.

1.2.2.1 Non-Targeted Optical Contrast Agents

Non-targeted optical contrast agents typically accumulate in tumors because of increased tumor vascularization and/or leaky blood vessels (Achilefu; S. I. Achilefu et al.; Licha, Hessenius, et al.; Licha, Riefke, et al.). The approved use of the NIR fluorescent dye, indocyanine green (ICG), by the US Food and Drug Administration for non-imaging indications has allowed adoption as non-specific and biocompatible optical imaging agent in humans. Thus, ICG is widely used to test the performance and specifications of optical imaging devices in clinical and preclinical studies. It is also used as a generic imaging agent for cancer imaging. For example, Intes et al. (Intes, Ripoll, et al.) localized suspicious mass in breast cancer patients after bolus administration of ICG. Additionally, Alacam et al. introduced a computational model to analyze ICG pharmacokinetics in cancerous tumors vs. normal tissues using NIR diffuse optical tomography (Alacam, Yazici, Intes, et al.; Alacam, Yazici, Intes, Nioka, et al.). In these studies, the authors provided temporal images of the distribution of ICG from breast cancer patients. Using a computational model, they reported significant difference in the pharmacokinetic rates as well as ICG concentration in the tumor compared to the surrounding normal tissue region. Recently, Sevick-Muraca et al. (Sevick-Muraca et al.) demonstrated the feasibility of employing NIR fluorescence imaging for dynamic lymph trafficking and lymph node mapping in humans non-invasively after bolus injection of ICG in the arms and legs of patients. The impressive dynamic images demonstrated the potential of using optical molecular imaging for sentinel lymph node mapping in cancer staging. However, since non-targeted optical probes suffer from low selectivity for tumors, the use of molecular probes that selectively target cancer tissue, could further

11

improve the information content obtained, particularly in the identification of positive nodes for biopsy.

1.2.2.2 Cancer Biomarkers and Targeted Probes

Many of the current efforts in tumor imaging have focused on the design of cancer-targeting molecular probes. One approach is to identify cancer biomarkers, such as over-expressed proteins or diagnostic enzymes in the tumor and the appropriate molecule (ligand) that binds to a target biomarker with high affinity. Once the biomarkers and the ligands are established, the targeted molecular probe can be prepared by conjugating the targeting moiety to the dye. Cancer biomarker identification is essential for early diagnosis, prognosis and staging of cancers as well as monitoring and optimizing therapies. In general, cancer biomarkers for targeted optical imaging are biomolecules such as cell surface protein receptors or enzymes, which are over-expressed in the active form in neoplasms compared to normal tissues. Many of these biomarkers are commonly shared by a number of malignant tumors (Ludwig and Weinstein; Sidransky). Below I will review two classes of the molecular targeted probes: non activatable and activatable.

Receptor Targeted optical molecular probes. Optical imaging with receptor-targeted molecular probes relies on the increased concentration of the probe on the target tissue to generate increased optical (fluorescence or photoacoustic) signal. Historically, this was the first type of tumor-targeted molecular probes (S. Achilefu, R. B. Dorshow, et al.). Today, a majority of the tumor targeting molecular probes belongs to this class and a large number of the constructs are now commercially available.

Initial studies relied on the labeling of large biomolecules such as antibodies for optical imaging (Ballou et al.; Clauss and Jain). These pioneering studies gave rise to the highly promising advances in the molecular imaging of tumors. For example, the transmembrane tyrosine kinase receptor proteins in which a member of the epidermal growth factor receptor family (EGFR), the human epidermal growth factor receptor 2 (HER-2/neu), is commonly over-expressed has become a favorite target for optical imaging of tumors. The key function of EGFR is intracellular signal transduction to control cell proliferation, migration and cell survival (Ross and Fletcher; Ross, Fletcher, Bloom, Linette, Stec, Symmans, et al.; Nicholson et al.). Up-regulation of HER-2/neu has been associated with tumor growth and metastasis (Ross and Fletcher; Cobleigh et al.). Trastuzumab (also known as Herceptin) is a humanized monoclonal antibody that has high affinity for HER-2 receptors (Ross, Fletcher, Bloom, Linette, Stec, Clark, et al.; Vogel et al.). Therefore, a number of efforts in optical imaging of cancer involved conjugating fluorescent dyes with Trastuzumab to image HER2 positive tumors (Koyama et al.; Sampath et al.).

Although large proteins and antibodies hold great promise for the development of tumor targeting agents with high binding affinity to the target receptor, interest in the use of small peptide-based molecular probes have continued to gain grounds in receptor-targeting imaging platforms. A prominent example is the targeting of somatostatin receptors with fluorescent dye labeled somatostatin peptide analogues such as octreotate (S. Achilefu, H. N. Jimenez, et al.; Licha, Hessenius, et al.). The somatostatin receptor served as a target in whole-body animal imaging study with receptor-targeted NIR fluorescent probe. In this example, a NIR fluorescent dye analogue to ICG but with

conjugatable functionalities, cypate, was covalently linked to octreotate. Using a planar fluorescence reflectance imaging system, the in vivo distribution of the molecular probe in rodents bearing pancreatic acinar carcinomas was obtained (S. Achilefu, R. B. Dorshow, et al.). This study demonstrates the high uptake of the optical molecular probe in the tumor. Since this pioneering study, numerous studies have validated the use of NIR dye-labeled peptides to image tumors in living systems as described below.

Another example of a cancer biomarker that is over-expressed in a wide range of tumors are the $\alpha_v\beta_3$ integrins, which are heterodimeric cell surface proteins composed of one one α and one β transmembrane glycoprotein subunits (Giancotti "Complexity and Specificity of Integrin Signalling"). The key function of integrins is to regulate multiple intracellular signal transduction pathways leading to cell proliferation, differentiation, migration and survival (Giancotti "Integrin Signaling: Specificity and Control of Cell Survival and Cell Cycle Progression"; Giancotti "Complexity and Specificity of Integrin Signalling"; Giancotti and Ruoslahti). The $\alpha_v\beta_3$ integrin is of special interest because it is upregulated in various tumors as well as angiogenic blood vessels (Giancotti "Integrin Signaling: Specificity and Control of Cell Survival and Cell Cycle Progression"; Guo and Giancotti). The $\alpha_v\beta_3$ integrin has high affinity for the naturally occurring proteins/polypeptides possessing Arg-Gly-Asp (RGD) peptide sequence [68]. The utility of a NIR fluorescent probe decorated with RGD peptides in tumor imaging has been reported by many investigators (Achilefu; Haubner et al.; S. Achilefu, S. Bloch, et al.; Ye et al.). Achilefu et al. [70] also discovered that a variant of RGD peptides possessing the GRD peptide sequence labeled with cypate selectively accumulates in $\alpha_v\beta_3$ integrin

14

positive tumor (A549) in nude mice. The study was conducted with a simple planar fluorescence reflectance imaging system. Further microscopic analysis showed that retention of this molecular probe in the tumor correlated with regions of high expression of metabolic indicators such as NADH. Thus, this molecular probe appears to selectively target highly proliferating tumors.

Following by the success of preclinical studies, efforts to move the receptor-targeted optical imaging to humans have increased recently. The highly compartmentalized nature of the gastrointestinal system and the ease of accessing this organ with endoscopes have attracted the first human study of molecular optical imaging of gastrointestinal tumors with a peptide-based exogenous imaging agent (Hsiung et al.). The fluorescein-conjugated peptide construct was developed to bind more strongly to dysplastic colonocytes than to adjacent normal cells and demonstrated 81% sensitivity and 82% specificity. Applications of this approach for image guided intraoperative procedures are also in progress.

Targeted activatable optical contrast agents are mostly designed to interrogate biological processes associated with abnormal protease activities and tissue metabolism. Activatable probes are generally composed of a covalently linked fluorophore pair with different or similar optical properties in close proximity to each other. For Förster or fluorescence resonance energy transfer (FRET) mechanism, the emission spectrum of the donor must overlap with the absorption spectrum of the acceptor (Berezin and Achilefu). In this configuration, the transmission of the excitation energy from the donor to the acceptor dye quenches the fluorescence of the donor (Berezin and Achilefu) decreasing the donor's fluorescence intensity and lifetime (M. Solomon, K. Guo, et al.). Upon

enzymatic cleavage, the two fluorophores separates from each other, resulting in increase of donor's fluorescence intensity and lifetime (M. Solomon, K. Guo, et al.). The amount of energy transfer measured from the fluorescence intensity and fluorescence lifetime of the activatable optical probes can be used to investigate changes in biological processes (Berezin, Lee, Akers, Guo, et al.). Figure 1.2 illustrates the process of FRET probes activation and application in tumor imaging. A number of FRET probes including those optically active in NIR were designed to recover fluorescence after releasing the quencher moiety, which occurs when the probe binds to the active site of diagnostic enzymes (Choe, Konecky, et al.; McIntyre and Matrisian "Molecular Imaging of Proteolytic Activity in Cancer"; McIntyre and Matrisian "Optical Proteolytic Beacons for in Vivo Detection of Matrix Metalloproteinase Activity"; McIntyre, Scherer and Matrisian; Z. Zhang et al.; Paulick and Bogyo).

Abnormally high proteolytic activities of extracellular and intracellular proteases such as matrix metalloprotease (MMP), cathespin and caspase families are found to mediate tumor growth, invasion, and metastasis (Himelstein et al.; McIntyre and Matrisian "Molecular Imaging of Proteolytic Activity in Cancer"; McIntyre and Matrisian "Optical Proteolytic Beacons for in Vivo Detection of Matrix Metalloproteinase Activity"; Fingleton). Particularly, MMPs and cathespin families are involved in basement membrane degradation, leading to local cell invasion and metastasis (Bremer, Tung and Weissleder). The utility of the protease activatable probes for in vivo tumor imaging was first demonstrated by Weissleder et al. (Weissleder et al.). They developed activatable NIR fluorescent molecular probe to localize lung tumor and image the expression and activity of lysosomal proteases. Bremer et al. used this strategy to image the expression

and activity of MMP-2 enzymes in vivo (Bremer, Tung and Weissleder). The study showed recovery of fluorescence after injection of the probe in mice bearing MMP-2 positive human fibrosarcomas. Fluorescence signal from the non-specific control molecular probe was minimal. These and other activatable molecular probes have improved the detection sensitivity of tumors in animal models.

In addition to MMPs, other biomarkers have also been targeted as tumor reporters and for monitoring treatment responses. For example, Blum et al. developed molecular probes that could monitor cathepsin B activity (Blum et al.), which mediates tumor invasion and Gocheva et al. utilized fluorogenic peptides for neo-angiogenesis detection (Gocheva et al.). These studies were conducted with in vivo mouse models of human epithelial adenocarcinoma and pancreatic islet cell carcinogenesis respectively.

Another area of intense research is to monitor treatment response through cell death using activatable probes. Programmed cell death, known as apoptosis, is partly controlled by intracellular caspases. These enzymes are up regulated in cells undergoing apoptosis and studies have shown that disruption of apoptosis results in abnormal cell proliferation and tumor growth. The activities of these proteolytic enzymes have been recognized as important markers for developing imaging and therapeutic agents to non-invasively monitor tumor progress and therapy response (Odonkor and Achilefu "Differential Activity of Caspase-3 Regulates Susceptibility of Lung and Breast Tumor Cell Lines to Paclitaxel"; Odonkor and Achilefu "Modulation of Effector Caspase Cleavage Determines Response of Breast and Lung Tumor Cell Lines to Chemotherapy"; Z. Zhang et al.). For instance, Bullok et al. developed FRET based caspase activatable molecular probe, TcapQ647, composed of fluorescent moiety in

close proximity to NIR fluorescent quencher linked with caspase cleavable peptide sequence (Bullok and Piwnica-Worms; Bullok et al.). The study demonstrated the utility of TcapQ647 for imaging amoeba induced cell death in mice with colon xenografts. They observed a greater increase in parasite-infected xenografts vs. the control after TcapQ647 injection, thus, demonstrating the potential of the compound for monitoring treatment response. An example of caspase-3 activatable probes that are based on FRET between two NIR cyanine dyes connected with caspase-3 cleavable peptide substrate, Asp-Glu-Val-Asp (DEVD), was designed by Zhang et al. (Z. Zhang et al.). Upon contact with caspase-3whose over-expression was induced by the administration of the chemotherapeutic drug (paclitaxel) to A549 tumor bearing mice, cleavage of the DEVD peptide sequence in the fluorescence-quenched probe resulted in the fluorescence restoration.

Although activatable molecular probes have improved the detection sensitivity of tumors in vivo by lowering background fluorescence, they suffer from nonspecific activation in the blood and healthy tissues. Therefore, the development of highly sensitive and specific activatable molecular probes for tumor imaging is an active area of current research endeavors. Efforts to translate some of the probes to humans have been initiated by different research groups.
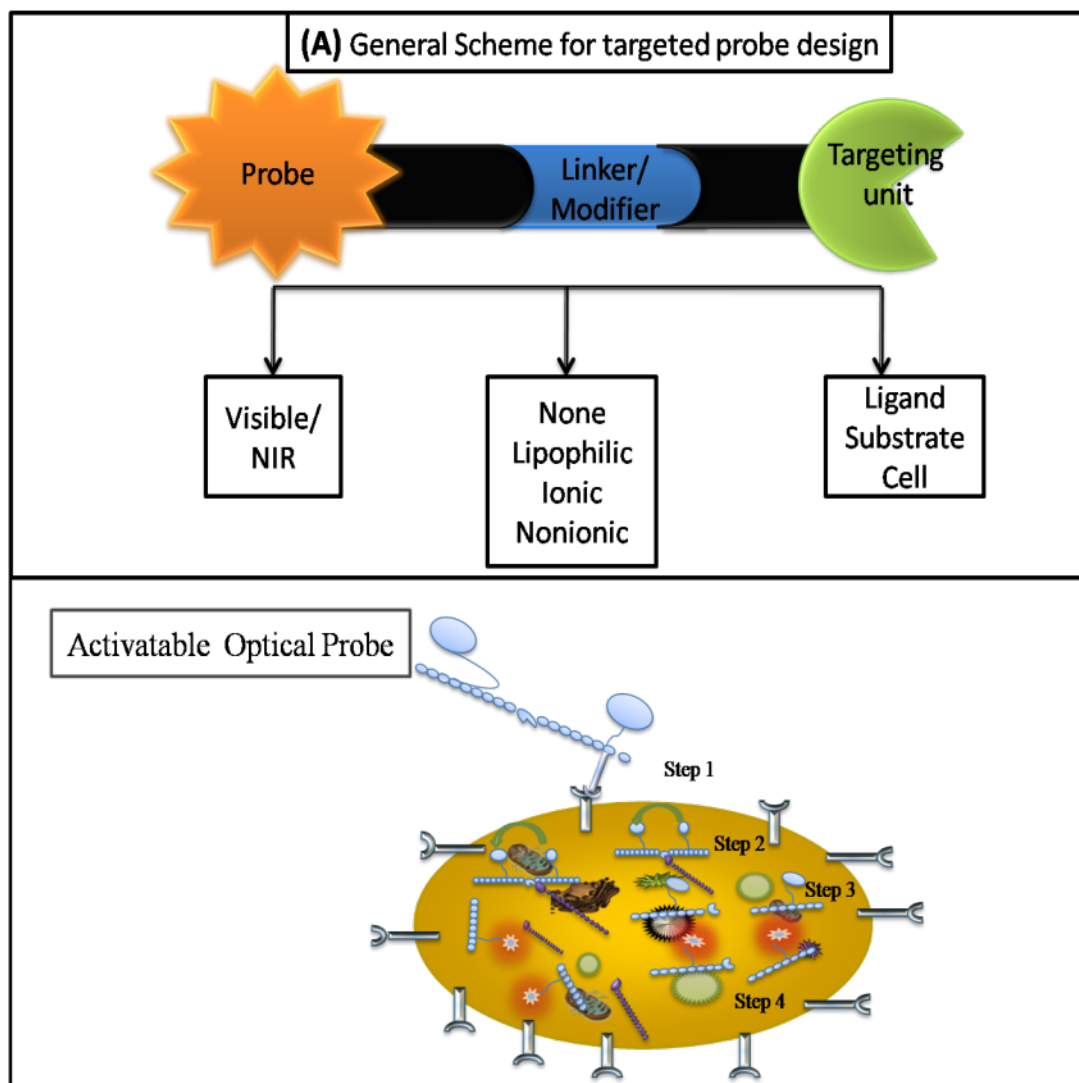
Figure 1.2: Schematic design of targeting non-activatable optical probe (top) and the process of utilizing targeted activatable FRET probe (bottom). Step 1: Internalization of protease activatable molecular probe via a membrane receptor. Step 2: Transmission of the excitation energy from the donor to the acceptor dye quenches the fluorescence of the donor. Step 3 and 4: Recovering of fluorescence after releasing the quencher moiety when the probe binds to the active site of diagnostic enzymes.

1.3   Hardware and Image Reconstruction

Based on the light illumination schemes, optical imaging systems are classified as continuous wave (CW), frequency domain (FD), and time domain (TD) imaging methods with planar, reflectance, or cylindrical modes of measurements (Gibson, Hebden and Arridge; Wang and Wu; Erickson and Godavarty; Vo-Dinh; Xu and Povoski; Tuchin; Hebden, Arridge and Delpy). CW optical imaging platform illuminates tissues with light of constant amplitude or low frequency modulation and detect the light attenuation caused by differential changes associated with the tissue absorption properties. FD imaging platform modulates the light sources at frequencies of tens to hundreds of megahertz and measures the amplitude decay and phase shift of the output light to quantify tissue absorption and scattering properties. TD optical platform detects the temporal distribution of diffuse light (photons) after illuminating the tissue with short light pulses for depth-resolved quantification of the tissue's absorption and scattering properties (Chance et al.; Grosenick et al.; S. Patwardhan et al.). Hybrid imaging methods that utilize light as part of imaging signal generation also use tomographic approaches. For example, in photoacoustic methods, pulsed light is used to generate ultrasound waves from local tissue's thermal expansion following light absorption (Xu and Wang). Each of these techniques will be described in more details below. Representative advantages and limitations of the above techniques are summarized in Table 1.1.

Continous Wave	Time Domain	Frequency Domain
Faster than TD and FD	Quantitative	Quantitative
Accurate for differential measurement of optical properties	High spatial and depth resolution	High spatial and depth resolution
Relatively compact	Recovery of absorption, fluorescence, and scattering properties from temporal impulse response	Faster than TD but less accurate
Less expensive than TD and FD	Accurate than FD but slower	Recovery of absorption, fluorescence, and scattering properties from diffusive wave phase and amplitude

Table 1.1: Comparison of imaging systems techniques.

Reconstruction of optical images requires an understanding of the propagation of light in tissue and is largely based on the knowledge of tissue properties that affect photons and the mathematical algorithms to analyze and classify spectral data. These algorithms help to overcome the tissue's high spatial heterogeneity and identify small differences between normal and cancerous tissues. Reconstruction procedure starts from multiple measurements, where an array of light sources and detectors for a defined geometry are used to generate and detect light. Acquisition of experimental data is followed by the application of a light transport model. This model is based on the propagation of photons in the region of interest. It describes the relationship between tissue optical properties (usually absorption and scattering coefficients) associated with

the relevant pixels and the resulting source-detector measurements (Arridge and Schotland; Arridge; Arridge and Hebden; Arridge and Schweiger; Dehghani et al.). Light transport in biological tissue is typically modeled stochastically by deriving probability functions for photon transitions (Monte Carlo, random walk theory) (Wang, Jacques and Zheng) or deterministically by deriving the diffusion equation from radiative transfer equation (RTE) (Patterson, Chance and Wilson; Arridge and Hebden; Dehghani et al.; Gibson and Dehghani; Wang and Wu). The first method produces more accurate results but it is computationally demanding. Data analysis can range from several hours to several days of computing. The method based on diffusion equation is faster. Therefore it is used more frequently in clinical setting (Schweiger et al.). In both methods, light transport model yields a set of dynamic equations describing the transport of photons as a function of optical properties of the tissue and instrument setting.

After establishing the light transport model, the second step in image reconstruction involves finding a solution to a forward problem (Arridge and Hebden; Gibson, Hebden and Arridge; Dehghani et al.; Arridge and Schweiger; Arridge and Schotland). The forward problem calculates the optical properties of the tissue (absorbance, scattering, or changes in absorption or light attenuation, e.t.c.) as a result of the applied light transport model from step one. Numerical models are commonly used to solve the forward problem and to predict the relationship between the optical parameters for all pixels as a function of the source-detector arrangement. Linear approximations to numerical methods are frequently used to simplify the estimation process (Schweiger et al.; Arridge; Gaudette et al.). The output of the forward problem is typically presented as a sensitivity matrix, where the values obtained from the forward problem are stored.

In the last step, the image is reconstructed by inverting the sensitivity matrix and solving the inverse problem to recover the optical properties of the tissue (Dehghani et al.; Arridge and Schotland; Gibson and Dehghani; Schweiger, Gibson and Arridge). To accomplish this goal, the optimization equation is solved to recover the optical properties of the tissue. The procedure is usually based on a least-squares equation (linear or non-linear) expressing the difference between the measured data and the expected measurements obtained from forward problem solution (Yalavarthy, Pogue, et al.; Yalavarthy, Lynch, et al.). This last step has a number of challenges. In general, the inversion of the matrix and the inverse problem solution is ill-posed because large changes in the model tend to produce only small changes in measurable parameters (real experimental data). Moreover, with the number of pixels larger than the number of measurements, the problem is underdetermined (Boas et al.). Both problems can be resolved with additional parameters known as penalty terms. These terms are added to the least-squares equation restricting the solution and enhancing the image. Basic Tikhonov zero-order regularization (Correia et al.) and more complex functions such as truncated singular value decomposition (TSVD) have been implemented to improve the image quality (Schweiger, Arridge and Nissila; Gaudette et al.; Yalavarthy, Lynch, et al.). The search for the appropriate regularization is in progress in the field of image reconstruction. For detailed information on light transport modeling and image processing, the reader is referred to several extensive reviews on the subject (Arridge and Hebden; Gibson, Hebden and Arridge). The details of the light modeling and reconstruction algorithm implemented on this thesis will be described on each chapter as needed.

1.3.1   Optical Imaging Platforms

This section covers the basic principles of some optical imaging techniques such as planar imaging; diffuse optical spectroscopy, and diffuse optical imaging, with and without the use of exogenous contrast reagents. The roles of these techniques in clinical detection, staging, and treatment monitoring of tumors are briefly described.

1.3.1.1 Planar Imaging

Over the past two decades, optical molecular imaging have benefited from the rapid advances in light sources, detectors, and mathematical modeling techniques. Fluorescence planar imaging is the simplest optical method and it is akin to flash photography. The method is fast and affordable and data analysis is straight forward. The light source required for planar imaging can be as simple as a single white light or a bundle of optical fibers equipped with optical switches (Ntziachristos, Turner, et al.). In its simplest form, appropriate filters are used to select the desired excitation wavelengths from a broad spectrum of light source such as bright light bulbs. More recent versions use CW lasers or light emitting diodes (LEDs) as the light source to provide higher power for deep tissue imaging. The ensuing fluorescence is captured with a charge-coupled device (CCD) camera, the signal is recorded temporally on a computer and displayed on a monitor in near real-time. Planar imaging systems are mostly used to obtain two-dimensional images of tissue in reflectance (epi-fluorescence) or transmission geometry. In transmission geometry, the detector is placed on the opposite side of the excitation source. Most of the commercially available small animal planar imagers utilize the epi-fluorescence mode because of its simplicity and to overcome problems with attenuation of light in thick tissue.

Normally, the images are generated from the recorded intensity of the emitted light in every pixel of the region-of-interest (ROI). Such images show the location of the target fluorescent molecular probe in tissue. However, the images are surface-weighted, resulting in the loss of quantitative accuracy, depth information and poor spatial resolution caused by scattering of the emitted light. Improvement of the reflectance and trans-illumination planar imaging methods can be achieved with data normalization approach (Ntziachristos, Turner, et al.). In this technique, the excitation and emission light intensities are acquired sequentially by switching the interference filter between excitation and emission scans. The normalized image is generated by simply dividing the emission light intensity by the excitation light intensity. The phantom and in vivo studies showed that the normalized data improved the image quality and accuracy as well as the depth sensitivity over non-normalized method (Hyde et al.; Ntziachristos, Bremer and Weissleder; Ntziachristos and Weissleder "Experimental Three-Dimensional Fluorescence Reconstruction of Diffuse Media by Use of a Normalized Born Approximation").

Further improvement in the depth resolution of planar imaging can be achieved by introducing phase profilometry technique into the system. The basic principle of phase surface profile characterization (profilometry) is similar to that of tomographic imaging systems. Both techniques have depth-sectioning ability from the recovered depth information of the imaging object. Implementation of the phase information recovered from the reflected light for 3D image reconstruction was first implemented by Gabor et al. (Gabor). In this method, a spatially modulated intensity sine wave is projected onto the object and imaged with a camera from an offset position (Srinivasan, Liu and

Halioua). The longitudinal distance between a reference plane and the object surface is extracted from the phase distribution at each pixel from multiple sine waves to provide the depth information (Gioux et al.). An alternative approach is to perform a fast Fourier transform using a single intensity sine wave (Takeda and Mutoh). In a typical arrangement, a light source (profilometer laser) and a detector (profilometer camera) are used to create a phase shift. The laser and camera can be synchronized by tilting the platform to further enhance light penetration depth (Gioux et al.). Overall, profilometry and triangulation methods produce good quality 3D images but this comes at the expense of complex hardware and longer processing time. From instrumentation and data analysis point of view, these techniques are closer to tomographic systems than to conventional planar imagers.

1.3.1.2 Diffuse Optical Spectroscopy

Diffuse Optical Spectroscopy (DOS) is the most established optical imaging technique for clinical applications. DOS has been widely used to obtain spectrally dependent functional and structural information by extracting absorption and scattering coefficients associated with concentration changes in endogenous and exogenous fluorophores (Ramanujam et al.; Richards-Kortum and Sevick-Muraca; Sokolov, Follen and Richards-Kortum; Tromberg et al.; Kukreti, Cerussi, Tanamai, et al.; Vishwanath, Klein, et al.). Measurement of hemoglobin absorption in vivo is one of the central approaches in DOS. The absorption spectra of oxy- and deoxy- hemoglobin state differ significantly and the ratio between the two states in tissues is highly conserved. The changes in oxy- and deoxy-hemoglobin concentration often indicate tissue abnormality

and are frequently used to identify physiological problems and follow effects of therapy. In a typical setting, DOS systems are mostly composed of a handheld probe employing a flexible fiber based source-detector configuration. Among a variety of DOS techniques, double-differential spectroscopic analysis and diffuse reflectance spectroscopy are the most common. Double-differential spectroscopic analysis of tissue's absorption and scattering spectra from 650nm to 1000nm has been applied to discriminate normal from cancerous breast tissues. In this method, subtracting the major absorbers' spectral components of normal from cancerous tissues provides patient-specific molecular signature of the tumor (Kukreti, Cerussi, Tromberg, et al.; Kukreti, Cerussi, Tanamai, et al.).

The feasibility of diagnosing tumors and using diffuse reflectance spectroscopy to monitor cancer therapy response by quantifying the associated physiological and morphological changes has also been demonstrated (Vishwanath, Yuan, et al.). To accomplish this goal, the authors extracted the concentration of oxy- and deoxy-hemoglobin, and scattering coefficient by applying inverse Monte Carlo model of light transport to diffuse reflectance spectra collected from tumor bearing mice models (Vishwanath, Yuan, et al.). A significant increase in the concentration of oxy-hemoglobin was observed in doxorubicin treated animals, which implies that diffuse reflectance spectroscopy can be used to monitor treatment response non-invasively.

Palmer et al. utilized hemoglobin based DOS to study physiological changes in response to combinational therapy using hyperthermia and liposomal doxorubicin in a murine model (Palmer et al.). Both diffuse reflectance and fluorescence spectroscopic measurements were performed, allowing multiparametric quantification of optical

properties of tissues and fluorescence of the drug doxorubicin. The study demonstrated that the total hemoglobin saturation increased after treatment. In a human study, Cerussi et al. used DOS to evaluate a patient suffering from infiltrating ductal carcinoma (Cerussi et al.). Here, the patient received a neoadjuvant chemotherapy consisting of anthracyclines and bevacizumab treatments. Instead of directly comparing the tumor water content and deoxy-hemoglobin concentration, a composite tissue optical index, defined as ([deoxy-hemoglobin]x[water])/[lipids] was used to evaluate responses. A decrease of ~50% in the index was found in the course of the chemotherapy, indicating high sensitivity of the index to tumors responding to treatment.

Overall, the results obtained by different research groups demonstrate the capability of DOS to dynamically monitor tumor-associated physiological and morphological changes non-invasively and use the information to identify patients' response, or lack thereof, to chemotherapy (Choe, Corlu, et al.; Choe, Konecky, et al.; Kukreti, Cerussi, Tromberg, et al.; Kukreti, Cerussi, Tanamai, et al.).

1.3.1.3 Diffuse Optical Imaging

Diffuse optical imaging (DOI) method is similar to DOS, but it is more complex due to the use of multiple source-detector combinations for data acquisition and image reconstruction. DOI has been used successfully in a quantitative study of the pharmacokinetics and pharmacodynamics of diagnostic and therapeutic agent, which is also the basis for this thesis work (S. Patwardhan et al.; S. V. Patwardhan, S. Bloch, et al.; Patwardhan and Culver; Ntziachristos, Tung, et al.; Choe, Konecky, et al.; Hebden, Arridge and Delpy).

Diffuse optical tomography (DOT) method produce three-dimensional images of tissue by combining measurements from multiple sources and detectors with light diffusion modeling techniques for depth localization (Vo-Dinh; Gibson, Hebden and Arridge; Wang and Wu; Hebden, Arridge and Delpy). A variant of DOI systems, fluorescence molecular tomography (FMT), acquires excitation and emission light intensity profiles sequentially with interference filter switching between two scans (Ntziachristos, Bremer and Weissleder; Ntziachristos, Tung, et al.; Pogue, Gibbs, et al.). A CCD camera is generally used as detector in this technique. The sequentially acquired excitation and emission light intensities are used to generate normalized data-set from the emission light intensity profile divided by the excitation light for volumetric reconstruction of the fluorescence distribution. Using this approach, Patwardhan et al. developed an FMT system capable of whole-body small animal imaging within a few minutes (S. Patwardhan et al.). The system was successfully used to quantify the biodistribution of targeted fluorescent molecular probes in mice bearing subcutaneously implanted human breast carcinoma.

In addition to reporting the fluorescence intensity, optical imaging systems can be modified to quantify fluorescence lifetime. Fluorescence lifetime is an intrinsic property of endogenous and exogenous fluorophores that relates to the average time a fluorophore remains in the excited state before light emission. Advances in laser technology and instrumentation have led to the development of time-resolved imaging techniques for whole-body imaging of cancer in small animal. This trend has aided the growing interest in developing new FLI systems for tumor imaging (Berezin, Lee, Akers, Guo, et al.; Nothdurft et al.; Bloch et al.; Berezin and Achilefu).

An important advantage of fluorescence lifetime contrast over fluorescence intensity measurements lies in its less dependence on the fluorophore concentration. However, it is generally sensitive to changes in the local tissue environment such as pH, temperature, and presence of fluorescence quenchers (Berezin, Lee, Akers, Guo, et al.; Nothdurft et al.; Bloch et al.; Berezin, Lee, Akers, Nikiforovich, et al.). This sensitivity to differences in tissue composition and biochemistry has been used to differentiate cancerous from normal tissues by fluorescence lifetime imaging (FLI) (Berezin, Lee, Akers, Guo, et al.; Nothdurft et al.; Bloch et al.; Berezin and Achilefu). Cubeddu et al. applied time-domain imaging to localize tumors after fluorescent hematoporphyrin derivative (HpD) uptake used for photodynamic therapy (Cubeddu, Canti, Taroni, et al.; Cubeddu, Canti, Pifferi, et al.). The authors treated L1210 leukemia and fibrosarcoma tumors with hematoporphyrin derivative and observed that the fluorescence lifetime were longer in both tumors than in the surrounding normal tissue. This group also demonstrated that FLI can discriminate between normal and basal cell carcinoma in human skin based on the lifetime differences between protoporphrin IX and normal tissue autofluorescence (Andersson-Engels et al.).

Reynolds et al. used frequency domain for lifetime sensitive detection of molecular probes. They extracted and differentiated NIR contrast agents based on their lifetime differences in tissue mimicking phantoms (Reynolds et al.). The ability to measure multiple fluorescence lifetimes from several fluorescent probes in relatively narrow lifetime range (0.5-1.2 ns) demonstrated the potential of fluorescence lifetime imaging in differentiating cancerous from normal tissues. Most in vivo lifetime imaging studies were confined to specialized laboratories until the commercialization of a time-domain

lifetime imaging system. Bloch et al. demonstrated the feasibility of using receptor-targeted NIR fluorescence molecular probe (cypate-GRD) for non-invasive whole-body fluorescence lifetime imaging with this commercial system (Bloch et al.). The study showed selective localization of the tumor based on the probe's lifetime properties. Further tissue analysis showed that the fluorescence lifetime of the molecular probe was 1.03 ns in tumor and 0.83 ns in the surrounding tissue. Although the lifetime changes appear to be small, modern FLI systems are capable of resolving 0.1 ns lifetimes, making it possible to potentially detect small but significant physiological changes in tumors.

The development of fluorescence lifetime tomography has further enabled improved temporal resolution and accurate tissue localization up to 1 cm depth of targeted tumor using fluorescent molecular probes. Nothdurft et al. developed a fluorescence lifetime tomography system that quantitatively resolves fluorescence lifetimes within the narrow range 0.35 ns and 1.35 ns in vivo (Nothdurft et al.). In this work, targeted exogenous NIR optical probe, cypate-cyclic[RGDfk], was injected into a mammary carcinoma mouse model and the fluorescence lifetime map of whole animal recorded. The tumor was quantitatively differentiated from the surrounding tissue based on the fluorescence lifetime and intensity maps.

Fluorescence lifetime imaging has also enabled imaging of multiple fluorophores with similar absorption and emission spectra but different lifetimes to provide simultaneous information about specific molecular processes without the need for spectral deconvolution of each fluorophore. Reynolds et al. [69], Akers et al. (Akers et al.) and Raymond et al. (Raymond et al.) were able to recover and separate the distribution of two or/and three NIR fluorescent probes that localized in different

organs of mice based on difference of their lifetimes. Their findings suggest that the fluorescence lifetime of different molecular probes can be multiplexed to monitor a variety of molecular interactions through a careful design of NIR fluorescent probes to exhibit lifetime shifts upon target binding. However, one should keep in mind that the difference between individual fluorescence lifetimes must surpass the temporal resolution of the instrument (currently ~100 ps for tomographic systems) to realize lifetime multiplexing.

Overall, optical molecular imaging has the potential to become a powerful and practical tool for a wide array of applications such as noninvasive early detection, image-guided biopsies and intraoperative procedures, and therapeutic monitoring of cancer.

Chapter 2

Video-rate Fluorescence Diffuse Optical Tomography for in vivo Sentinel Lymph Node Imaging

2.1   Introduction

Sentinel lymph node biopsy (SLNB) is the current standard procedure used for prognostic staging of cancers and therapeutic guidance. SLNB is a minimally-invasive procedure that involves the removal of sentinel nodes (the first lymph nodes that receive drainage from the primary tumor) for nodal staging. The location of sentinel lymph nodes (SLNs) is routinely determined by injecting radioactive lymphophilic tracer dye intra-operatively around the tumor region. The lymphophilic tracer is commonly composed of a radioactive colloid and/or optical contrast methylene blue for visual guidance (Tuttle et al.; Hojo et al.). Due to safety issues, a non-invasive and non-ionizing method for imaging of metastatic lymph nodes and lymphangiogenesis would be preferred. Fluorescence diffuse optical tomography (DOT) is an emerging deep tissue (> 3 mm) imaging technique that has great potential as an alternative to radioactive tracer analysis for noninvasive detection and imaging of the sentinel lymph node. While fluorescence DOT often operates on the time scales of minutes to hours, the method also has the potential for imaging at higher speeds above the respiratory and cardiac fluctuations, allowing it to capture pharmacokinetics and pharmacodynamics of diagnostic and therapeutic agents.

Currently, most fluorescence diffuse optical tomography systems are CCD camera-based systems that scan at relatively slow speeds (i.e., frame rates < 0.01 Hz). The slow speed is due in part to the method by which ratio-metric data is acquired. Excitation and emission light intensity profiles are imaged consecutively, which requires that an interference filter for blocking the excitation light to be mechanically inserted between

34

the two scans (Ntziachristos and Weissleder "Charge-Coupled-Device Based Scanner for Tomography of Fluorescent near-Infrared Probes in Turbid Media"; S. V. Patwardhan, S. R. Bloch, et al.; Patwardhan and Culver). Comparison of sequentially acquired excitation and emission light intensities improves image quality through the generation of a normalized ratio-metric data-set (Patwardhan and Culver; Ntziachristos, Turner, et al.). However, the mechanical requirements of sequential scanning slow data collection and pose a challenge for real-time imaging. Alternatively, DOT systems developed to image functional absorption contrast have used time- or frequency-encoding of the illumination with broad spectral detection to image fast activities (> 10 Hz) within the human brain. This style of DOT system replaces the CCD-camera acquisition with multiple photodiode detectors in order to take advantage of the high dynamic range and high speed of avalanche photodiodes (APDs) (Culver, Siegel, et al.; Franceschini and Boas; Zeff et al.). However, the discrete detector DOT approach has not yet been applied to ratio-metric data for fluorescence DOT.

Herein, we aim to improve upon current fluorescence DOT platforms by developing a system with expanded dynamic range and faster data acquisition rates. The video-rate, fiber-based fluorescence DOT system design is built upon a previously published APD-based platform for high-speed DOT (Zeff et al.).

The source-detector grid is designed as a contact probe to pre-operatively identify SLNs near the tumor region after administration of a fluorescent contrast agent. Biopsy of SLNs would follow intra-operatively to enable further histological evaluation for the presence of metastatic cells. These studies with a non-specific, but approved, contrast

agent ICG will set the stage for future work with more specific targeted contrast agents that fluoresce/activate in the presence of metastatic cells.

Fiber-based, video-rate fluorescence DOT could additionally improve the flexibility of imaging by adapting to varying tissue curvatures and performing simultaneous multiple point illumination and collection, thus increasing the imaging frame rate.

In this chapter, I demonstrate the feasibility of in vivo imaging of the dynamics of dye accumulation in the region of the sentinel lymph nodes and quantify the accuracy of depth localization and sensitivity in tissue-simulating phantoms. These results demonstrate that fiber-based, video-rate fluorescence DOT is a practical and powerful tool that is well suited to a wide array of potential imaging applications, ranging from sentinel lymph node mapping to monitoring cancer therapy progression.

2.2   Methods

The generation of ratio-metric (fluorescence-to-reference) data for fluorescence DOT reconstructions has previously relied on sequentially acquired measurements where the source laser is kept at the excitation frequency while a band-pass filter in front of the detector alternates between allowing through excitation and emission (fluorescent) light. The detected excitation light is then used as a reference to normalize the measured fluorescence. The acquisition of such ratio-metric data allows reconstructions using the normalized Born approximation, which can be implemented to quantify fluorochrome distribution. However, while the use of an excitation reference is customary, it is not required. The assumption that light at the excitation wavelength acts as a good reference inherently assumes similar optical properties at the two wavelengths. And, if this

assumption is made, there is no reason why light at the fluorescence wavelength could not be used as a reference. With a CCD-based system, this would be impractical, as there would be no way to determine the difference between the fluorescent and reference light at the same wavelength. However, with APD-based detection, high speed allows the use of frequency-encoding regimens to separate out contributions from different sources. With this encoding scheme, there is no longer any need for the hardware-based temporal-encoding of switching a filter in and out of the light beam. This paradigm is the basis for the system presented here.

The fiber-based, video-rate fluorescence DOT system is composed of an alternating grid of 12 sources and 13 detectors (Figure 2.1). The video-rate fluorescence DOT system uses multimode fiber to carry light from the source box (Figure 2.1 A.1) to the imaging pad (Figure 2.1 A.2) and then to the detector box (Figure 2.1 A.3).
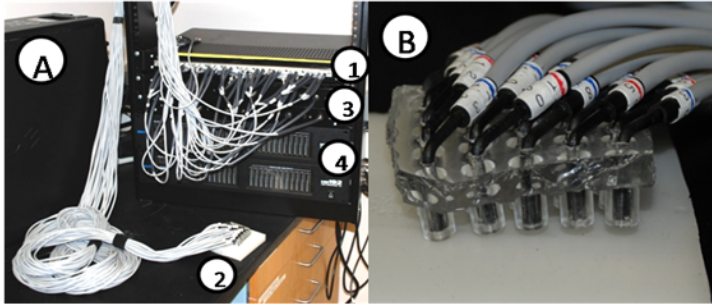
Figure 2.1: Fiber-based, video-rate fluorescence DOT system setup (a) The video-rate fluorescence DOT prototype. Fibers carry light from the source box (1) to the imaging pad (2) then to APDs in two detector boxes (3). The detected signals are digitized by an ADC recording unit (4). (b) A close-up of a 5x5 fiber array.

The source channels contain 785 nm (Thorlabs DL7140-201S) (3.5 mW) and 830 nm (Thorlabs HL8325G) (0.25 mW) laser diodes, with dedicated laser diode drivers and control lines for each source, allowing flexible software configurable source encoding (frequency- and time-encoding) (Figure 2.2 A). Light from the sources is coupled into 2.5 mm diameter fiber bundles. The detection channels use optically-filtered discrete avalanche photodiodes (Hamamatsu C5460-01) digitized with dedicated 24-bit analog-to-digital converters (MOTU HD 192). A narrowband optical filter with center wavelength 830 +/- 10 nm (CVI) and an out-of-band rejection of OD4 separates the excitation light from fluorescent and reference signals. An aspheric lens is used to collimate the light in order to optimize the blocking of excitation light by the narrowband interference filter and enhance fluorescent signal detection. This design provides high instantaneous dynamic range (106) and cross-talk rejection (10-6), so that light levels can be detected over many orders of magnitude. With this scheme, we acquire frequency-encoded fluorescence emission and reference transmission light levels simultaneously at each detector through the individual interference filters optimized for fluorescence emission (Figure 2.2A). All data are acquired at a frame rate of 30 Hz. A total of 108 measurements from source-detector-pairs (also known as optode-pairs) representing the 1st, 2nd, and 3rd nearest-neighbors are used for image reconstruction.
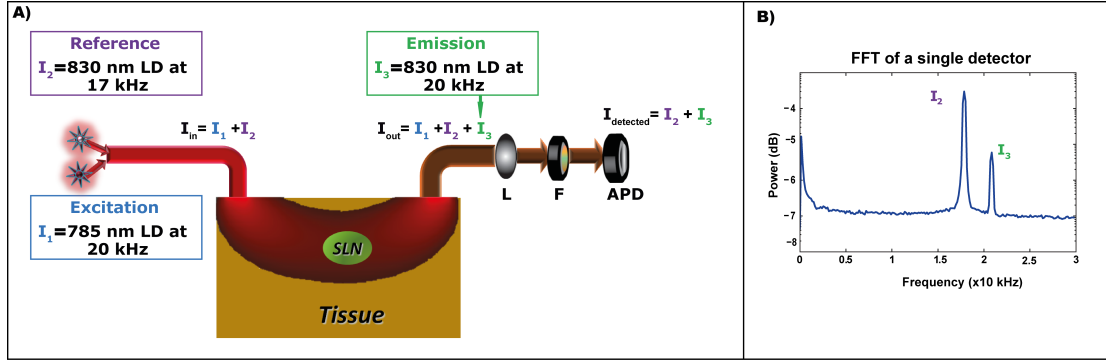
Figure 2.2: Schematic of the video-rate fluorescence DOT hardware. (A) Schematic demonstrating frequency-encoding of 830 nm and 785 nm laser diode sources. Both reference and excitation light (at distinct frequencies) are incident on the tissue. Light exiting consists of reference, excitation, and emission (fluorescent) light. After collimation, the light is passed through a narrow band optical filter (F) to block the excitation light (785 nm). The resulting detected light, a sum of the reference transmission (I_2) and fluorescence emission (I_3), is simultaneously detected by a single detector. (B) A Fourier transform of the sum of I_2 and I_3 provides identification of transmission and emission signals from a single detector.

2.2.1   Ratio-metric Reconstruction

The reference transmission and fluorescent emission light intensities acquired concurrently at each detector (Figure. 2.2B) are used to generate ratio-metric data of fluorescence   divided by reference transmission. The data are then reconstructed using the normalized Born approach to correct for tissue and illumination inhomogeneities, which is written in discrete notation as y=Ax with the following definitions (Zeff et al.).

In the Normalized Born approach: $y_i = \dfrac{\phi_{emi}(r_{s(i)}, r_{d(i)}, \lambda_{emi})}{\phi_{ref}(r_{s(i)}, r_{d(i)}, \lambda_{ref})}$. When the bleed-through of the filter is accounted for then the Normalized Born approach becomes:

$$y_i = \frac{\phi_{emi}(r_{s(i)}, r_{d(i)}, \lambda_{emi}) - \phi_{bleedthrough}(r_{s(i)}, r_{d(i)})}{\phi_{ref}(r_{s(i)}, r_{d(i)}, \lambda_{ref})}$$

The ratio-metric data (y) is generated by measuring the fluorescence light intensity profile $\phi_{emi}(r_{s(i)}, r_{d(i)}, \lambda_{emi})$ at emission wavelength, λ_{emi} , and the reference

transmission light intensity profile, $\phi_{ref}(r_{s(i)}, r_{d(i)}, \lambda_{ref})$, at the reference wavelength , λ_{ref}. The ith source-detector measurement (y$_i$) is associated with source (r$_{s(i)}$) and detector (r$_{d(i)}$) locations.

The bleed-through measurement is made in the absence of a fluorescing agent and measures the amount of light leakage through the filter. It is determined by:

$$\phi_{bleedthrough}(r_{s(i)}, r_{d(i)}) = \alpha \times \phi_{exc}(r_{s(i)}, \lambda_{exc}) = \alpha_{filter}^{d(i)} \times R \times \phi_{ref}(r_{s(i)}, \lambda_{ref});$$

$$where\ R = \frac{\phi_{exc}(r_{s(i)}, \lambda_{exc})}{\phi_{ref}(r_{s(i)}, \lambda_{ref})};$$

α captures the optical density of the filter. In this fiber-based fluorescence DOT system there are individual detectors and sources, and the sources have separate lasers for both reference and excitation. Therefore, the α is calculated separately for each source-detector pairs. To calculate the bleed-through specific to an imaging study, we derived an estimate of the bleed through of ϕ_{emi} based on ϕ_{ref}. Experimentally determined conversion factors (α and R) are used to account for the difference in power level between the excitation and reference lasers. R is measured using a power meter at source fiber tips of each sources and $\alpha_{filter}^{d(i)}$ is the excitation light measured with and without filter, $\phi_{exc}(r_{s(i)}, \lambda_{exc})$, for each detectors at the excitation wavelength (λ_{exc}) of 785 nm.

The sensitivity matrix ($A_{i,j}$) is created using the analytic solutions for photon density in the semi-infinite geometry to obtain the influence of a particular voxel j on every source and detector measurement i.

$$A_{i,j} = -\frac{s_o v h^3}{D_o} \frac{G(r_{s(i)}, r_j, \lambda_{ref}) G(r_j, r_{d(i)}, \lambda_{emi})}{G(r_{s(i)}, r_j, \lambda_{ref})};\ x_{j\,=}\partial N_j$$

The S_o is calibration factor while h^3 represents the voxel volume. The D_o and v are the diffusion coefficient and speed of light in the medium. The two-point Green's function, G, models light transport for the given boundary condition. Optical properties at the reference wavelength of μ_a = 0.1 cm^{-1} and μ_s' = 10 cm^{-1} were used to model the optical properties of rat and chicken muscles for both in vivo and phantom studies (Marquez et al.; Nilsson, Berg and Andersson-Engels; Cheong, Prahl and Welch). In this case, a semi-infinite geometry is implemented. x_j is the jth recovered image voxel that contains the fluorescence yield, ∂N_j, obtained using a Moore-Penrose generalized inverse (Culver, Siegel, et al.).

2.2.2   System Performance Analysis

2.2.2.1 Design of Simulation Studies

The system's depth sensitivity was first evaluated with simulation studies before proceeding to phantom and in vivo studies. To evaluate the depth sensitivity, 1x1x1 mm fluorescent targets mimicking labeled sentinel lymph nodes were simulated as perturbations in homogeneous medium with the addition of 1% biological measurement noise at different depths. A sensitivity matrix with a simulated grid of 12 sources and 13 detectors was implemented for image reconstruction. To evaluate a potential clinical application, sentinel lymph node mapping for cancer staging, we reconstructed simulated fluorescent lymph nodes at various depths (3, 5, 8, 11, 15,) with simulated 1% noise (Figure. 2.3A). The reconstructed images suggest that the video-rate fluorescence DOT will have depth-sectioning capabilities with accurate depth localization down to 15mm confirming its potential for clinical application (Figure 2.3B). The resolution of the

system was tested by using the simulated 1x1x1 mm target at different depths. The size of the reconstructed perturbation is measured with the full width at half maximum (FWHM) of each target's point-spread function (PSF). We observe a broadening of the response with depth (Figure 2.3C).
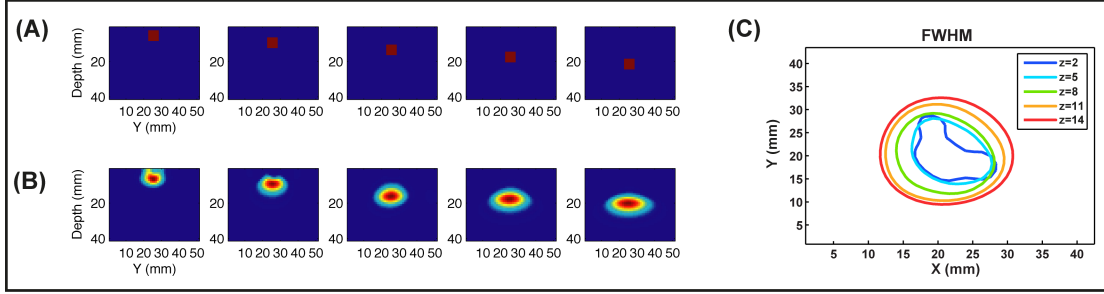
Figure 2.3: Evaluations of imaging depth sensitivity. To evaluate the depth sensitivity of the reflectance fluorescence DOT imaging array (Figure 2.1c), we reconstructed images from simulated data for targets at different depths. Two-dimensional slices through a volume show a cross-sectional view. Targets of 0.125 mL in volume (A) at the depths of 3, 5, 8, 11, 15 mm (left to right) were reconstructed. (B) Targets are all clearly visible even in the presence of simulated measurement noise (1%). (C) Point-spread function analysis using a simulated image reconstruction. Half-maximum contours of responses for different depths are shown.

2.2.2.2 Design of Phantom Studies

To evaluate the performance of the system, different concentrations of ICG targets in 3 mm diameter plastic tubes were prepared and embedded at 7 mm depth in a breast tissue mimicking phantom with μa = 0.1 cm-1 and $\mu's$ = 10 cm-1 (Figure 2.4A). The breast tissue simulating phantom was constructed by mixing 1% Intralipid solution with Black India ink to obtain the appropriate absorption and scattering properties (Flock et al.). The absorption and reduced scattering coefficients are chosen based on previously published values of rats and chicken breast optical properties (AN. Bashkatov et al.; Cheong, Prahl and Welch; Nilsson, Berg and Andersson-Engels; Marquez et al.). The targets contained solutions of indocyanine green (Sigma-Aldrich, St Louis, MO) in

concentrations ranging from 1 nM to 1 μM. The averaged values from regions-of-interest (ROIs) of the reconstructed image were compared to known concentrations to evaluate the sensitivity and linear response of the system.

Analysis of the system's sensitivity as a function of depth was performed by submerging a 3 mm diameter plastic tube of 4 μM concentration in a tissue-mimicking phantom. Starting at a depth of 5.5 mm, the tube was moved in 1.5 mm increments via a vertical stage until the middle of the tube reached a depth of 13.5 mm. The depth localization accuracy of the fluorescent target and sensitivity were calculated by averaging the intensity of the tube ROI and computing the center-of-mass for the different depths acquired.

2.2.3   Probe Dynamics Measurement in Sentinel Lymph Node Imaging

2.2.3.1 Design of in vivo Studies

We conducted a non-invasive preclinical study of fluorescent sentinel lymph node mapping in rats (n=5) with our fiber-based, video-rate fluorescence DOT system. The hair was shaved from the axillary region prior to imaging. In order to test the translational feasibility of the system to humans (which will require imaging at depths > 1 cm), we also conducted an experiment mimicking a deeper imaging scenario than would normally be available in a rat by inserting 8-10 mm of chicken breast tissue between the rat chest wall and the imaging pad (Figure 2.4B). Imaging through 8-10 mm chicken breast increased the depth of the SLNs to 10-12 mm, which is deeper than the typical 2 mm where the SLNs are normally located below the skin surface in rats. Control images were acquired for 1 minute prior to administration of the ICG, and the

dynamics of the injection in the axillary region were monitored for 10 minutes continuously.

Animal handling was performed according to the guidelines approved by the Washington University School of Medicine Animal Studies Committee for humane care and use of laboratory animals. For in vivo imaging, 50 μL of 100 μM ICG was injected intradermally in the left forepaw of 200-250 g female Sprague Dawley rats (HSD, Indianapolis, IN) after giving a mixture of ketamine (85 mg/kg) and xylazine (15 mg/kg) for anesthesia. After imaging, rats were then euthanized with an overdose of pentobarbital solution (150 mg/kg, IP) and the lymph nodes were then resected for verification of ICG uptake.

For reference and verification of ex vivo ICG uptake by the lymph nodes, superficial fluorescence images were acquired without the layers of chicken breast using the Pearl near-infrared (NIR) fluorescence imaging system (LiCor Biosciences, Lincoln, NE).
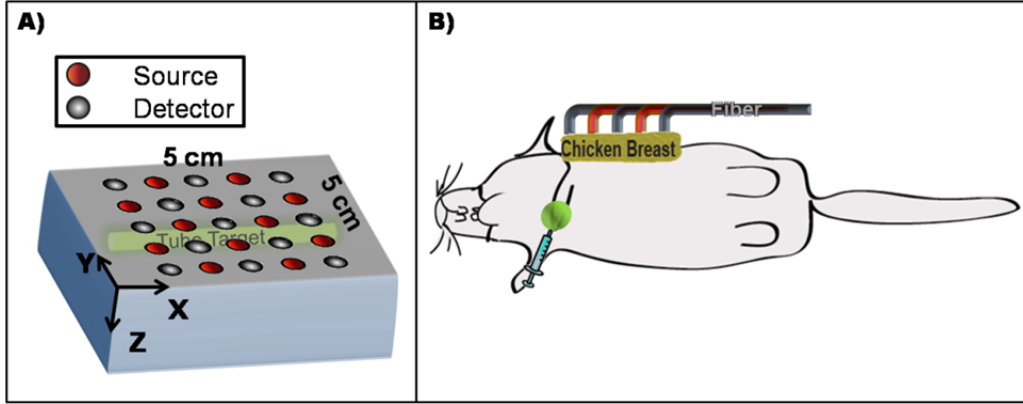
Figure 2.4: Schematic of the video-rate fluorescence DOT experimental setup. (A) Schematic of my experimental setup with an imaging array and a 3 mm ICG tube embedded in a tissue-mimicking phantom. (B) Schematic of the placement of the fiber array on a preclinical animal model using an 8-10 mm thick chicken breast to simulate a deep tissue imaging situation.

2.3 Results

2.3.1 System Performance Analysis with Phantom Studies

The Fourier transform of a measurement from a single detector illustrates the use of frequency-encoding to separate the emission and reference measurements acquired simultaneously (Figure 2.2B). Following frequency-decoding, the intensities of both reference transmission and emission were retrieved. The data was then used to generate volumetric reconstructions of the fluorescence distribution. The reconstructed images from various depths suggest that the newly developed video-rate fluorescence DOT system has the capability to accurately section depths up to 13.5 mm (Figure 2.5B). The resolution of the system was tested with simulated data for 1×1×1 mm phantom targets at different depths (Figure 2.3C). The center-of-masses (COMs) of the reconstructed fluorescence tubes (Figure 2.5B) were computed by averaging the fluorescence intensity values for each experimental depth. The linear relationship between the experimental

and the computed COMs demonstrate the depth localization accuracy up to 13.5 mm (Figure 2.5C). The sensitivity as a function of depth was computed by taking the mean fluorescence intensity of the regions-of-interest from reconstructed image for the different depths acquired (Figure 2.5D). The data demonstrate that the signal intensity drops exponentially with depth, as expected.

The relationship between the true dye concentration and the reconstructed voxel value (arbitrary units), is shown in Figure 2.5E. The graph confirms the high dynamic range and linear response of our system to varying ICG concentrations as measured by the resulting fluorescent yield from 1 nM to 1 μM. Values from this phantom analysis are used to generate a calibration factor for our in vivo studies.
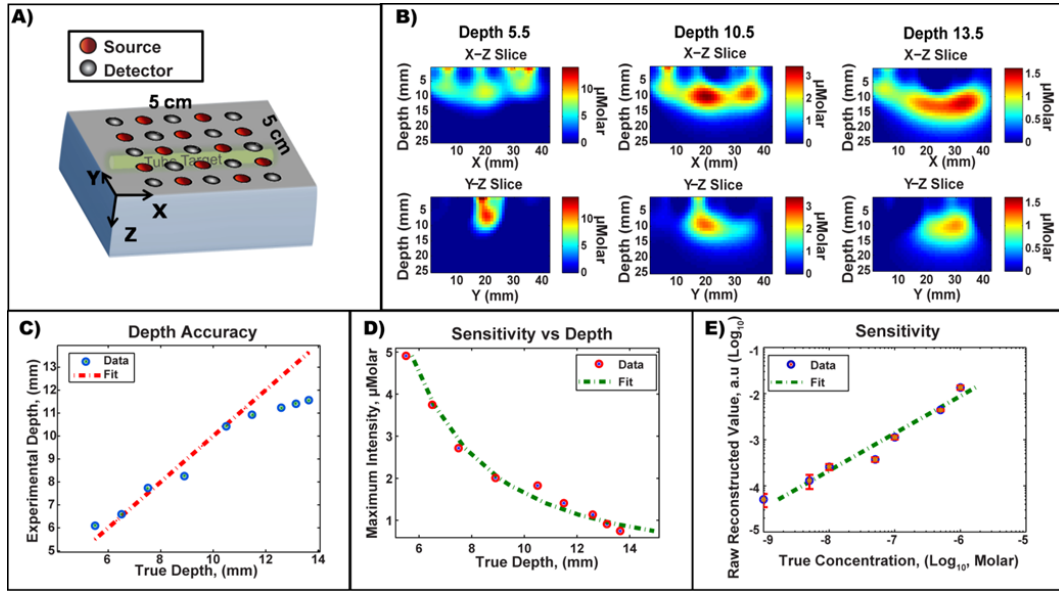
Figure 2.5: System sensitivity analysis with phantom studies. (A) Schematic of our experimental setup with an imaging array and a 3 mm ICG tube embedded in a tissue mimicking phantom. (B) Vertical x-z and y-z slices of reconstructed experimental data from a fluorescent 3 mm tube target whose center of mass is located at 7.5 mm, 10.5 mm, and 13.5 mm depths. The system accurately reconstructs the tube shape with some artifact at the optode positions. (C) Evaluation of the depth localization accuracy of a phantom target. The system has accurate localization from 6 to 13.5 mm. (D) Sensitivity vs. depth. The data demonstrate that the signal intensity falls off exponentially with depth. (E) The relation between the raw reconstructed value and the true concentration of the dye was characterized by titration of ICG from 1 nM to 1 uM concentrations in a 3 mm tube.

2.3.2   In vivo Imaging of the Uptake of the dye into SLNs

We performed a pre-clinical in vivo study to evaluate the feasibility of imaging sentinel lymph nodes in rats noninvasively. ICG was injected intradermally into the forepaw and the axillary region was imaged with DOT. The DOT images of fluorescent lymph dynamics shown at 2 mm were obtained following injection of the ICG (Figure 2.6A). Representative dynamics of fluorescent lymphatic fluid accumulation is obtained from a volume of about 30 mm^3 from the region of the sentinel lymph node of the injection site (Figure 2.6B). The mean of the background pixels shows no fluctuation associated with the dynamics of fluorescent dye.

Reflectance fluorescence images were captured using the Pearl NIR fluorescence imaging system before sacrificing the animal to confirm the DOT results (Figure 2.6C). Reflectance fluorescence images acquired after euthanasia and removal of overlying skin further confirmed ICG uptake by the lymph node imaged by DOT (inset on Figure 2.6D).
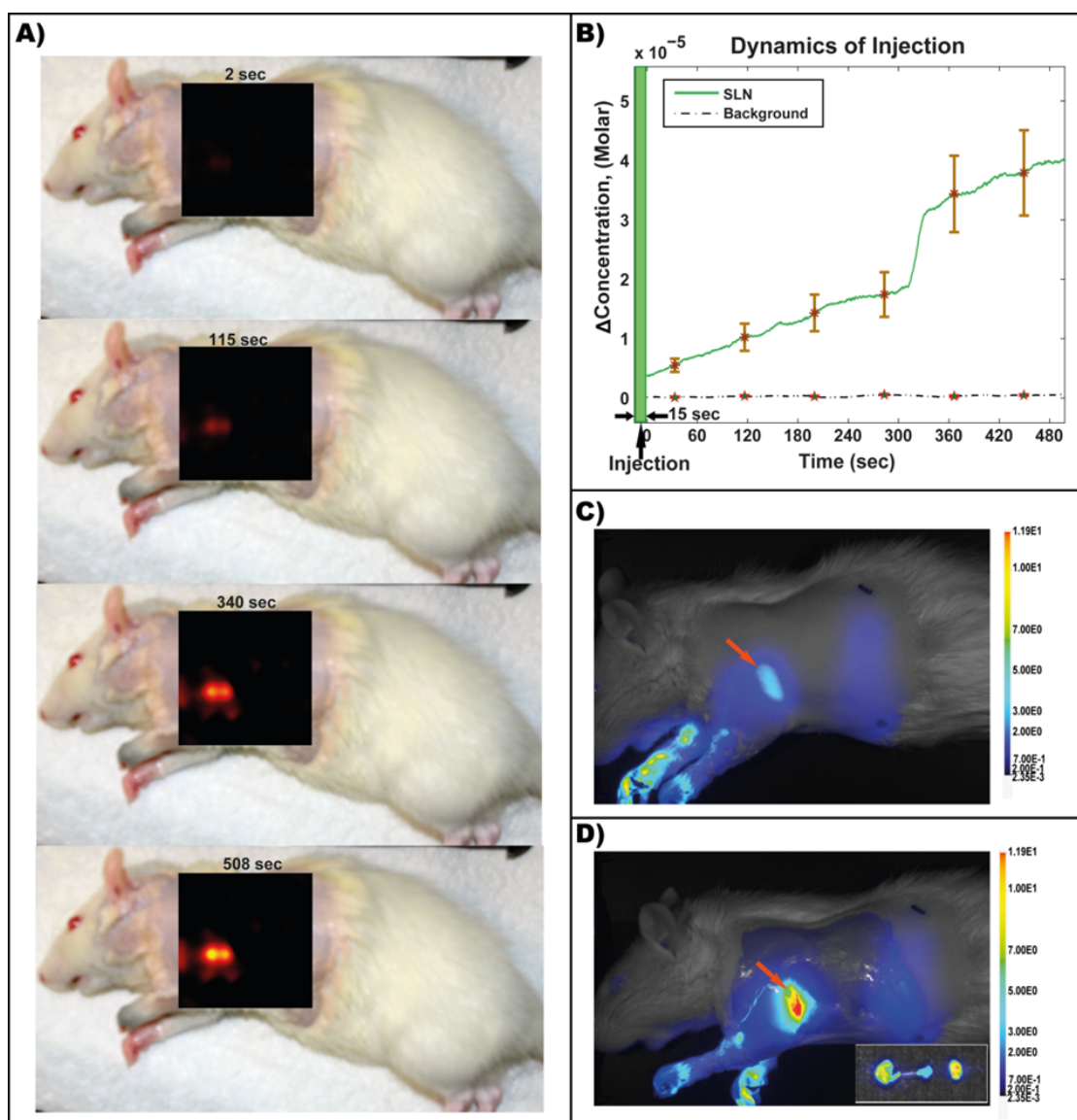
Figure 2.6: Shallow imaging of lymph dynamics. (A) DOT images of the fluorescence dynamics at 2 mm depth in a rat following injection of ICG into the left forepaw. (B) Time traces of the dynamics of ICG accumulation in the region of the sentinel lymph node (for comparison the mean background signal is shown). (C) Reflectance fluorescent imaging of the sentinel lymph node region demonstrating fluorescence from the injection site (paws) and the lymph vessels leading to axillary lymph nodes (arrow). (D) Reflectance fluorescent image of the rat after euthanasia and removal of overlying skin. Inset: fluorescence from ex vivo imaging shows ICG uptake in the lymph nodes.

We repeated the experiment with an increased imaging depth by inserting 8-10 mm of chicken breast between the rats (n=5) and the imaging pad. DOT images of fluorescent lymph dynamics were acquired and show that high quality imaging can be obtained even at increased depth (Figure 2.7A). Time courses of the SLN region as well as background pixels demonstrate the representative dynamics of fluorescent lymphatic fluid accumulation after the injection (in two individual rats Figure 2.7B and averaged over all five rats Figure 2.7C). The variability in the lymph dynamics and accumulation in the SLNs can be associated with inter- and intra-subject variability of the periodic expansion and contraction structures that surrounds the lymphatic vessels. The results demonstrate the potential of the video-rate fluorescence DOT system to image the in vivo dynamics of dye accumulation in SLNs.
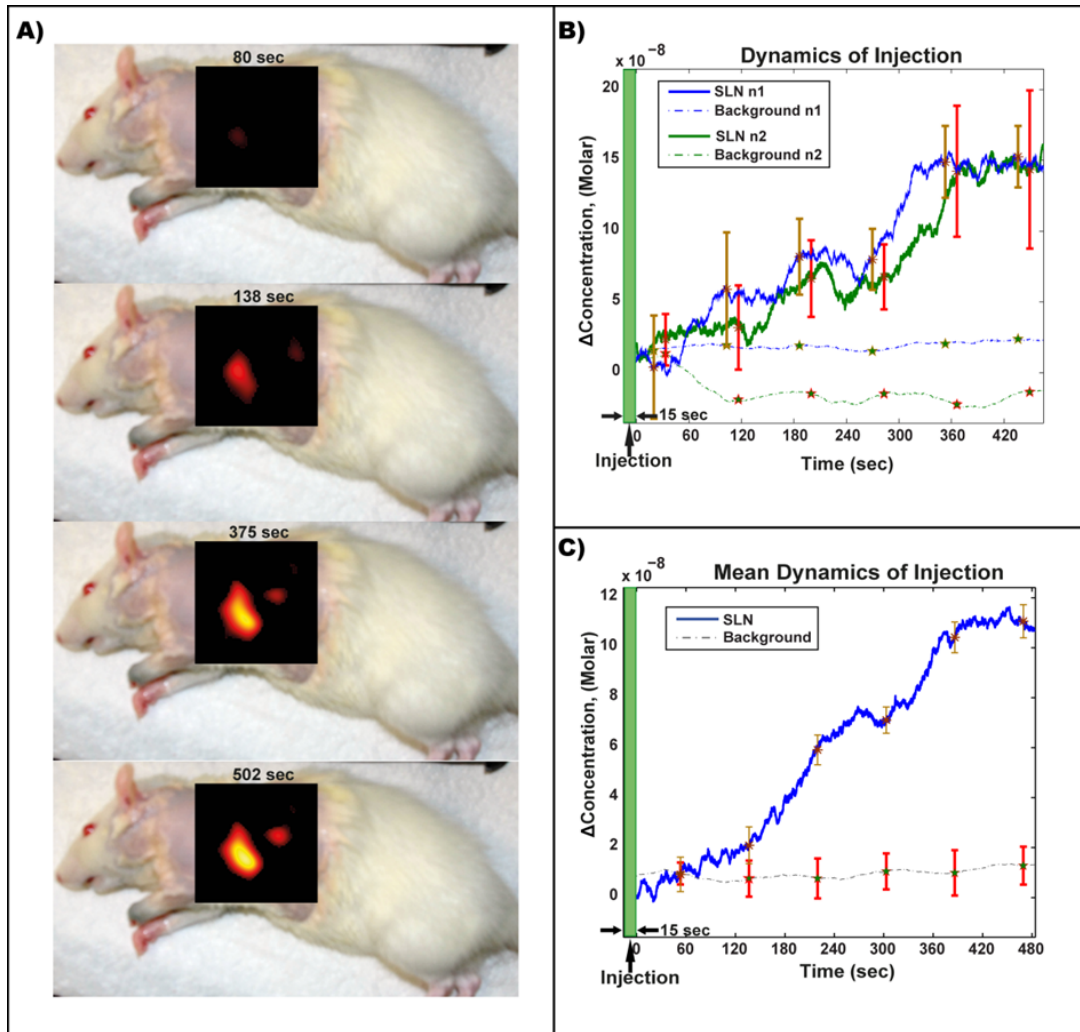
Figure 2.7: Deep (> 10 mm) imaging of lymph dynamics. The video rate fluorescence DOT was used to image the SLN region in rats through 8-10 mm of chicken breast following ICG injection into the rat forepaw. (A) The dynamics in a slice at 11 mm depth from a DOT reconstruction. (B) Time traces of the dynamics (for 2 representative rats) of a region around the SLN and of the mean of all background pixels. (C) Dynamics of ICG accumulation averaged over 5 rats.

2.4   Discussion

Fiber-based, video-rate fluorescence DOT has the potential to become a powerful and practical tool for a broad array of imaging applications, ranging from sentinel lymph node mapping to monitoring cancer therapy progress. We demonstrated the feasibility of a 30 Hz APD-based fluorescence DOT system. Images of fluorescent targets in tissue mimicking phantoms were used to confirm the high dynamic range and linear response of the system and the accurate localization of targets in the range of depths from 5.5 to 13.5 mm. As the optical properties used in our experiments are higher than those reported for human breast tissues we expect the depth sensitivity and dynamic range to be improved in human studies.

We also successfully demonstrated the in vivo capabilities of the system by noninvasively imaging the dynamics of ICG accumulation in a rat. Accumulated dye in the region of the sentinel lymph nodes was imaged to a depth of 10-12 mm over a 10 minutes time course. These results demonstrate the potential for imaging the pharmacokinetics of fluorescent diagnostic and therapeutic agents.

Previous two-dimensional fluorescence reflectance imaging (FRI) has been used to image lymph nodes and the lymphatic systems in animal models and cancer patients (Frangioni et al.; Proulx et al.; Sharma, Wang, et al.; Sevick-Muraca et al.; Troyan et al.; Sampath, Wang and Sevick-Muraca; Sharma, Wendt, et al.). For instance, the lymph dynamics and lymph node images obtained after injection of ICG in breast cancer patients show the feasibility of implementing FRI for nodal staging (Sevick-Muraca et al.). The specificity of the FRI method was further evaluated with an intraoperative FRI system by localizing the same SLNs as lymphoscintigraphy in breast cancer patients

(Troyan et al.). This particular FRI system is currently on clinical trials for intraoperative SLN mapping in cancer patients (Frangioni et al.; B. T. Lee et al.; Proulx et al.; Troyan et al.). While the FRI method is useful, its sensitivity declines quickly with imaging depth.

Three-dimensional DOT methods address several limitations of FRI and can potentially improve deep-tissue sensitivity, volumetric localization, resolution, and quantitative accuracy. For example, DOT approaches have been used in small animals to image whole bodies (Intes, Ntziachristos, et al.; S. V. Patwardhan, S. R. Bloch, et al.) and in humans to image breast (Pogue, Poplack, et al.; Culver, Choe, et al.; Choe, Corlu, et al.; Q. Zhang et al.) and brain (Joseph et al.; Austin et al.) tissues at depths of several centimeters. One limitation of our current system for application in humans is the limited field of view. The potential for an expanded system with up to 48 sources and 48 detectors has been demonstrated for brain imaging (White et al.). A higher density imaging array could also potentially increase the resolution, particularly at the shallower depths (Culver, Ntziachristos, et al.).

Sentinel lymph node localization is currently performed by administering radiocolloids conjugated with blue dye for intraoperative guidance (Rzyman et al.). The potential of implementing other organic optical dyes such as fluorescein and indocyanine green has also been demonstrated in multiple clinical trials (Sampath, Wang and Sevick-Muraca; Sevick-Muraca et al.; Troyan et al.; Hojo et al.; B. T. Lee et al.; Proulx et al.). Extensive research is still needed into targeted optical dyes. Fiber-based, video-rate fluorescence DOT aided with targeted optical dyes could have the potential to assess the cancer status of SLNs non-invasively in order to avoid unnecessary surgical procedures.

Multimodal imaging with fluorescence DOT could also play an important role in the detection and imaging of sentinel lymph nodes for cancer management. DOT could be combined with, for example, nuclear imaging to improve the accuracy of DOT images during data processing and image reconstruction (Cao and Peter; A. Li et al.; Barber et al.). In addition to a standalone mode (and due to the flexibility of the fiber array geometries), video-rate fluorescence DOT also has the potential to be combined with handheld ultrasound (US) and/or photoacoustic tomography (PAT). Fibers assembled around the periphery of the PAT/US imaging head could provide many tracings through the PAT/US imaging volume. A similar approach wherein DOT is combined with ultrasound has been demonstrated feasible for imaging breast cancer (Q. Zhu et al.; Quing Zhu et al.). In these scenarios, the fluorescence molecular contrast of DOT would complement the high-resolution function and anatomical data of PAT and US.

2.5   Conclusion

In this chapter, we have shown we have developed a fiber-based, video-rate fluorescence DOT system and demonstrated its potential for in vivo imaging. We have demonstrated that a 30 Hz APD-based DOT system can be operated in fluorescence mode. A fiber-based imaging array was used to image a fluorescent target within a tissue-mimicking phantom and to exhibit our system's high sensitivity. These results confirmed the high dynamic range and linear response of the system. We have also successfully demonstrated the capability of the system for sentinel lymph node mapping in rats. Further progress with this technology has the potential to provide a useful clinical tool

for a wide array of imaging applications, ranging from sentinel lymph node mapping to

monitoring cancer therapy progress.

Chapter 3

Multimodal Fluorescence Mediated Tomography and SPECT/CT for Small Animals Imaging

3.1 Introduction

Multimodal imaging strives to improve upon uni-modal imaging by combining multiple contrasts. For example, combining anatomical and molecular imaging (PET/CT and SPECT/CT) has provided an anatomical context for the detailed molecular information from the nuclear contrasts (Quing Zhu et al.; Alberini et al.; Even-Sapir, Keidar and Bar-Shalom). However, full fusion of the anatomical and molecular information is limited by the relatively weak connection between the different contrasts. Alternatively multiple molecular contrasts might be joined through specific links (S. Achilefu, Y. P. Ye, et al.; Zhang and Achilefu). For example, optical methods have unique activation contrast mechanisms, which are complementary to PET/SPECT information. The information available to both nuclear and optical contrasts can be harnessed directly using monomolecular multimodal imaging agent (MOMIA) (S. Achilefu, Y. P. Ye, et al.; Zhang and Achilefu). Imaging of MOMIA agents requires suitable instrumentation and algorithms. To combine optical data with PET/SPECT, optical contrasts can be imaged in three dimensions by diffuse optical tomography (DOT) (Z. R. Zhang et al.; Cao and Peter; Culver, Akers and Achilefu; C. Q. Li et al.). In this chapter, we demonstrate the feasibility of combining the previously reported fiber-based, video-rate fluorescence mediated tomography (FMT) system (Metasebya Solomon et al.) with a preclinical NanoSPECT/CT platform (Bioscan, Inc.) for combined optical and nuclear imaging of dynamic events associated with lymphatic transport.

The design and construction of a multimodal imaging platform presents a number of challenges. The first is integrating hardware such that each modality can function with minimal, or acceptable, interference from the others. Hardware integration requires

compatibility of all the parts for both platforms. The second challenge is spatial and temporal co-registration of information from the disparate reporting strategies under each modality. For instance, the distinct chemical and physical characteristics of traditional contrast agents might lead to different biodistribution and migration rates. MOMIAs are being developed to address these pharmacokinetic issues. Recent work has demonstrated the use of this approach for SPECT/optical (H. Lee et al.; Q. Zhang et al.), PET/Optical (Berezin, Guo, Teng, et al.; Zhang and Achilefu), and MRI/optical (Gulsen et al.; Guo et al.; Ntziachristos, Yodh, et al.) imaging. The last challenge is determining how to merge the anatomical or functional information from multiple technologies into a single imaging output. This is currently a subject of intensive research, though most of the work is focused on incorporating structural information from X-ray/CT (Ntziachristos, Yodh, et al.; Culver, Akers and Achilefu; Q. Zhang et al.) or MRI (Q. Zhang et al.; Gulsen et al.) with molecular imaging. Merging information that leverages the respective strengths of each modality would provide new insight into biological processes relevant to cancer diagnosis and therapy monitoring (S. Achilefu, Y. P. Ye, et al.; Culver, Akers and Achilefu).

To address the instrument integration challenges, we took advantage of the flexibility of fiber arrays to provide a compact conduit of light to and from the animal so that the FMT imaging array could fit into the bore of the existing NanoSPECT/CT system without modifications. In addition, to facilitate integration of the nuclear and optical contrasts, we used a MOMIA based on a radiolabeled near-infrared dye synthesized in our laboratory (Zhang and Achilefu).

Feasibility studies of simultaneous fluorescence and radioactive imaging were performed in tissue simulating phantoms and in vivo in rats. Accurate depth localization of the MOMIA targets was established to depths of up to 10 mm. Fluorescence and radioactivity from an injection of MOMIA into the forepaw region was imaged over time to follow the lymphatic dynamics. These studies were used to assess whether the proposed combined multimodal platform has the potential to become a practical tool for a broad array of imaging applications, ranging from early disease detection to monitoring progress of disease and therapies.

3.2   Materials and Methods

3.2.1   Fiber-based FMT Imaging System

DOT source and detector console: Laser diodes with a wavelength of 785 nm (Thorlabs DL7140-201S) (3.5 mW) and 830 nm (Thorlabs HL8325G) (1.5 mW) have dedicated drivers and control lines for each source to allow flexible software configurable source encoding (frequency- and time- encoding). The detection channels use optically-filtered discrete avalanche photodiodes (Hamamatsu C5460-01) digitized with dedicated 24-bit analog-to-digital converters (MOTU HD 192). The narrowband optical filters (CVI) have an 830 +/- 10 nm center wavelength and an out-of-band rejection of OD4, thus blocking the excitation light while passing the fluorescent and reference signals. An aspheric lens is used to collimate the light to optimize the blocking of excitation light by the narrowband interference filter and enhance fluorescent signal detection. With this scheme, we acquire frequency-encoded fluorescence emission and reference transmission (used to normalize the measured fluorescence) light levels

concurrently at each detector. This ratio-metric data allows DOT reconstructions using the normalized Born approximation, resulting in a map of quantified fluorochrome distribution. All data are acquired at a frame rate of 30 Hz. A total of 108 measurements from source-detector pairs representing the 1st, 2nd, and 3rd nearest-neighbors are used for image reconstruction. Further design elements and capabilities of the fiber-based, video-rate FMT are detailed in the previous chapter (Metasebya Solomon et al.).

DOT imaging fiber array: The imaging array is composed of a grid of alternating sources (12) and detectors (13). Light from the sources is coupled into 0.5 numerical aperture with 2.5 mm diameter fiber bundles made of borosilicate glass sheathed with lightweight silicone. The DOT imaging array composed of flexible silicone with right-angle fibers is integrated with the NanoSPECT/CT system.

3.2.2   SPECT/CT Acquisition

To test the compatibility of inserting the fiber-based FMT into nuclear platform, we used a NanoSPECT/CT platform (Bioscan, Inc., Washington, D.C.). For NanoSPECT/CT scanning, first, CT was performed (using a 45 KVP energy tube at 177 mA and 180 projections with 400 ms exposure with pitch of 1), followed by helical SPECT of 16 projections with 60 seconds each. CT and SPECT projections were reconstructed using InvivoScope software (Bioscan, Inc., Washington, D.C.). The high-resolution NanoSPECT/CT anatomical and radioactive data-sets have isotropic voxel size of 0.4 and 0.6 mm respectively.

3.2.3   MOMIA Synthesis

DOTA-Gly-Ser-Gly-Lys(Cypate)-E-Ahx-NH2,LS444,   was   synthesized   and
radiolabeled with ^{111}InCl$_3$ (MSD-Nordion, Kanata, ON, Canada, 3.0 microcuries (μCi)) in
aqueous buffer (190μl, 0.4 M sodium acetate, pH 4.5, 30 min, 98 °C) as described
previously (Zhang and Achilefu). Labeling efficiency and radiochemical purity were
checked by HPLC (Supelcosil ABZ $^+$ PLUS, HPLC Column, 15cm X 4mm, 5μm) with a
gradient of H$_2$O and acetonitrile containing 0.1% TFA. The radiochemical purities of
peptides used in the studies were always above 95%. The specific activity was 223.0
μCi/nmol.

3.2.4   Experimental Protocol

Animal handling and preparation was performed according to the guidelines
approved by the Washington University School of Medicine Animal Studies Committee
for humane care and use of laboratory animals. A flowchart of the acquisition timeline is
presented in Figure 3.1A. The rats (n=5, 200-250 g Female Sprague Dawley, HSD,
Indianapolis, IN) were first anesthetized via a mixture of ketamine and xylazine (85
mg/kg and 15 mg/kg IP). The MOMIA imaging agent (100 μL of 111In-LS444) was
then administered via forepaw injection. Concurrent FMT/SPECT/CT imaging was
performed immediately after injection.

The DOT imaging fiber array was securely positioned on top of the rat, which was
then advanced into the NanoSPECT/CT imaging chamber (Figure 3.1B). The
SPECT/CT scanning regions were selected to include the injection site as well as the
DOT imaging pad by top-view topogram. CT was performed followed by helical
SPECT, with total acquisition times of 5 and 16 minutes respectively. To evaluate the

influence of the DOT array on the SPECT/CT data-sets, we also acquired SPECT/CT data without the DOT fiber array with the same imaging protocol as described earlier (Figure 3.1C).

For reference and verification of ^{111}In-LS444 uptake by the lymph nodes (LNs), reflectance fluorescence images were acquired in vivo before and after removal of overlying skin following euthanasia using the near-infrared (NIR) reflectance fluorescence system (Pearl, LiCor Biosciences, Lincoln, NE). Lymph nodes were excised post-mortem and examined with the Pearl imaging system and dosimeter to further validate the origin of the fluorescent and the radioactivity signals respectively. In addition, the resected lymph nodes were frozen in OCT and sectioned in the cryostat to 8-μm thickness. NIR fluorescence (775 +/- 55 nm excitation and 810 nm long pass emission filters) and brightfield microscopy images were acquired using Olympus BX51 upright epifluorescence microscope (Olympus America, Center Valley, PA). The same slides were stained with hematoxylin and eosin (H&E) and imaged with fluorescence microscopy.

To evaluate the performance of the system as a function of depth, we followed the approach used for the stand-alone FMT system (chapter 2) (Metasebya Solomon et al.), but in this instance with MOMIA targets. The tissue mimicking phantoms were constructed by mixing agarose (Sigma-Aldrich, Saint Louis, Missouri) with intralipid (20% fat emulsion, Fresenius Kabi, Germany), and India ink (Speedball, Statesville, North Carolina) to obtain the appropriate absorption and scattering properties with μa = 0.19 cm-1 and $\mu's$ = 3.4 cm-1. The mixture was poured into a mold and allowed to solidify at room temperature. Targets consisting of 3 mm diameter plastic tubes filled

with the MOMIA agent were prepared and embedded at 4, 7, 10 mm depths in the tissue simulating phantoms. The imaging protocols described above were implemented to acquire optical and nuclear data-sets of the phantoms with targets at different depths.
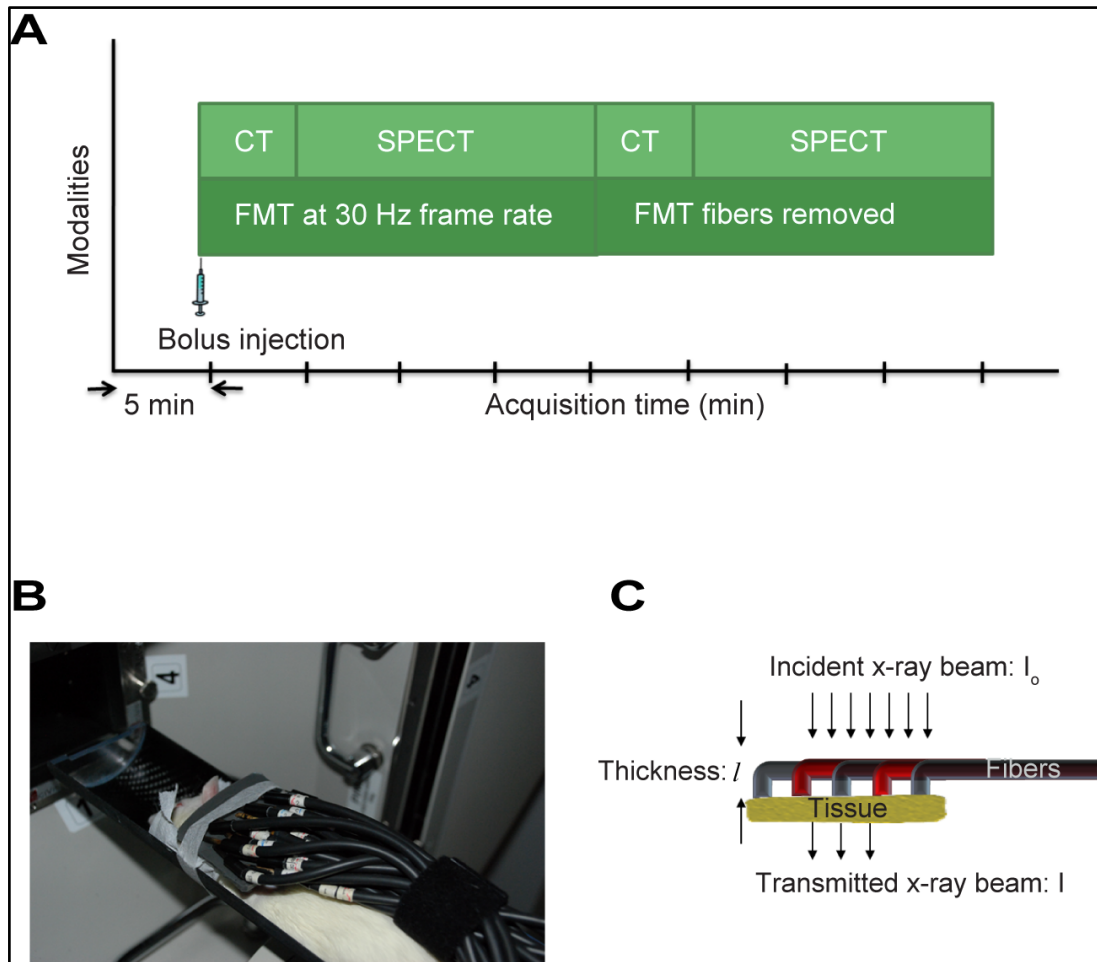
Figure 3. 1: Schematic experimental setup and timeline of the multimodal experimental protocol. (A). Timeline of the multimodal experimental protocol. (B) Picture showing the placement of the fiber array on a preclinical animal model before advancing into the NanoSPECT/CT imaging chamber. (C) Schematic of the fiber array to demonstrate its effect on the transmitted x-ray beam.

3.2.5 Fluorescence DOT Reconstruction

We generated a subject-specific three-dimensional (3D) finite-element model (FEM) (Figure 3.2). Using anatomical data of rats obtained from 3D X-ray CT projections (Figure 3.2A), we created a tetrahedral mesh using Mimics™ with a maximum inter-nodal distance of 1 mm both on the surface and within the mesh volume. The mesh, composed of 400,399 linear tetrahedral elements connected by 67931 nodes, was segmented into two tissue types: bone and soft tissues and assigned their corresponding optical properties (μa = 0.17 cm^{-1}, μ's = 24 cm-1 and μa = 0.19 cm^{-1}, μ's = 34 cm^{-1} respectively) (Figures 3.1C and D). A heterogeneous tissue model was employed because previous studies have shown improvements relative to light models that assume homogeneous optical properties (Metasebya Solomon et al.; Niedre, Turner and Ntziachristos; Dehaes et al.; Heiskala et al.; Eggebrecht et al.). For the tissue-simulating phantom imaging, we also used the 3D phantom X-ray CT projections and created a homogeneous mesh and assigned the corresponding optical properties (μ_a = 0.19 cm-1, μ_s' = 34 cm-1). A second anatomical CT data-set of each rat and tissue mimicking phantom was obtained with DOT fibers in place and was used to obtain the 3D coordinates of the optodes (sources and detectors) positions (Figure 3.1B). The resulting FEM mesh and co-registered source and detector locations were used for light modeling (Figure 3.1E).

The light transport through the tissue was calculated using NIRFAST following our previously reported methods (Dehghani et al.). Briefly, an adjoint approach to constructing the Jacobian was used to construct a sensitivity matrix. The construction of the sensitivity matrix specific to fluorescence imaging follows the methods previously

described (see chapter 2 (Metasebya Solomon et al.)). The sensitivity matrix maps the relationship between the optical parameters (fluorescence distribution) and the measurements (Ntziachristos and Weissleder "Experimental Three-Dimensional Fluorescence Reconstruction of Diffuse Media by Use of a Normalized Born Approximation") following the normalized Born approach (Metasebya Solomon et al.). We directly invert the sensitivity matrix via a Moore-Penrose generalized inverse (Metasebya Solomon et al.; Culver, Durduran, et al.). The experimental source-detector measurements are converted into images by matrix multiplication with the inverted matrix. The recovered fluorescence yield of the tissue at each FEM node is then presented in 3D. The mesh nodes are then transformed to a voxellated three-dimensional space of 1 mm isotropic voxel space for integration with SPECT/CT (the point spread function (PSF) of the FMT system is ~1.2 cm at 1 cm depth (Metasebya Solomon et al.).

The accuracy of the reconstructed FMT image is further improved by using the radioactivity measurement obtained from SPECT as a spatial priori to create a binary mask. The mask is then multiplied with the simulated light propagation matrix (sensitivity matrix) to constrain the FMT image reconstruction.
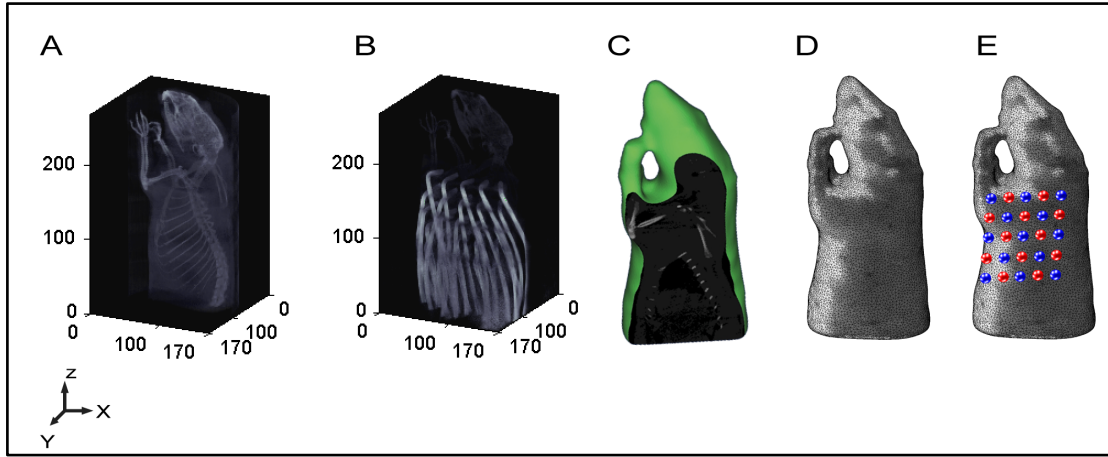
Figure 3.2: Fluorescence DOT Image Reconstruction. (A) An X-ray CT is used to capture the three-dimension structure of the anatomy of a rat. (B) X-ray CT image with the fiber array of DOT used to obtain optode positions. (C) Sagittal section of the anatomical X-ray CT image after segmentation into bone and soft-tissue region using MimicsTM. (D) 3D finite element model (FEM) of small animal half-body mesh generated from CT within MimicsTM to be used for forward modeling of light propagation.(E) Small animal mesh after projection of the optodes (source (red) and detector (blue)). Sensitivity matrix is then generated using the mesh and the measurement parameters as the main inputs for the FEM modeling of light in tissue using NIRFAST (Dartmouth).

3.2.5 Quantification of the Influence of FMT Fibers on SPECT and CT

We evaluated the potential for the presence of the optical fibers to negatively impact the imaging performance of the SPECT/CT imaging systems. The influence of the optical fibers on the transmitted x-ray depends on the linear attenuation coefficient (μ) of glass fibers at a given energy window and the thickness of the fiber arrays (l) (Figure 3.1C). The fraction of the transmitted x-ray beam is calculated using the following equation, $I = I_0 e^{-\mu \cdot l}$, where I_o and I are the incident and the transmitted X-ray beams respectively and l is the effective thickness of the glass fiber elements.

In addition, the normalized root mean square error (NRMSE) is used to quantify the distortions induced in the nuclear data due to the presence of the optical fibers:

$$NRMSE = \frac{\sqrt{\dfrac{(X - X_{ref})^2}{N}}}{\max(X_{ref})}$$; where X is the nuclear image with DOT fiber array and X_{ref} is the reference image without the optical fibers. N is the total number of image pixels. NRMSE is computed for both the SPECT and X-ray CT data-sets.

3.2.6 Quantifying Image Quality: Localization Accuracy

The localization accuracy of the FMT reconstruction compared to their corresponding SPECT data-sets was evaluated by calculating the absolute error in the center of masses' (of the optical and nuclear contrasts) of the lymph node volumes. The mean fluorescence and radioactivity intensity values in the XYZ-planes were computed for each subject from the reconstructed nuclear and optical data-sets to compute the center of masses (COMs). In addition, the absolute error of the COMs was computed to

assess the positional error between the fluorescence and radioactive distributions. The COMs and COMs error of the reconstructed MOMIA tubes were also computed by averaging the fluorescence and radioactive intensity values for each experimental depth. In addition, quantitative comparison of the difference in spatial resolution was quantified by comparing the volumetric ratio of the ROIs between the nuclear and optical data-sets of the various depths of the reconstructed tubes.

3.3   Result

The goal of this study was to demonstrate the feasibility of combining fiber-based FMT with NanoSPECT/CT. This combined nuclear-optical platform obtained data from both contrast mechanisms concurrently in space and time. Signal from a monomolecular multimodal imaging agent (MOMIA), ^{111}In-LS444, was used to facilitate the spatial integration of the nuclear and optical data.

The potential influence of the optical fibers on the nuclear imaging data-sets was evaluated both by computing the X-ray beam attenuation due to glass fibers and, more directly, by measuring the variance introduced into the CT and SPECT signals by the DOT fiber array. The experimentally derived transmission losses for the X-ray beam were consistent with the trends of the theoretical estimates based on attenuation coefficients (energy dependent) of the glass fiber (Table 3.1). Model calculations estimate the X-ray beam transmission through the fiber array to be 31% for CT (45 keV) and 68 % for SPECT (245 keV).

69

	SPECT	CT
Radiation Energy (E)	245 keV (^{111}In)	45 keV
Attenuation coefficient of glass, μ(E), cm^{-1}	0.256	0.781
Thickness (l) in cm	1.5	1.5
Transmission [%]	68	31

Table 3. 1: Evaluation the effect of fluorescence DOT fiber arrays on the transmitted X-ray beams of the nuclear imaging system
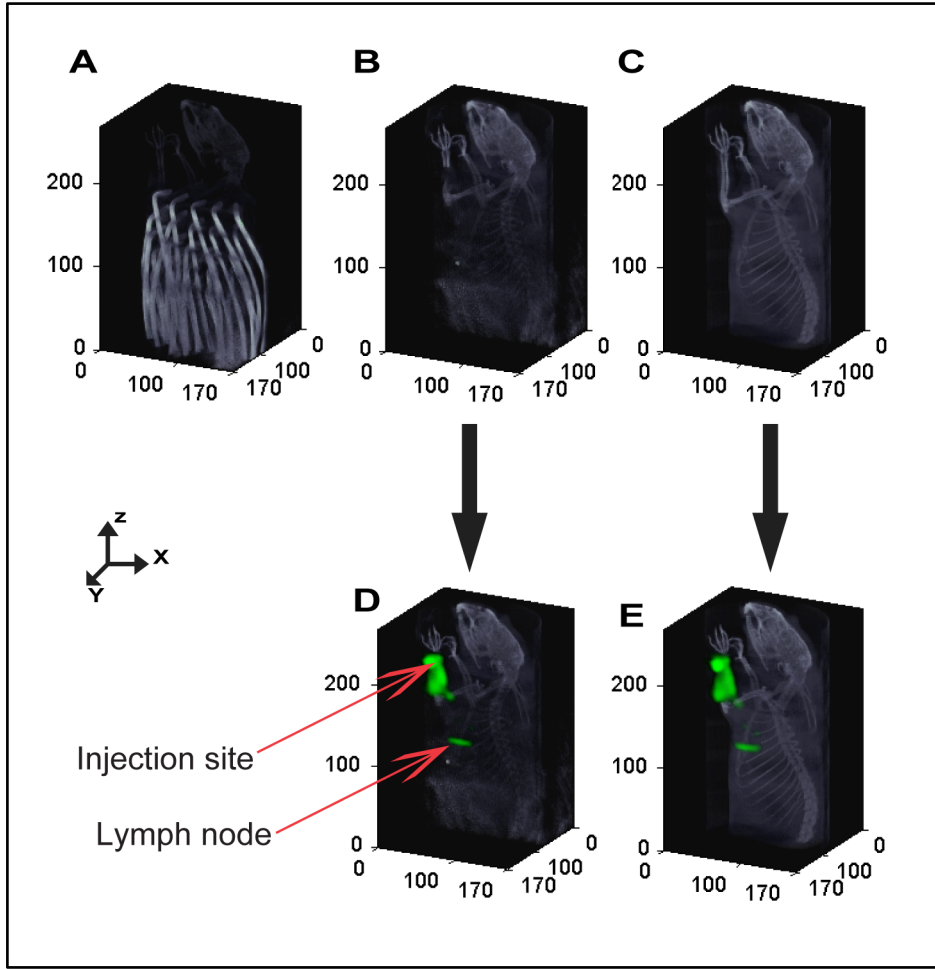
Figure 3. 3: Evaluating the influence of fiber arrays on SPECT and CT images: (A) X-ray CT image of a rat with the fiber array of DOT. (B) X-ray CT image of the same rat shown after removing the voxels related to the fiber array of the DOT. (C) X-ray CT acquired after removing the DOT imaging pad. The anatomical structures acquired without the fibers are used to display the fluorescence and radioactive distribution for all 5 rats. (D) SPECT data acquired at the presence of DOT fiber array depth in a rat following injection of multimodal imaging agent,[111]In-BS255, into the left forearm. (E) SPECT data of the same rat acquired after removing the fibers.

The computation of the NRMSE also demonstrated the existence of distortion introduced by the optical fibers (Figure 3.3A) in the nuclear data. The NRMSE between the X-ray CT anatomical data with and without FMT imaging fibers (Figure 3.3B and 3.3C) is 8.5%. The NRMSE between the radioactive data-sets acquired in the presence (Figure 3.3D), and absence (Figure 3.3E) is found to be 3.1 +/- 1.3 %, which also accounts for the additional MOMIA accumulated in LNs during the process of acquiring the reference SPECT measurements. For improved visual reference, the fluorescence and radioactive data are co-registered and displayed on anatomical x-ray CT obtained after removing the DOT fiber arrays (Figure 3.3E) for the remainder of the manuscript.

Images of the MOMIA targets in tissue mimicking phantoms confirm the localization of the targets in the range of the depths from 5-10 mm (Figure 3.4, Tables 3.2 and 3.3). The average absolute error between the COM of the optical and nuclear data-sets for all three depths was 4.1 +/- 2.1 mm. The average depth dependent spread of the volume of the FMT compared to the SPECT was 2.4 +/- 0.95 after thresholding at 30% maximum.
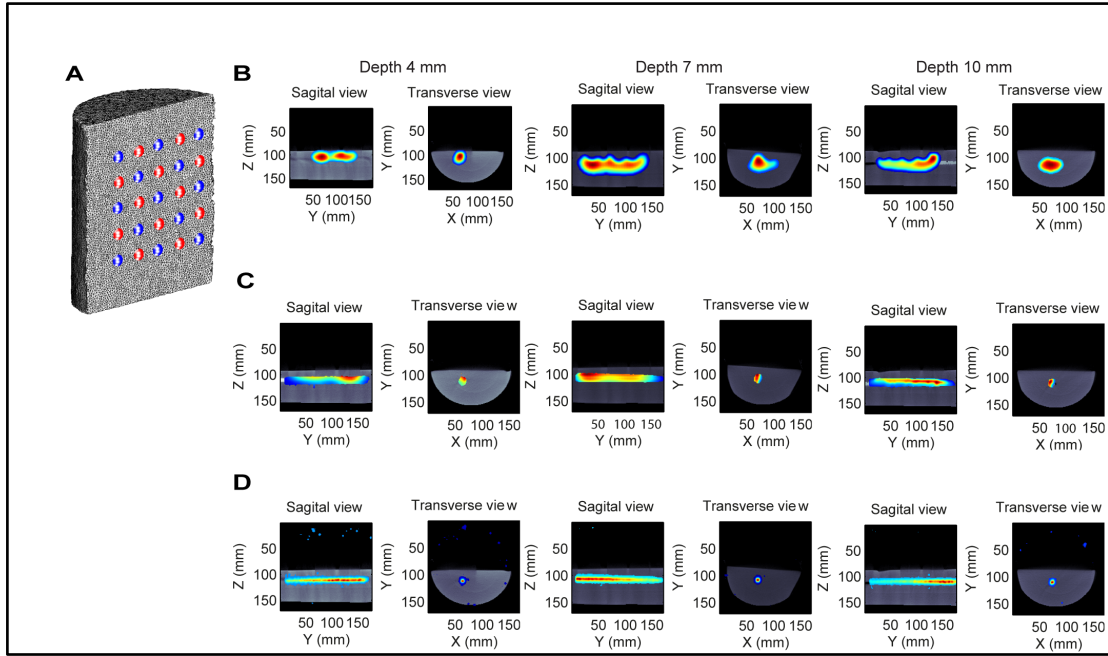
 Figure 3. 4: Depth sensitivity analysis with phantom studies. (A) 3D finite element model (FEM) mesh of the tissue phantom with the positions of the optodes (source (red) and detector (blue)). These were used to model light propagation. (B) Sagittal and Transverse Views of reconstructed experimental data from a 3mm tube target, filled with MOMIA contrast, whose center of mass is located at either 4, 7 or 10 mm depths. The fluorescence data shown is thresholded to >30% of max sensitivity. (C) Sagittal and transverse view of reconstructed fluorescence tube after incorporating SPECT contrast as a prior in the reconstruction. (D) Sagittal and transverse view of the SPECT-CT image demonstrate localization of the MOMIA at various depths.

	COM {X, Y, Z} in mm	COM Error (mm)	DOT to SPECT Volumetric Ratio	DOT to SPECT Volumetric Ratio (>30 % maximum fluorescence intensity)
Shallow	DOT = {8.4, 4.6, 31.9}	3.4	3.7/1	1.3 /1
	SPECT = {11.7,4.7,31.5}			
Mid	DOT = {12.6,6.7,31.9}	6.4	4.3/1	2.9/1
	SPECT = {10.1,7.4,37.7}			
Deep	DOT = {12.3,7.6,41.2}	2.5	5/1	3/1
	SPECT = {11.2,9,39.5}			

Table 3. 2: Quantitative comparison of the localization between nuclear and optical data sets.

	COM {X, Y, Z} in mm	COM Error (mm)	DOT to SPECT Volumetric Ratio
Shallow	DOT = {10.9, 4.1, 34.1}	2.6	0.9/1
	SPECT = {11.7,4.7,31.5}		
Mid	DOT = {9.6,6.3,35.1}	2.9	0.85/1
	SPECT = {10.1,7.4,37.7}		
Deep	DOT = {11.1,7.4,37.7}	2.3	0.7/1
	SPECT = {11.2,9,39.5}		

Table 3. 3: Quantitative comparison of the localization between nuclear and optical data sets when SPECT is used to constrain the DOT reconstruction.

The co-registered molecular information with its corresponding anatomical structure, Figure 3.5, demonstrates the feasibility of obtaining measurements with FMT and SPECT molecular contrasts and structural information with X-ray CT. An anatomical X-ray CT of a rat provided structural information that facilitated segmentation of different tissue types including bone and soft-tissue. The tissue segmented structure was used to generate a finite element mesh and the corresponding optical properties of the different tissue types were assigned to each FEM element to provide an accurate light propagation model for the FMT forward calculation (Figure 3.2).

Reconstructed FMT images show uptake of the MOMIA by the LNs in the axillary region (Figure 3.5A). The localized radioactive signal in the axillary region of the SPECT/CT image also demonstrated the uptake of the MOMIA by the axillary LNs (Figure 3.5B). The high radioactive signals on the left forepaw, at the injection site, show the starting point of the lymph tract that leads to the axillary nodes. Due to the limited field of view of the FMT fiber array, the injection site is not visible in the reconstructed FMT image.
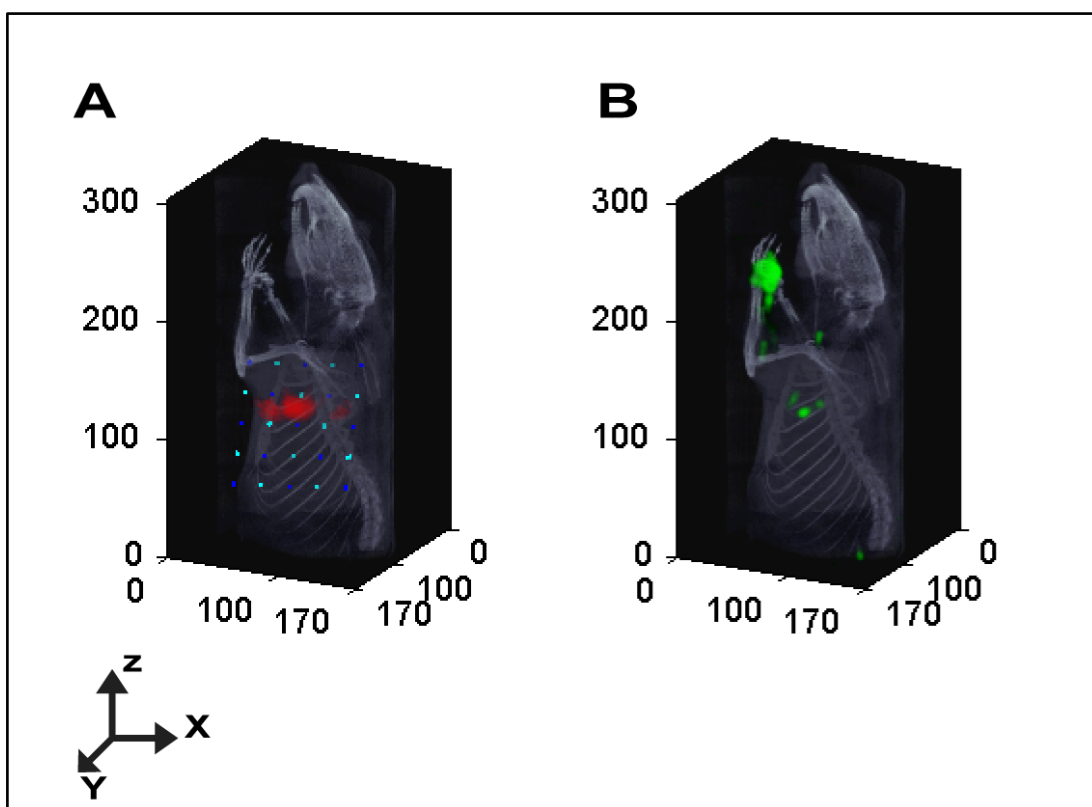
Figure 3.5: Representative Sentinel Lymph Node Mapping using Optical and Nuclear Imaging Systems. (A) DOT-CT image of the fluorescent LNs shown at 2mm depth in a rat following injection of multimodal imaging agent, ^{111}In-LS444, into the left forearm. (B) SPECT-CT image demonstrating localization of axillary lymph node identified by accumulation of the multimodal imaging agent.

The uptake of 111In-LS444 by the axillary LNs was further validated by combining the SPECT and FMT data-sets. The co-registered FMT/SPECT/CT images, Figure 3.6A, demonstrate co-localization of the multimodal agent in a spatially coincident region. The co-localization confirms that the radioactive and fluorescent signals originate from the same location corresponding to the LNs. The low overlap percentage can be attributed to the difference in resolution (or point spread function) between the optical and nuclear imaging systems and the presence of fractional component of non-radiolabeled LS444. However, the free LS444 fractional component is expected to be very minimal due to the high radiochemical purities of peptides used.

Having demonstrated the co-localization of the fluorescence and radioactive distribution, we explored a simple method to incorporate the high resolution NanoSPECT/CT radioactive data into the DOT image reconstruction to improve the localization accuracy of the axillary LNs signal. A binary mask, created from the radioactivity distribution of the SPECT data was multiplied with the simulated light propagation matrix to constrain the FMT image reconstruction. The SPECT/CT measurements fused with the FMT data-sets reconstructed with a priori, Figure 3.6B, demonstrated an improvement in congruency of the radioactive and fluorescence signal in the axillary regions. As a result of using SPECT as a hard prior, the overlap between DOT and SPECT is inherently unity. Likewise, it is assumed that the fluorescent signal originates from conjugated complexes and not from free optically active fragments. A soft prior approach to relax these conditions is suggested below. The average spatial discrepancy between the COM of the optical and nuclear data-sets for all five rats was

2.68 +/- 1.0 mm and 1.33 +/- 0.85 mm before and after incorporating SPECT as a priori respectively.
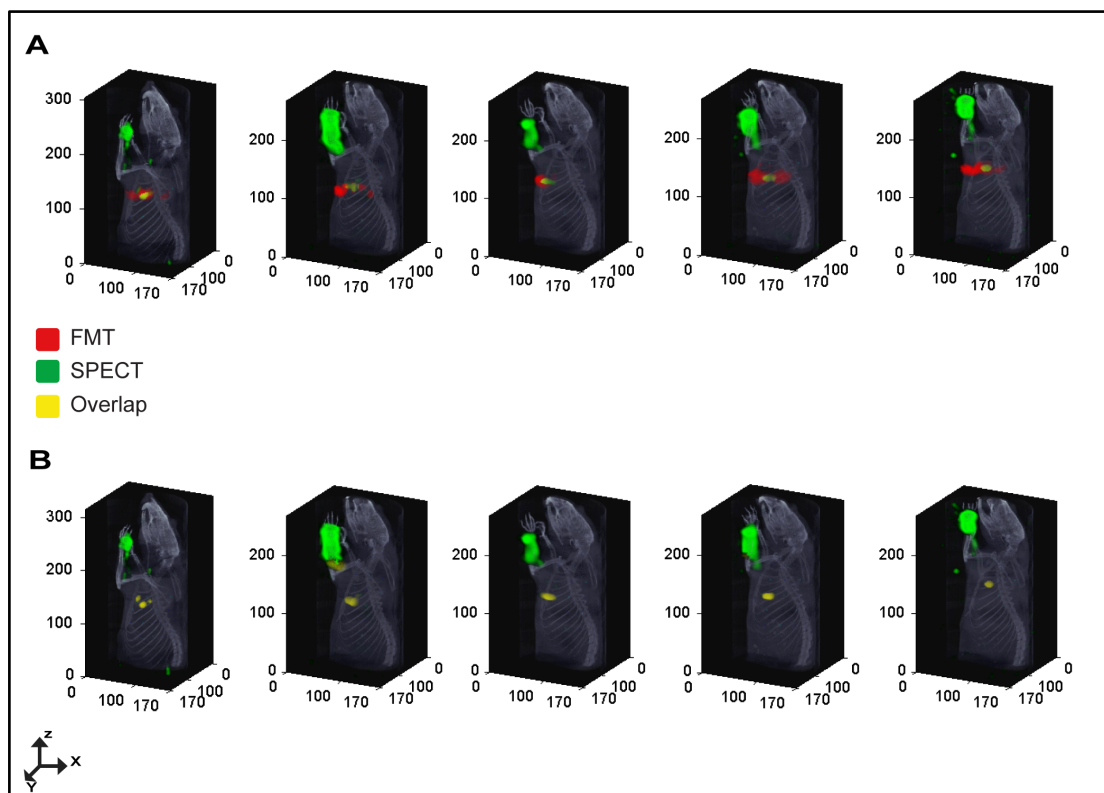
Figure 3. 6: Multimodal Sentinel Lymph Node Imaging. (A) Co-registered FMT-SPECT-CT image demonstrate co-localization of the MOMIA in spatially coincident region in 5 rats. (B) Demonstrate robust co-localization on the co-registered FMT-SPECT-CT image after using SPECT as a prior.

Reflectance fluorescence images were captured using the Pearl NIR fluorescence imaging system before sacrificing the animal to confirm the nuclear and DOT results. Reflectance fluorescence images acquired after euthanasia and removal of overlying skin further confirmed MOMIA uptake by the lymph nodes localized by DOT and SPECT (Figure 3.7A). The uptake of the MOMIA by axillary lymph nodes (inset on Figure 3.7A) was further confirmed with combined fluorescence and bright field microscopy (Figure 3.7B). In addition, the H&E stains validate the excised organ as lymph nodes due to the presence of centroblasts (dark zone) and centrocytes (light zone).
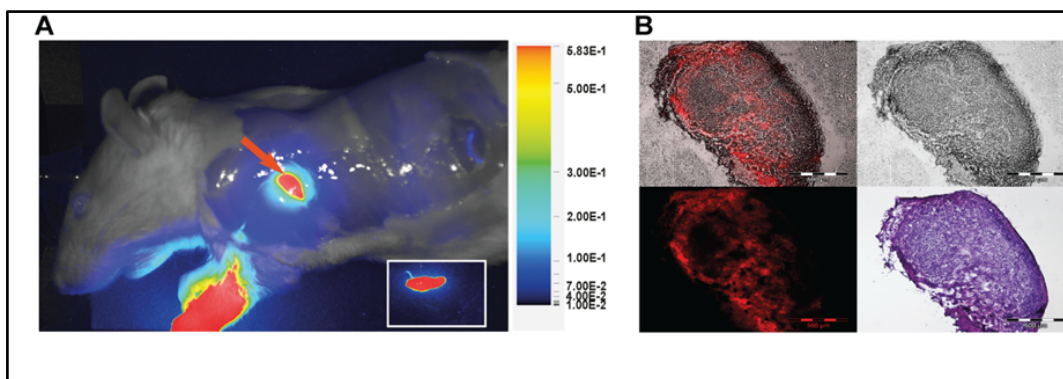
Figure 3.7: (A) Representative planar reflectance image of the sentinel lymph node regions demonstrating fluorescence from the injection site (paws) and the lymph vessels leading to the axillary lymph nodes (arrow) of the rats after euthanasia and removal of the skin. In set fluorescence from ex vivo imaging shows MOMIA uptake in the lymph nodes. (B) Representative microscopy images of fluorescent sentinel lymph nodes. Montages are a composite of brightfield and fluorescence microscope at top left and brightfield at top right. The bottom left and right represent fluorescence and H&E stained section respectively.

The radioactivity measured from excised LNs with a dosimeter demonstrate an uptake of approximately 0.45+/-0.17 % μCi (n=4) of the injected dose per SLN. The tracer uptake of sentinel nodes is highly variable as the lymph flow depends on factors such as massaging the injection site. For instance, in a study of melanoma cancer patients, uptake in the SLNs ranged from 0.00139-6.8% of the injected tracer dosage (Kapteijn et al.).

3.4   Discussion

The multimodal optical-nuclear platform shown has the potential to elucidate underlying biological mechanisms relevant to a wide array of diseases. We established the feasibility of integrating a fiber-based, video-rate FMT system with a preclinical NanoSPECT/CT platform. We used our recently developed MOMIA, which has the unique structural feature that both signals (fluorescence and radioactivity) emanate from the same source. The NIR fluorescent molecular probe, LS444, served as a contrast agent for FMT, while the [111]ln served as a source of signal for SPECT imaging to facilitate the fusion of the optical and nuclear data-sets with high spatial precision.

In this chapter, we evaluated the FMT/SPECT/CT system for imaging LNs in rats. CT provided high-resolution, co-registered anatomy. The combined optical-nuclear imaging demonstrated co-localization of a MOMIA in a spatially coincident region. We further demonstrated the congruency of the co-localization by incorporating SPECT as a prior in the DOT reconstruction. The average spatial discrepancy in the COMs of the contrasts between SPECT and FMT improved from 2.68 +/- 1.0 mm to 1.33 +/- 0.85 mm after incorporating SPECT into the FMT reconstruction.

Data-sets acquired separately with optical and nuclear platforms have been integrated previously (Kapteijn et al.; Nahrendorf et al.). For instance, Nahrendurfet et. al. demonstrated the similarity between FMT and PET by combining the two data-sets acquired sequentially on two different scanners using fiducial markers to co-register the data (C. Q. Li et al.). A strength of the current simultaneous optical-nuclear system is that it avoids potential misalignment of data-sets due to involuntary non-uniform movement of tissues during repositioning. Furthermore, the datasets in the presented study are co-registered in time. The first small animal study where optical imaging (scan rate not reported) was physically integrated into a PET system was reported by Li et al. (Nahrendorf et al.). Localization of the tumor with simultaneously acquired nuclear and optical datasets was performed after injection of two separate contrast agents (for fluorescent and radioactive detections) at different time points, separated by 24 hours, thus the data-sets were not co-registered in time. Further, acquisition of the anatomical information using a different scanner might lead to co-registration error of the functional molecular data with reference anatomy. To a significant extent, the system presented in this paper addresses many of these difficulties by combining three modalities

(FMT/SPECT/CT) within a single device. The FMT/SPECT/CT platform acquires the different functional (fluorescent and radioactive) and anatomical data either simultaneously or sequentially without moving the subject from the bed. This design essentially eliminates differences in subject positioning and minimizes misalignment due to involuntary internal organ motion.

While the current study does not focus on the dynamics of the lymph node accumulation, we have previously reported the capability of the FMT system for dynamic imaging by monitoring and generating time-course data of the lymphatic dynamics for indocyanine green (ICG) (Metasebya Solomon et al.). Accumulated dye in the axillary region of rats was imaged to a depth of 10-12 mm over a 10-minute time-course. Future studies will be needed to explore dynamic imaging of pharmacokinetics and pharmacodynamics for multimodal contrast agents.

Optical imaging can leverage the SPECT and CT information to improve accuracy during data processing and image reconstruction (Cao and Peter; A. Li et al.). For instance, we generated a small animal 3D finite-element model (FEM) using the 3D anatomical projections obtained from an X-ray CT to improve forward modeling of light propagation. In addition, incorporating SPECT data into the FMT reconstruction augmented the localization accuracy. An important future area of work is in developing algorithms to incorporate the SPECT data as a soft-prior in the FMT reconstruction to optimize the fusion of the two data types (Cao and Peter).

The current FMT system setup has high dynamic range and linear response and accurate localization at various depths as shown with phantom studies. However, several potential improvements of the fiber-based, video-rate FMT system can still be identified.

For instance, the sensitivity of the optical imaging in general is expected to decline with imaging depth, while SPECT has no depth limitation and easily extends to whole-body imaging. Possible extensions on the current design include extending the FMT field of view for more complete coverage. The DOT imaging array shape and size can be designed based on application. For example, the imaging array could have a cylindrical shape with extended sources and detectors for whole-body imaging. The potential for an expanded fiber array system with up to 48 sources and 48 detectors has been demonstrated for brain imaging in humans (White et al.). A higher-density imaging array could also potentially increase the resolution, particularly at the shallower depths for accurate localization of the target (Culver, Ntziachristos, et al.). A second limitation is the existence of distortion/artifacts on the x-ray CT images due to the high attenuation coefficient of borosilicate glass fibers compared to the bone. The possibility of whether switching to optical fibers composed of materials with lower attenuation than bone would reduce the artifacts remains a question for future investigation.

Another area of future work is to leverage the complementary contrast mechanisms of SPECT/FMT to evaluate biological mechanisms. MOMIAs that use activatable optical contrast mechanisms provide complementary information to the "always-on" SPECT information. SPECT can be used for whole-body imaging to localize the diseased tissue based on maps of the concentration of molecular targeted imaging agents while the FMT would report local molecular events, such as enzymatic activity, to monitor therapeutic response (H. Lee et al.).

3.5   Conclusion

We demonstrated integration of a fiber-based, video-rate fluorescence mediated tomography system with a preclinical NanoSPECT/CT platform. The video-rate FMT can accommodate the various imaging bore sizes of nuclear imaging systems due to the flexibility of the imaging fiber array. We used a monomolecular multimodal imaging agent such that the nuclear and optical signals emanated from the same regions to facilitate the fusion of both data-sets with high spatial precision. The depth profiling capability of the FMT was confirmed in phantoms by localizing MOMIA targets in tissue mimicking phantoms in the range of depths from 5-10 mm. The average absolute error between the COM of the optical and nuclear datasets for all three depths was 4.1 +/- 2.1 mm and the depth dependent spread of the volume of the FMT compared to the SPECT was 2.4 +/- 0.95 after thresholding at 30% maximum. For in vivo imaging, we used the anatomical X-ray CT data-sets to generate 3D finite-element model for light propagation. Co-localization of the MOMIA in both the FMT and SPECT contrasts was demonstrated. We also observed improvement in spatial correlation of the co-registered datasets after incorporating SPECT as a priori to constrain the FMT data reconstruction. The average spatial discrepancy of the LNs COMs between FMT and SPECT improved from 2.68 +/- 1.0 mm to 1.33 +/- 0.85 mm after incorporating the SPECT as a prior into the FMT reconstructions. These results suggest that integrated multimodal FMT/SPECT/CT has the potential to become a powerful and practical tool for a broad array of real time imaging applications.

Chapter 4

FMT/CT Guided Dynamic Imaging of Optical Tracers for Small Animal Imaging

4.1 Introduction

Dynamic fluorescence imaging is an emerging technology that can provide enhanced non-invasive functional and molecular level details and is a promising tool for detection of abnormal anatomical or physiological conditions based on kinetic parameters related to perfusion, pharmacokinetics, and tissue metabolism.

Currently, dynamic fluorescence imaging has been applied to studies of biodistribution of various optical agents in basic biological research (Achilefu and Dorshow; Amoozegar et al.; El-Desoky et al.; Goiffon et al.; Hillman et al.; Hillman and Moore; Patwardhan and Culver; Welsher, Sherlock and Dai). While dynamic imaging via fluorescence reflectance imaging (FRI) recently allowed segmentation of various internal organs based on their different kinetic behaviors(Hillman and Moore; Welsher, Sherlock and Dai), FRI sensitivity declines quickly with depth and a 2D geometry precludes co-registration with 3D modalities such as MRI, CT, PET or SPECT. Three-dimensional fluorescence mediated tomography (FMT) provides improved deep tissue sensitivity, volumetric localization and increased quantitative accuracy. FMT systems typically image on time scales of minutes to hours, which is too slow to monitor the uptake dynamics of a vascular injection.

In this work, we overcome this limitation and demonstrate dynamic tomography of fluorescent diagnostic imaging agents in healthy mice and in mice with liver disease. We demonstrate that video-rate FMT is fast enough to enable imaging of cardiac, respiratory and pharmacokinetic induced dynamic fluorescent signals and that the real-time uptake of injected agents can be deduced from these measurements. Fiber-based, video-rate FMT can additionally improve the flexibility of imaging by adapting to varying tissue

curvatures and performing simultaneous multiple point illumination and collection, thus increasing the imaging frame rate. In addition, for improved delineation of target tissues, we have combined FMT with CT to obtain complementary information. X-ray CT provides anatomical information while FMT provides dynamic functional information. Anatomically guided dynamic fluorescence mediated tomography was made possible by combining our recently published fiber-based, video-rate FMT system (Metasebya Solomon et al.) with preclinical NanoSPECT/CT (Bioscan).

Dynamic fluorescence mediated tomography (DyFMT) used in conjunction with tracer kinetic modeling promises to be an effective tool for non-invasive quantification of molecular imaging analysis (Liu et al.; Milstein, Webb and Bouman). Tracer kinetic modeling allows extraction of clinically or experimentally relevant information related to physiological and molecular processes. Kinetic models require two main measurements of tracer concentration over time as inputs (van den Hoff; Willemsen and van den Hoff). The two key measurements are tracer time course in arterial blood, used as a forcing function, and the corresponding tracer time course in the organ of interest, the "response."

Some challenges exist that limit the application of compartment modeling on a routine basis or for longitudinal studies relating to small animal imaging (Laforest et al.; van den Hoff; Willemsen and van den Hoff). The gold standard for obtaining an input function is through manual acquisition of arterial blood samples, a technique that yields a limited temporal resolution (Laforest et al.). In addition, frequent arterial blood sampling is an invasive technique that has multiple drawbacks. First, the number of arterial blood samples collected is limited because it is inconvenient and hard to access the small blood

vessels of small animals. Second, the amount of blood volume withdrawn is limited to a small fraction of the total blood volume of the animal to avoid blood depletion and keep the animal alive. Furthermore, the loss of blood may perturb the animal physiology and induce a bias in the experimental outcome. It may also limit or prevent repeated assessment of the same animal for longitudinal studies. Non-invasive techniques such as factor analysis methods and region-of-interest based (image-derived) input functions are proposed to resolve some of the challenges associated with serial arterial blood sampling for routine implementation of kinetic modeling in small animal studies (Laforest et al.; van den Hoff; van der Weerdt et al.; Willemsen and van den Hoff; Wu, Hoh, et al.; Wu, Huang, et al.; Hoekstra, Hoekstra and Lammertsma).

In this work, we propose to implement our application using a plasma input function, derived from dynamic FMT images. This approach is noninvasive in nature and helps simplify the scanning protocol. We demonstrate, for the first time, the feasibility of implementing time traces extracted from highly vascularized region-of-interest, the heart region, as image-derived input function (IDIF) for dynamic fluorescence tomography. The IDIF was validated against the reference input functions, arterial blood samples, to fulfill the requirement of compartmental modeling and kinetic parameter estimation for fluorescence dynamic imaging studies. The second input to the compartmental modeling, time resolved signal curves of target regions, was obtained from the fluorescence dynamic imaging series guided by organ locations shown in the corresponding X-ray CT data. Furthermore, feasibility studies were performed to distinguish healthy and diseased target regions uptake and clearance rates by implementing a two-compartment model. In summary, this technique provides a

powerful pharmacokinetic analysis of optical agents, with the potential for detecting the disease state of the internal organs and monitoring their response to therapeutic agents.

4.2   Materials and Method

4.2.1   Fiber-based, video-rate FMT System

For this study, we used our previously published fiber-based, video-rate fluorescence mediated tomography system, which consists of a grid of alternating 12 sources and 13 detectors (Metasebya Solomon et al.) Each source position is composed of two near infrared laser diodes (785 nm, Thorlabs DL7140-201S, and 830 nm, Thorlabs HL8325G) with dedicated drivers and control lines for each source to allow flexible software configurable source encoding (frequency- and time- encoding). Light sources are coupled into 2.5 mm diameter fiber bundles made of borasilicate glass sheathes with lightweight silicone. The detection channels use optically-filtered discrete avalanche photodiodes (Hamamatsu C5460-01) digitized with dedicated 24-bit analog-to-digital converters (MOTU HD 192). The custom made narrowband optical filters (CVI) have an 830 +/- 10 nm center wavelength and an out-of-band rejection of OD4, thus blocking the excitation light while passing the fluorescent and reference signals. An aspheric lens is used to collimate the light and optimize the blocking of the excitation light by the narrowband interference filter in order to enhance fluorescent signal detection. With this scheme, we acquire frequency-encoded fluorescence emission and reference transmission (used to normalize the measured fluorescence) light levels concurrently at each detector. This ratio-metric data allows DOT reconstructions using the normalized Born approximation, resulting in a map of quantified fluorochrome

89

distribution (Ntziachristos and Weissleder "Experimental Three-Dimensional Fluorescence Reconstruction of Diffuse Media by Use of a Normalized Born Approximation"). All data are acquired at frame rate of 30 Hz. A total of 88 measurements from source-detector pairs representing the first (6 mm) and second (13 mm) source-detector pairs are used for image reconstruction. The DOT imaging array composed of 3 cm wide by 3 cm high flexible silicone with right-angle fibers is integrated with the NanoSPECT/CT system.

The ratio-metric data of light intensities of transmission and fluorescent acquired concurrently at each detector is discretized according to the normalized Born approach to obtain $\mathbf{y=Ax}$, which is followed by direct inversion using a Moore-Penrose generalized method to obtain fluorescence image reconstruction (Culver, Siegel, et al.; Ntziachristos and Weissleder "Experimental Three-Dimensional Fluorescence Reconstruction of Diffuse Media by Use of a Normalized Born Approximation"; Patwardhan and Culver; M. Solomon, B. R. White, et al.; Zeff et al.). Optical properties at the reference wavelength of $\mu_a = 0.1$ cm^{-1} and $\mu'_s = 10$ cm^{-1} were used to model the optical properties of the mouse for in vivo studies (Cheong, Prahl and Welch). Further reconstruction and design details as well as capabilities of the fiber-based, video-rate FMT are detailed in a previous publication (Metasebya Solomon et al.).

4.2.2   CT Acquisition

For improved delineation of tissue/target volumes, we have combined FMT with microCT to obtain complementary information. X-ray CT provides anatomical information while FMT provides dynamic functional information. Our fiber-based,

video-rate FMT system was inserted into NanoSPECT/CT platform (Bioscan, Inc. Washington, D.C.) for co-registration of fluorescence and nuclear imaging data sets. The rat bed and 9-pinhole collimator sets were used to accommodate mouse and DOT imaging fiber array as previously described (chapter 3). The whole body CT scanning regions, including the DOT imaging pad, were selected by top-view topogram and the total acquisition time was 5 minutes. CT scanning was performed using a 45 KVP energy tube at 177 mA and 180 projections with 400 msec exposures with pitch of 1. CT projections were reconstructed using InvivoScope software (Bioscan, Inc. Washington, D.C.). The high-resolution NanoSPECT/CT anatomical data sets have isotropic voxel size of 0.4 mm.

4.2.3   Experimental Protocol

Animal handling and preparation was performed according to the guidelines approved by the Washington University School of Medicine Animal Studies Committee for humane care and use of laboratory animals. A flowchart of the acquisition timeline is presented in Figure 4.1. Mice (n= 5 healthy and n=6 mice with liver disease) were anesthetized with an intraperitoneal injection of ketamine (85 mg/kg) and xylazine (15 mg/kg) cocktail.

The dynamic fluorescence intensity was monitored for 10 minutes following tail vein bolus injection of 80 μM of ICG (Indocyanine green, Sigma-Aldrich, St Louis, MO) via a catheter secured in the tail vein. The DOT imaging fiber array was securely positioned on the ventral side of each mouse to image the heart, lung and liver regions (Figure 4.1B). We continuously acquired images at the rate of 30 frames per second (fps)

to capture the initial rapid change in signal levels associated with the uptake and washout of the optical tracer in the blood and different tissues, with maximum time resolution. Arterial blood samples were collected before and during the optical data acquisition period using micropipette tubes by capillary action. Initially, continuous blood sampling from the tail artery is achieved every 15 seconds for the first two minutes in order to capture the fast dynamics of the first few minutes of the contrast agent time course. The continuous sampling was performed every 1-minute until the end of the imaging session to minimize the effect of blood loss on the animal physiology. The micropipette tubes are then imaged using the Pearl near-infrared (NIR) fluorescence imaging system (LiCor Biosciences, Lincoln, NE).

To induce liver apoptosis, FasL (Jo2 clone, BD Pharmingen) was administered intraperitoneally into the mice (n=6) (0.15 ug/g) 4 hours before imaging (Ogasawara et al.; Janin et al.). FasL is a monoclonal antibody that targets ligand Fas receptors (also known as "Death" receptors) and activates apoptotic responses of hepatocytes and endothelial cells that express the Fas receptors (Ogasawara et al.; Janin et al.; Goetz et al.). At the end of the dynamic fluorescence data acquisition period, we also acquired anatomical X-ray CT data with and without the DOT fiber array using imaging protocol as described earlier without moving the animal.

For reference and verification of ex vivo ICG uptake by different organs, superficial fluorescence images of the excised organs were acquired at the end of imaging experiments after humane euthanasia using the Pearl near-infrared (NIR) reflectance fluorescence system. Healthy and diseased livers were isolated and fixed in 10 % formalin for hematoxylin and eosin (H&E) staining and histological analysis.

4.2.4 Segmentation

Using anatomical data of the mouse obtained from 3D X-ray CT projections (Figure 4.1C), we created a binary mask for each target regions (heart, lung and liver). The XYZ-coordinates of the mask are manually selected from the corresponding anatomical locations. A second anatomical X-ray image of mouse obtained with DOT fibers is used to obtain source-detector positions (Figure 4.1B). An affine transformation is performed to transform the masks XYZ-coordinates into a DOT space for multiplication with the reconstructed fluorescence dynamic data to extract its corresponding time courses by averaging the voxels fluorescence intensity. The accurate segmentation of the different functional regions is key since the average voxel time trace is dependent on it. Any change of the time trace, for example delay in time, might lead to an error in kinetic parameters estimation. To address this issue, we selected the masks coordinates well within the target regions.
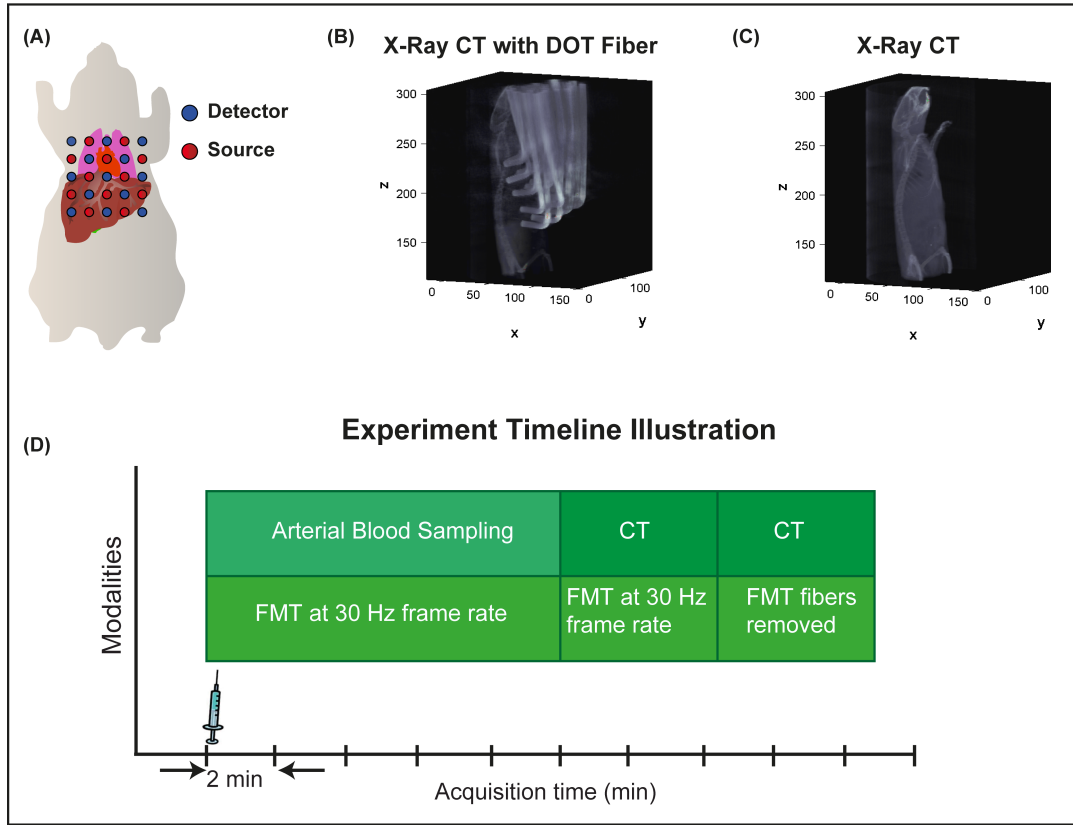
Figure 4.1: Dynamic Fluorescence and Anatomical Data Acquisition Protocol. (A) Schematic showing the placement of the fiber array on ventral side of a mouse to demonstrate the source-detector arrangement and the imaging field-of-view. (B) X-ray CT image with the fiber array of DOT used to obtain source-detector positions for anatomical co-registration of the dynamic FMT data. (C) An X-ray CT is used to capture the three-dimension structure of the anatomy of a mouse for segmentation of target regions. (D) Timeline of the fluorescence and anatomical data acquisition protocol.

4.2.5   Compartment Modeling

First, the feasibility of implementing a region-of-interest based forcing function was validated against the reference arterial blood samples. Serial arterial blood samples were collected as the gold standard for pharmacokinetic analysis for validation of dynamic fluorescence imaging. Image-derived input functions (IDIF) were constructed from heart region time traces. Temporal correlations were determined using Pearson correlation of the heart region time traces with corresponding reference arterial blood samples, thus producing correlation r-value for each mouse. Second, the IDIF was used as input for a two-compartment model to estimate and assess ICG pharmacokinetics in healthy mice and mice with liver disease extracted time traces from lung and liver regions. To assess the in vivo pharmacokinetics of ICG in the liver and lung with and without drug treatment, a widely used two-compartment trapping model with three parameters was employed (Figure 4.2)(Willemsen and van den Hoff; van den Hoff).

The "vasculature" compartment represents the kinetics of ICG remaining in systemic circulation. The clearance of ICG from the systemic circulation is attributed to its trapping and excretion exclusively into the bile through the liver without undergoing any biotransformation. In this model, the "tissue" compartment is split into two-compartments – EES and Internalized. We postulate that free ICG in the blood can reversibly extravasate into the tissue while no extravasation from albumin bound ICG to tissue is expected except in the liver (Berezin, Guo, Akers, et al.). Therefore, the "Extracellular Extravascular Space" compartment represents the time-resolved reversible extravasation of ICG in different organs of interest (lung and liver). The forward and reverse rate-constants of ICG between the blood and tissue are denoted by k_1 (sec^{-1}) and

k_2 (sec^{-1}), respectively. The "Internalized" compartment represents the concentration of ICG that remained trapped in the tissue during the data acquisition period. The tracer is trapped into the tissue at a rate constant of k_3 (sec^{-1}).

The tissue compartment, C_T, is represented as the solution to a linear differential equation (Eq 1) derived assuming that rates of transport are given by a rate constant multiplied by the concentration of the different compartments of our model (Berezin, Guo, Akers, et al.; Willemsen and van den Hoff; van den Hoff). The solution of the differential equation is convolved with the image-derived forcing function, C_{bl} (Eq2) (Willemsen and van den Hoff; van den Hoff). Next, the output of the convolution is used as an input and the Nelder-Mead Simplex algorithm is used to optimize the kinetic parameters k_1 through k_3 against the target regions dynamic FMT data. This is implemented through the *fminsearch* function in Matlab (MatLab 7.14, The MathWorks, Inc. Natick, MA). The overall uptake rate constant of ICG (K) (Eq 3) in the liver and lung is computed to compare their difference in overall ICG uptake rate (Willemsen and van den Hoff; van den Hoff). The accuracy of the fitted ICG curves were compared and validated against their matching dynamic FMT data using Pearson correlation.

$$\frac{dC_T}{dt} = k_1 * C_{bl}(t) - (k_2 + k_3) * C_T(t) \qquad 1$$

$$C_T = C_{bl}(t) \otimes \frac{k_1}{k_2 + k_3}\left(k_3 + k_2 * e^{(-(k_2+k_3)t)}\right) \quad 2$$

$$K = \frac{k_1 \times k_3}{k_2 + k_3} \qquad\qquad 3$$
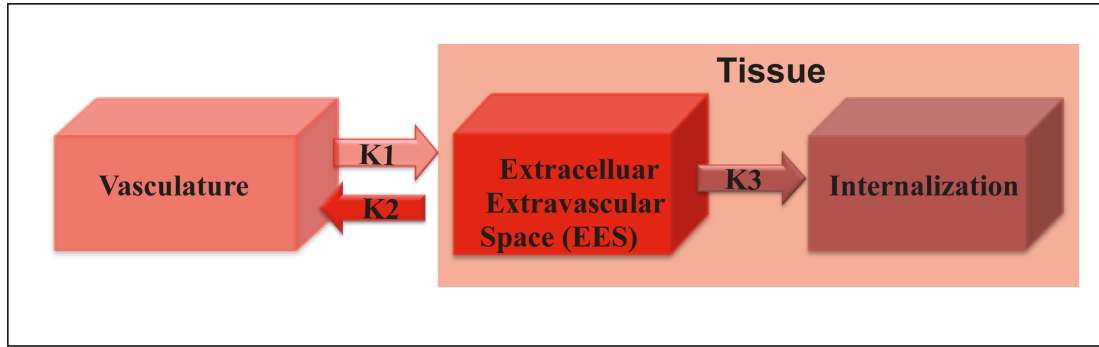
Figure 4.2: Two-compartment model implemented to estimate ICG kinetic rate constants (k1, k2 and k3 (sec^{-1})) of the lung and liver tissues in healthy mice and mice with liver disease.

4.3   Results

The goal of this study was to demonstrate the feasibility of implementing video-rate, fiber-based FMT-CT as a fast and non-invasive tool to obtain IDIF and assess organ function based on the quantitative output of kinetic modeling. The different processing steps involved in obtaining image-derived input functions and kinetic modeling steps to estimate rate constants of regions-of-interest are outlined in Figure 4.3.

Fluorescence concentrations over time were obtained from the dynamic imaging series for target regions (heart, lung and liver) guided by their corresponding anatomical x-ray CT data (Figure 4.4 and Figure 4.5). Figure 4.4 illustrates typical subject-specific masks definition of regions-of-interest manually generated from anatomical X-ray CT projections. The masks are used to constrain reconstructed FMT data and obtain ICG dynamics for anatomically defined regions.
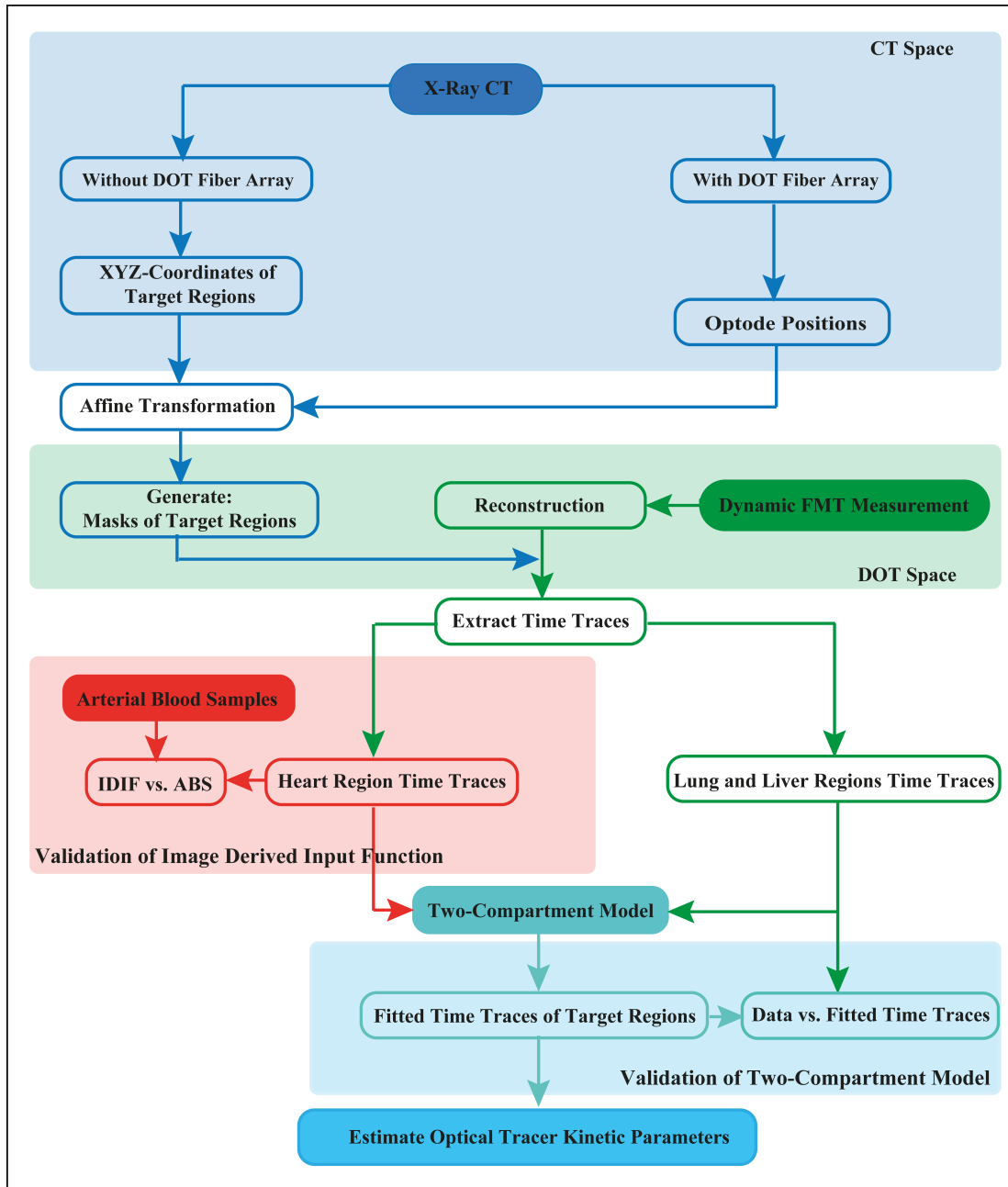
Figure 4.3: Flow chart demonstrating steps towards quantitative fluorescence mediated tomography (FMT). IDIF= Image-Derived Input Function, ABS= Arterial Blood Samples.
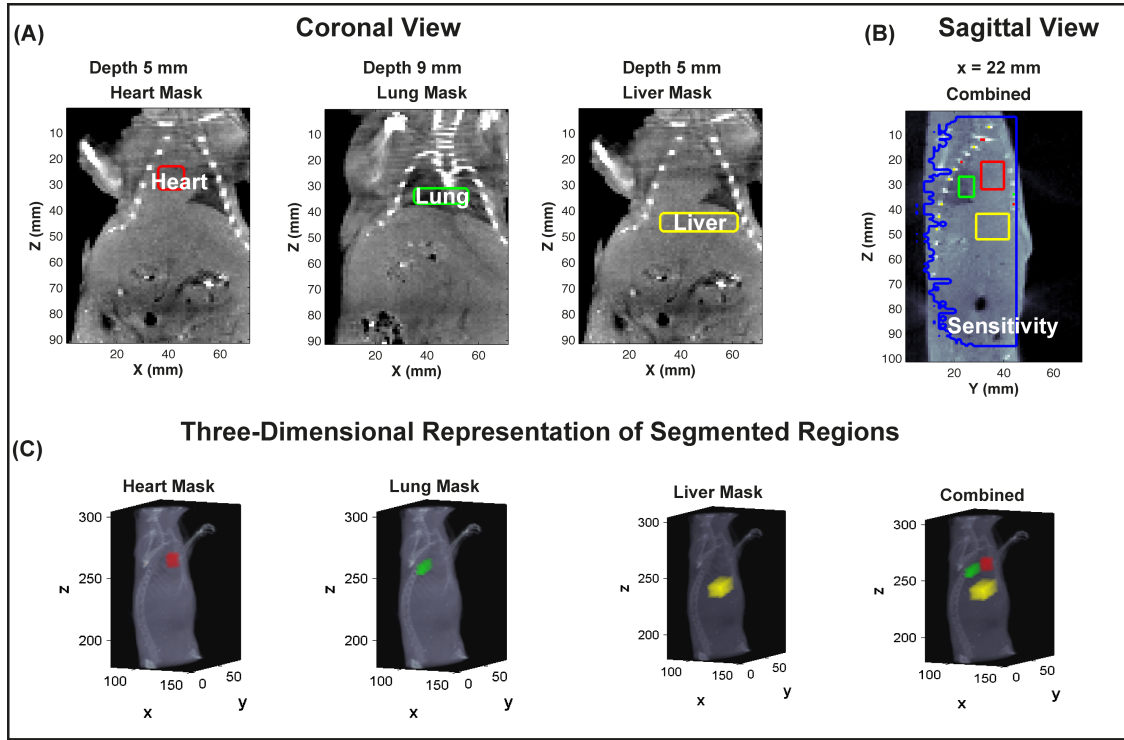
Figure 4.4: Illustration of typical masks definition of target regions generated from anatomical X-ray CT data. (A) Representative coronal view of heart, lung, and liver (left to right) regions masks combined with the corresponding X-ray CT data. (B) Representative sagittal view to demonstrate the depth profile of the combined target regions masks and the profile of the DOT sensitivity matrix (blue). The target regions are within the DOT sensitivity. (C) Three-dimensional representation of the heart, lung and liver masks co-registered with its anatomical X-ray CT data. The far right image is the combined heart, lung and liver masks co-registered with its corresponding X-ray CT data. The masks are used to extract their corresponding ICG time courses to estimate the kinetic rate constants of each region of interest.

The DOT images of ICG dynamics of heart, lung and liver regions were co-registered with its corresponding anatomical X-ray CT projections for healthy and anti-Fas-treated groups (Figure 4.5). Representative sagittal and coronal views of the target regions masks are shown in Figures 4.5A and 4.5C. Coronal slices that best display the dynamic fluorescence data from the heart, lung and liver are shown in Figure 4.5B and 4.5D. Representative time traces extracted from target organs corresponding to their anatomical locations demonstrated distinct ICG dynamics due to their different ICG pharmacokinetics (in healthy mouse (Figure 4.5E) and averaged over all five healthy mice and all six mice with liver disease (Figure 4.5F)). Each organ demonstrated distinct ICG dynamics due to their different ICG pharmacokinetics. The time traces demonstrated ICG accumulation in the liver, which is associated with ICG uptake by hepatocytes prior to elimination in the bile. In contrast fluorescence signal from heart and lung regions rapidly decreased during the same time period, corresponding to ICG clearance from the blood.
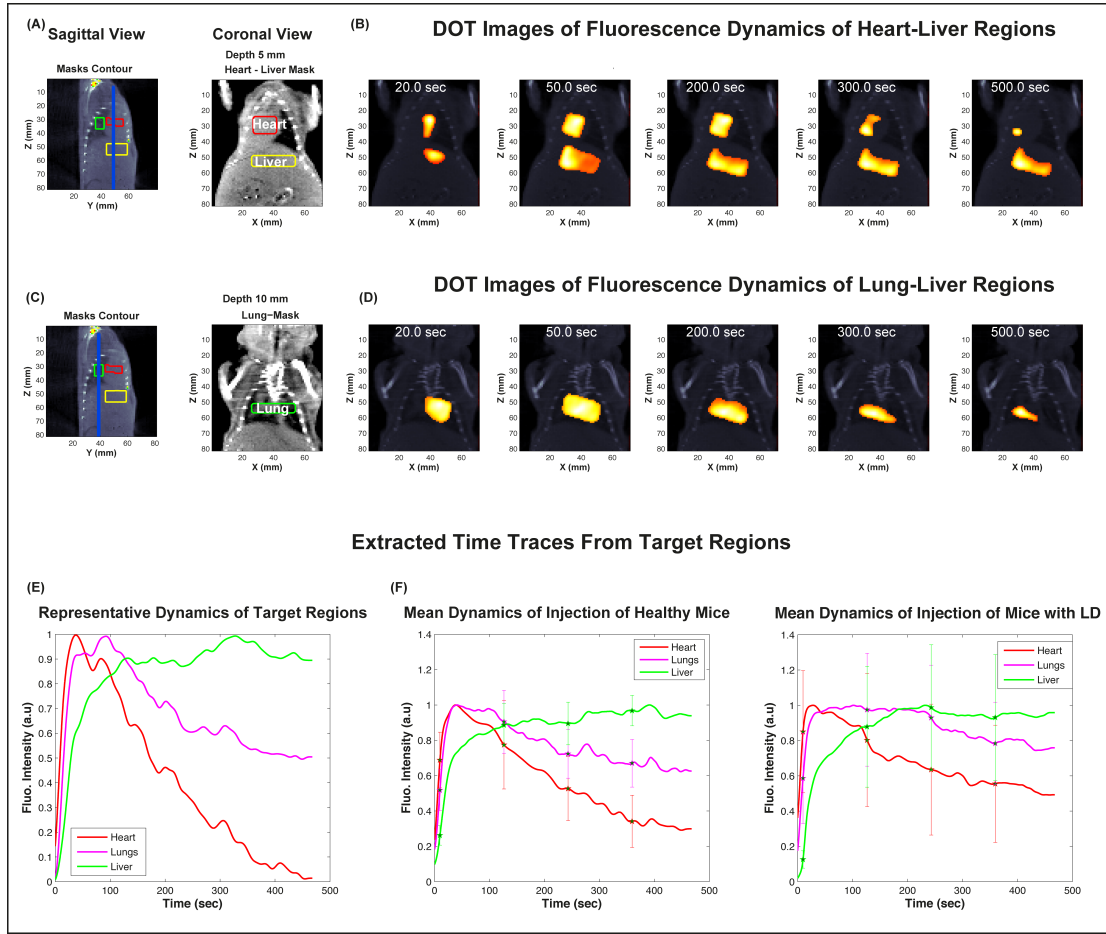
Figure 4.5: Imaging of ICG Dynamics in Mice. (A & C) Sagittal and coronal views of the combined heart-liver masks (left to right). The blue lines of the sagittal views indicate the position of the coronal slice used to display the dynamic FMT-CT data. (B & D) Coronal view of the reconstructed fluorescence dynamic tomography, after segmentation, and co-registered with its corresponding anatomical X-ray CT following bolus injection of ICG into the tail vein of a healthy mouse. (E) Average time courses of pixels extracted from the heart, lung and liver regions of a representative healthy mouse shown above. Each organ demonstrates distinct ICG dynamics due to their different ICG pharmacokinetics. (F) The dynamics of ICG of heart, lung and liver regions averaged over 5 healthy mice and over 6 mice with experimentally induced liver apoptosis (left to right). The time traces demonstrate ICG accumulation in the liver while the signal decreases over time in the heart and lung regions, which is associated with ICG clearance. In addition, the time traces of mice with liver disease show high standard deviation, which can be associated with the subject specific response to the FasL treatment that can indirectly induce high variation on ICG pharmacokinetics.

The feasibility of implementing time traces derived from the heart, as forcing function for a two compartment model was validated against the gold standard method, arterial blood samples. Time traces of ICG in collected serial arterial blood samples shows similar dynamics to its corresponding time traces derived from the heart region (in a representative mouse Figure 4.6A and averaged over all fiver healthy mice and six mice with liver disease Figure 4.6B and 4.6C respectively). Time traces of the IDIF are highly correlated temporally with their corresponding arterial blood samples with a mean Pearson correlation coefficient of 0.95 ± 0.024 and 0.86 ± 0.083 in healthy mice (Table 4.1) and in mice with liver disease (Table 4.2) respectively. The high correlations demonstrate that the time courses from the heart region can be used as an image-derived forcing function for a two-compartment model to estimate ICG kinetic parameters of the target regions, the lung and liver.
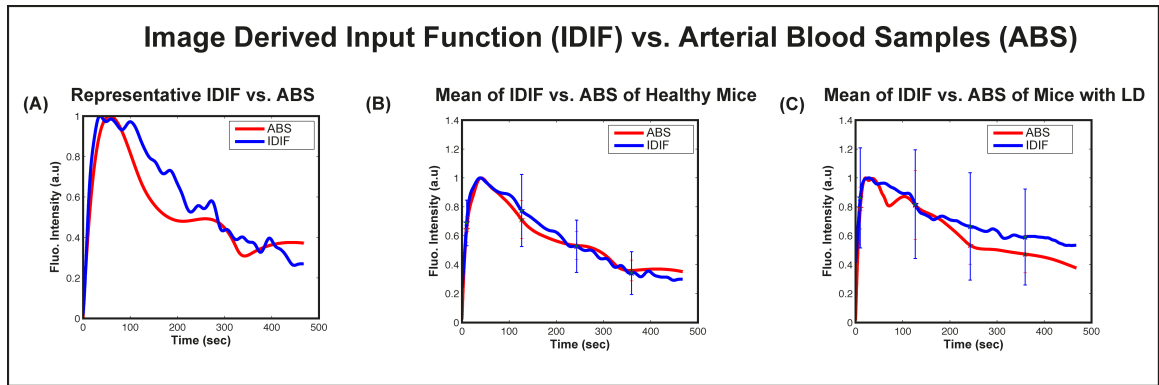
Figure 4.6: Validation of Image-Derived Input Function (IDIF) with Interpolated Serial Arterial Blood Samples. (A) Time traces of ICG in collected serial arterial blood samples compared to its corresponding time courses from heart region of a representative healthy mouse. (B & C) Mean time courses of ICG dynamics in systemic circulation and time courses extracted from heart regions and averaged of 5 healthy mice and 6 mice with liver disease. The heart region are highly correlated with the arterial blood samples with Pearson correlation coefficient of r=0.95 +/- 0.024 and 0.86 +/- 0.083 in healthy mice and mice with liver disease respectively.

Moreover, we demonstrated the feasibility of evaluating organs function by comparing ICG kinetic parameters in regions-of-interest in mice with induced hepatic apoptosis and healthy mice. Target regions (lung and liver) measurements and their corresponding IDIF were used as inputs for the proposed two-compartment model. The estimated ICG kinetic rate constants of liver and lung regions demonstrate the feasibility of distinguishing different organs as well as healthy vs. diseased organs. Using the two-compartment model, each fitted ICG concentration curve shows high temporal correlation with the corresponding lung and liver ICG time courses data (r= 0.95 ± 0.059 and 0.95 ± 0.028 for lung and liver regions respectively) in healthy mice (Figures 4.7A and 4.7B and Table 4.1). There is also high correlation between each fitted ICG concentration curve and the corresponding lung and liver time courses data (r= 0.92 ± 0.047 and 0.92 ± 0.042 for lung and liver data respectively) in mice with liver apoptosis (see Figures 4.7C and 4.7D and Table 4.2).
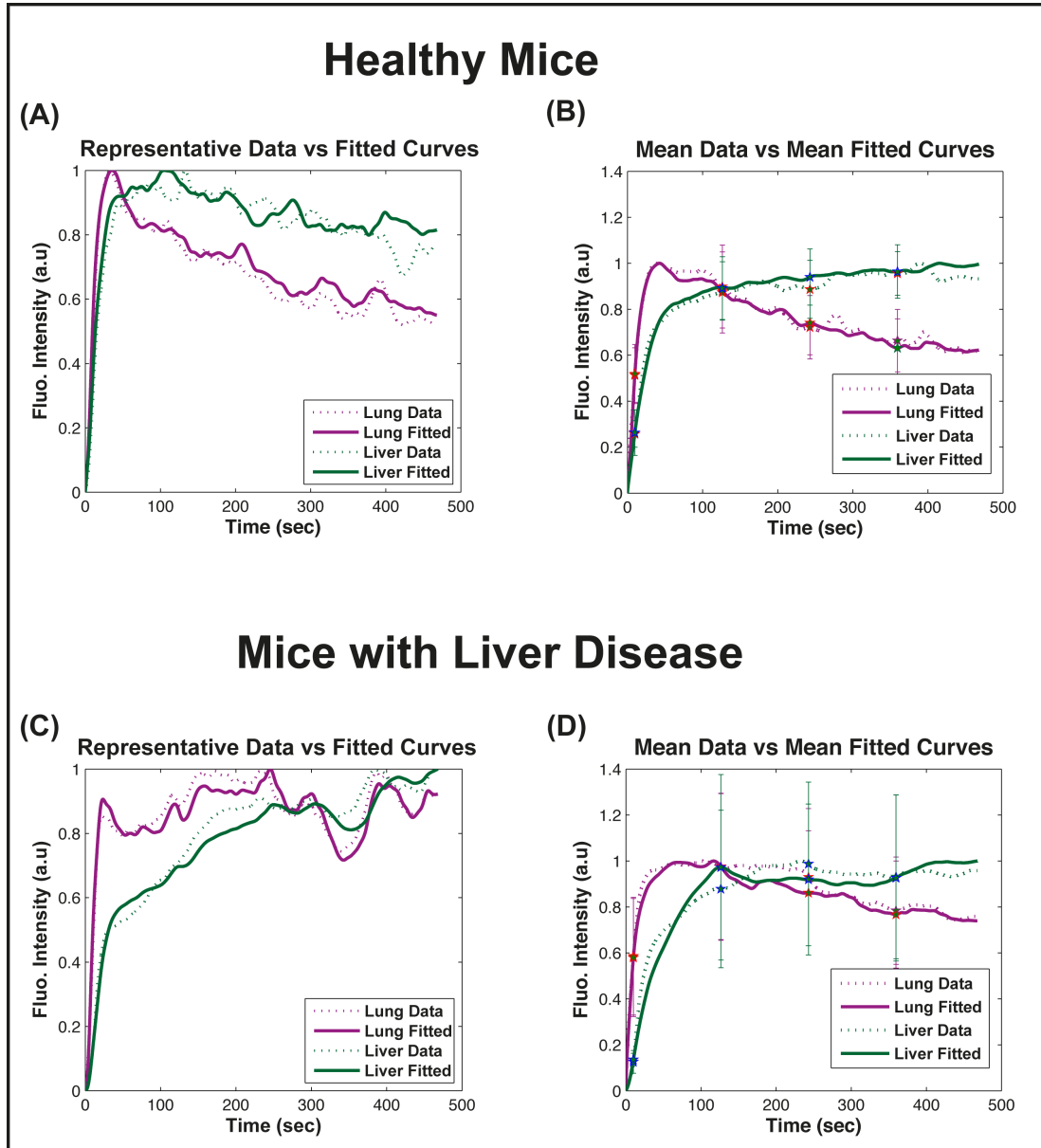
Figure 4.7: (A & C) Examples of lung and liver regions fitted ICG time courses using the two-compartment model and their corresponding time courses obtained from a healthy mouse and mouse with experimentally induced liver disease respectively. (B & D) Mean dynamics of lung and liver regions ICG time courses and their corresponding fitted ICG time traces using the proposed two-compartment model averaged over 5 healthy mice and 6 mice with liver disease respectively. Each fitted ICG concentration curve shows high correlation with the corresponding lung ICG time courses data with mean Pearson correlation coefficient of, r, 0.95 +/- 0.059 and 0.92 +/- 0.047 for healthy mice and mice with liver disease respectively. Each fitted liver ICG concentration curve is highly correlated with the corresponding liver ICG time courses data with mean

Pearson correlation coefficient of, r, 0.95 +/- 0.028 and 0.92+/- 0.042 for healthy mice and mice with liver disease respectively.

The average overall uptake rates of liver and lung in healthy mice were 7.4×10^{-4} +/- 5.6×10^{-4} sec^{-1} and 4.48×10^{-6} +/- 1.92×10^{-6} sec^{-1} respectively, which confirms that ICG is trapped hundredfold time more in the liver (Figure 4.8A) and that lung lower permeability and retention rate of ICG. The liver damage alter the kinetics of ICG compared to healthy mice as displayed by the increase in the overall rate constant of lung and liver in diseased mice as shown in Figure 4.8B. For example, the observed delay in excretion rate of ICG from the systemic circulation in mice with hepatic apoptosis was caused by the sluggish ICG uptake rate of diseased liver (Table 4.3). The mean ICG uptake rate (k_1) of liver in mice with liver disease was decreased from 0.02 ± 0.022 sec^{-1} to 0.013 ± 0.0094 sec^{-1}. The mean reverse rate (k_2) was also diminished in mice with liver apoptosis to 0.074 ± 0.66 sec^{-1} from 0.12 ± 0.11 sec^{-1}. The ICG internalization by hepatocytes was elevated from 0.0055 ± 0.0024 sec^{-1} in healthy mice to 0.0092 ± 0.012 sec^{-1} in mice with liver disease. ICG is mainly cleared through the liver into the bile without undergoing any modification.

In addition, there was also an observed increase in the uptake and clearance rate of ICG in lung of mice with liver disease compared to healthy mice (Table 4.3). For instance, we observed an increase in lung mean uptake rate of (k_1) in mice with liver disease from $6.8 \times 10^{-4} \pm 3.7 \times 10^{-4}$ sec^{-1} to 0.0161 ± 0.0094 sec^{-1}. The mean reverse rate (k_2) had also increased from 0.29 ± 0.21 sec^{-1} to 0.48 ± 0.39 sec^{-1} in mice with liver disease. The ICG retention rate in lung cells was elevated from 0.0019 ± 0.0011 sec^{-1} to 0.0031 ± 0.0036 sec^{-1} in mice with liver disease. Moreover, the average overall ICG

uptake rate of liver and lung increased from 7.4×10^{-4} to 1.48×10^{-3} sec^{-1} and 4.46×10^{-6} to 1.03×10^{-3} sec^{-1}, respectively. The observed increase in overall ICG rate constant of lung and liver (Figure 4.8B) is associated with leaky vasculature and cell membranes due to the experimentally induced endothelial cell apoptosis and vascular lesions after FasL administration (Ogasawara et al.; Janin et al.).
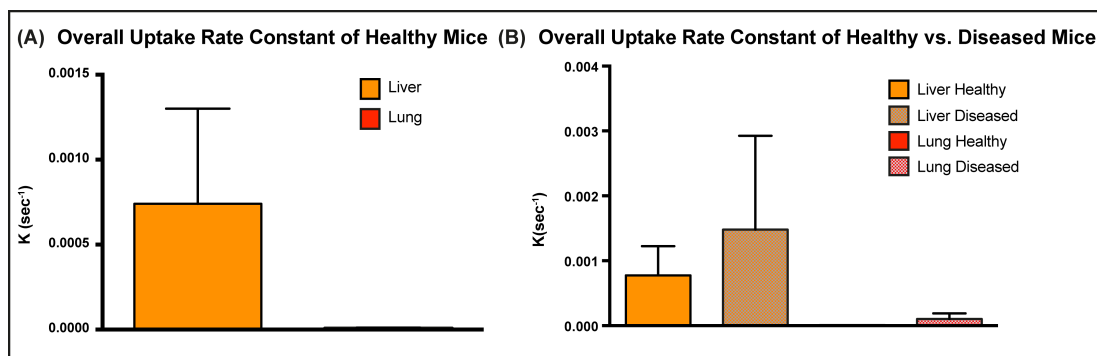
Figure 4. 8: Overall ICG uptake rate constant of lung and liver regions. (A) Comparison of the overall uptake rates of liver and lung regions in healthy mice. The mean overall uptake rates of liver and lung are 7.4×10^{-4} +/- 5.6×10^{-4} sec^{-1} and 4.48×10^{-6} +/- 1.92×10^{-6} sec^{-1} respectively, which confirms that ICG is trapped hundredfold time more in the liver (Figure 8A) and that lung lower permeability and retention rate of ICG. (B) Comparison of the overall uptake rates of liver and lung regions in healthy mice with anti-Fas treated group of mice. The average overall ICG uptake rate of liver and lung increased from 7.4×10^{-4} to 1.48×10^{-3} sec^{-1} and 4.46×10^{-6} to 1.03×10^{-3} sec^{-1}, respectively

The change in kinetic parameters is associated with the induced morphological changes of hepatocytes (cell bodies and the nucleus) and endothelial cells that express Fas receptors (Ogasawara et al.; Janin et al.). Liver section histology verified morphological changes of the cell bodies and nucleus as a result of the induced apoptosis 4 hours after administering FasL compared to healthy liver (Figure 4.9). The extent and severity of the liver apoptosis after the FasL treatment is subject specific as

shown in Figure 4.9B. This could be the cause of the high variation (standard deviation) observed in the ICG time courses of mice with liver disease.
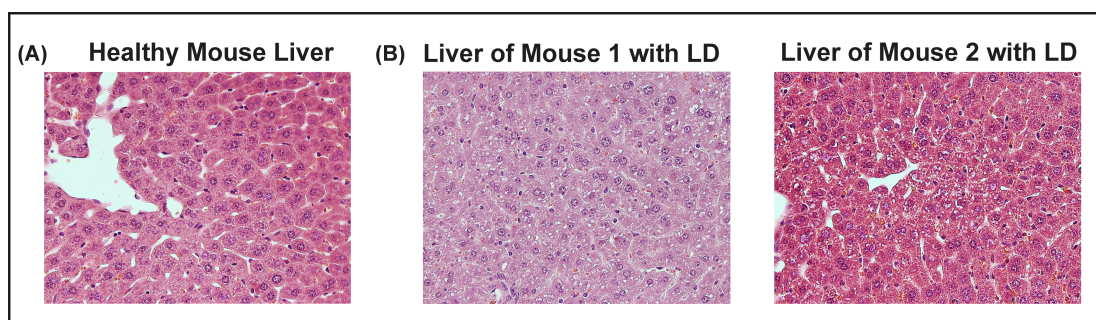
Figure 4.9: Histological analysis of liver sections of healthy mice and mice with experimentally induced liver apoptosis. (A & B) Examples of hematoxylin and easin (H&E) stained healthy and diseased liver sections respectively. The H&E stained liver sections demonstrate morphological changes of the cell bodies and the nucleus as the result of the induced liver apoptosis 4 hours after administering FasL. The extent of liver apoptosis after the FasL treatment is subject specific as shown as an example for two different mice in B. LD= Liver Disease.

	Healthy Mice Pearson Correlation Coefficient (r^2)					
	1	2	3	4	5	Mean +/- STD
IDIF vs. ABS	0.96	0.92	0.93	0.97	0.97	**0.95 +/- 0.024**
Liver Data vs. Fitted Curve	0.99	0.97	0.94	0.92	0.93	**0.95 +/- 0.028**
Lung Data vs. Fitted Curve	0.99	0.93	0.99	0.99	0.85	**0.95 +/- 0.056**

Table 4.1: Validation of image derived input function (IDIF) against the reference arterial blood samples (ABS) and comparison of the two-compartment model output with the corresponding dynamic FMT data of healthy mice.

	Mice with Liver Disease Pearson Correlation Coefficient (r^2)						
	1	2	3	4	5	6	Mean +/- STD
IDIF vs. ABS	0.94	0.76	0.76	0.95	0.85	0.87	**0.86 +/- 0.083**
Liver Data vs. Fitted Curve	0.88	0.9	0.98	0.9	0.92	0.97	**0.92 +/- 0.042**
Lung Data vs. Fitted Curve	0.95	0.93	0.97	0.92	0.83	0.91	**0.92 +/- 0.047**

Table 4.2: Validation of image derived input function (IDIF) against the reference arterial blood samples (ABS) and comparison of the two-compartment model output with the corresponding dynamic FMT data mice with experimentally induced liver apoptosis.

	Healthy Mice Mean +/- STD			Mice with Liver Disease Mean +/- STD		
	k_1 (sec^{-1})	k_2 (sec^{-1})	k_3 (sec^{-1})	k_1 (sec^{-1})	k_2 (sec^{-1})	k_3 (sec^{-1})
Liver	0.0195 +/- 0.022	0.133 +/- 0.113	0.0055 +/- 0.0024	0.0134 +/- 0.0094	0.074 +/- 0.066	0.0092 +/- 0.012
Lung	6.8×10^{-4} +/- 3.7×10^{-4}	0.29 +/- 0.21	0.0019 +/- 0.0011	0.0161 +/- 0.0094	0.48 +/- 0.39	0.0031 +/- 0.0036

Table 4. 3: Rate Constants of ICG Pharmacokinetics in the Lung and Liver of Healthy Mice and Mice with Liver Disease. The observed increase in ICG rate constants of lung is associated with the experimentally induced endothelial cell apoptosis and vascular lesions after FasL administration. The slow excretion rate of ICG from the systemic circulation in mice with liver disease compared to healthy mice can be associated to the sluggish ICG uptake rate of the liver in mice with liver disease. ICG is mainly cleared through the liver into the bile without undergoing any modification.

4.4   Discussion

Dynamic FMT systems can be used to determine the biodistribution of a multitude of injectable agents and can be used in conjunction with organ specific dyes to acquire a general assessment of organ function. We presented DyFMT as preclinical imaging tool for assessing alterations in fluorescent tracer pharmacokinetics pharmacokinetics and biodistribution in relation to disease states.

In this study, we imaged healthy and diseased mice with high temporal resolution, during the disappearance of ICG from systemic circulation, the heart, and its time resolved uptake in the liver and lung. ICG is a well-characterized probe, approved for a variety of clinical endpoints such as measuring the hepatic blood flow to test liver function (El-Desoky et al.; Kimura et al.; Ott; Seifalian et al.). ICG binds to plasma proteins, such as albumin, and is mainly removed from the circulation by the liver (Ott; Berezin, Guo, Akers, et al.). Dynamic fluorescence mediated tomography (DyFMT) was made possible by co-registering data collected using our fiber based, video-rate FMT system (Metasebya Solomon et al.) with preclinical microCT data as an anatomical reference. To extract ICG concentration over time from our DyFMT data in selected regions of interest, we choose three ROIs, one in the heart, lung and in liver based on manual segmentation guided by anatomical x-ray CT projections.

A measurement of the input function is required for most models characterizing the kinetic behavior of substances of interest in tissue in vivo. Measurement of the plasma input function enables accurate quantification of dynamic FMT data. Derivation of the input function from DyFMT images is the most attractive method because of its non-invasive nature and because it simplifies the scanning protocol. Therefore, we

demonstrated the feasibility of implementing time traces from the heart region as image-derived forcing function. We demonstrated that there is high temporal correlation between IDIF and its corresponding reference arterial blood samples for each mouse. Obviously, blood sampling is very invasive and very inconvenient for small animal imaging especially due to their small blood vessels and small blood volume. The mean Pearson r-values were 0.95 ± 0.024 and 0.86 ± 0.083 in healthy mice and in mice with liver disease respectively.

We demonstrated the feasibility of distinguishing the uptake rate of two different organs, lung and liver. The overall ICG uptake rate of liver was hundredfold higher than the lung as expected since ICG is mainly cleared through the liver. Furthermore, we demonstrated the feasibility of distinguishing healthy vs. diseased organs based on significant difference between the estimated ICG kinetic rate constants of liver and lung regions in healthy mice and mice with hepatic disease. For instance, we observed a decrease in plasma clearance of ICG in diseased mice, which is associated with the slow transport rate through the plasma membrane of hepatocyte. The estimated k_1 value, which decreased from 0.02 ± 0.022 in healthy mice to 0.013 ± 0.0094 in diseased mice, successfully predicted the status of the hepatic function. In addition, we observed an increase in the ICG rate constants of the lung and liver. The average overall ICG uptake rate of liver and lung, for instance, increased from 7.4×10^{-4} to 1.48×10^{-3} sec^{-1} and 4.46×10^{-6} to 1.03×10^{-3} sec^{-1}, respectively. The fitted ICG concentration curves generated using the two-compartment model showed high temporal correlation with the corresponding lung and liver ICG time courses data in healthy mice and mice with liver disease (r-values were 0.95 ± 0.059 and 0.95 ± 0.028 for lung and liver regions of healthy mice

respectively and 0.92 ± 0.047 and 0.92 ± 0.042 for lung and liver respectively in diseased mice). The difference between healthy and diseased mice kinetic parameters of the lung and liver is associated with the induced morphological changes of cell bodies and the nucleus (in liver) and endothelial cells that express Fas receptors (in both lung and liver) as previously shown in the literature (Goetz et al.; Janin et al.; Ogasawara et al.).

Previous two-dimensional fluorescence reflectance imaging (FRI) has been used to monitor the biodistribution of newly developed contrast agents and effects of drugs on excretory systems function (Achilefu and Dorshow; Hillman and Moore; Hillman et al.; Welsher, Sherlock and Dai; Amoozegar et al.). For instance, dynamic imaging via fluorescence reflectance imaging (FRI) recently allowed segmentation of various internal organs (Hillman and Moore; Welsher, Sherlock and Dai); In addition, Amoozegar et al. has further demonstrated the capacity of dynamic FRI to evaluate healthy and diseased organs based on the presence of abnormally altered time courses (Amoozegar et al.). The study showed change in ICG uptake rates in the liver and kidney following liver damage compared to healthy animals by visual assessment and comparison with ex-vivo studies. The strength of the current DyFMT-CT study is that we further extended this approach by implementing a two-compartment model to quantify the extent of damage on the target organs based on the changes of the kinetic parameters. Furthermore, the current DyFMT-CT system has improved deep tissue sensitivity, volumetric localization and increased quantitative accuracy compared to the dynamic FRI.

The feasibility of fluorescence tomography for in vivo dynamic imaging has been previously reported (Alacam and Yazici; Alacam, Yazici, Intes, et al.; Alacam, Yazici, Intes, Nioka, et al.; Alacam, Yazici, Serdaroglu, et al.; Cuccia et al.). For instance, Liu et

al. quantified the uptake and washout rate of ICG in the liver, where optical imaging was acquired at a 1.1 min/frame using their hybrid fluorescence DOT and micro-CT system (Liu et al.). The rate constants (uptake rate (k_1=0.0036 sec^{-1}) and washout rate of (k_3=0.00069 sec^{-1})) were ten times slower than we predicted, which could be associated to the slow acquisition rate incapability to capture the fast dynamics of liver. Moreover, their image acquisition time, 1.1min/frame is unsuitable for capturing fast dynamics of the first few minutes in regions such as the heart, although it may be adequate for the slow dynamics of the liver. In addition, image acquisition times in the range of minutes is unsuitable for capturing the early fast-changing signals associated with various optical contrast agents. To a significant extent, the system presented in this paper addresses many of these difficulties.

The difficulty in FMT image segmentation is compound by the low spatial resolution in optical imaging, which rapidly degrades with imaging depth due to the high scattering of light in tissues (Hillman et al.). Therefore, optical imaging can leverage anatomical information to improve accuracy during processing and image reconstruction. For instance, we implemented manual segmentation to extract relative ICG concentration from three target regions. An important future area of work is in incorporating automatic or semi-automatic statistical clustering algorithms. The possibility of implementing segmentation algorithm to delineate the different organs based on differences in the kinetics of injected contrast agents also remains a question for future investigation. Another limitation of low spatial resolution is spillover and partial volume effects that would affect the accuracy of ROI based input functions. The spillover and partial volume effects on the selected ROIs have not been corrected for in

this study. Therefore, another area of future work is to adapt spillover and partial volume correction algorithms developed for dynamic PET and MRI imaging systems for DyFMT platform (Fang and Muzic; Laforest et al.; van der Weerdt et al.; Wu, Hoh, et al.; Wu, Huang, et al.). With these improvements, the accuracy of IDIF would remain consistent across multiple optical contrast agents despite the variance introduced by their different perfusion rates.

The current FMT system setup has high dynamic range and linear response and accurate localization at various depths as shown in previous studies (Metasebya Solomon et al.). However, several potential improvements of the fiber-based, video-rate FMT system can still be identified. Possible extensions on the current design include extending the FMT field of view for whole-body imaging. The DOT imaging array shape and size can be designed based on the individual application. For example, the imaging array could have a cylindrical shape with extended sources and detectors for whole-body coverage. The potential for an expanded fiber array system with up to 48 sources and 48 detectors has been demonstrated for brain imaging in humans (White et al.). A higher-density imaging array could also potentially increase the resolution, particularly at the shallower depths for accurate estimation of the IDIF (Culver, Ntziachristos, et al.).

4.5   Conclusion

In this study, we presented video-rate, fiber-based FMT, a non-invasive in vivo imaging tool for quantitative pharmacokinetics and biodistribution studies. We imaged, with high temporal resolution, the disappearance rate of ICG from systemic circulation and its time-resolved uptake and clearance in the liver and lung in healthy mice and mice

with experimentally induced acute hepatic apoptosis. In addition, we validated the feasibility of implementing time traces extracted from highly vascularized region-of-interest as a forcing function rather than acquiring arterial blood samples invasively. The time courses of the heart region are used as an image-derived input function for a two-compartment model to compute the uptake and clearance rate of ICG from the lung and liver regions. Comparisons between the ICG kinetics parameters before and after drug treatment demonstrate the capacity to assess organ function and drug-related acute toxicity. Although we have used a linear compartment model in these studies, more complex models could be used successfully. In summary, tracer kinetic modeling combined with fluorescence dynamic tomography provides a powerful pharmacokinetic analysis tool using newly developed diagnostic optical agents with a potential for detecting the disease state affecting internal organs and monitoring their response to therapeutic agents.

Chapter 5

Detection of Enzyme Activity in Orthotopic Murine Breast Cancer by Fluorescence Lifetime Imaging Using Fluorescence Resonance Energy Transfer-based Molecular Probe

5.1 Introduction

Molecular signatures of cancer tissues include up-regulated signaling receptors and enzyme expression. For example, up-regulation of integrin receptors in tumors is associated with metastatic spread (Sloan et al.). Likewise, increased activity of members of the matrix metalloproteinase (MMPs) family by in cancer tissue can also be an indication of metastatic potential (Roy, Yang and Moses). Enzyme activity can be diagnostic and prognostic in cancer and other diseases. For instance, MMPs are biomarkers for diagnosis and prognosis in cancer as they have been implicated as mediators of tumor growth, invasion and metastasis (Bremer, Tung and Weissleder; Himelstein et al.; Fingleton; Weissleder et al.). MMP inhibitors are under investigation as anti-cancer agents (Roy, Yang and Moses).

Preclinical optical imaging with fluorescent contrast agents has become prominent in recent years due to the high sensitivity and high throughput nature of this versatile modality. Fluorescent molecular probes can be administered for rapid detection of disease throughout the body of small animals, economically and without ionizing radiation. Fluorescence techniques can be further enhanced by sensing mechanisms such as spectral shifts, quenching and fluorescence lifetime changes that may occur due to molecular interactions and environmental conditions. Optical imaging with fluorescent molecular probes is an economical, high throughput modality for non-invasive detection these cancer signatures in animal models of cancer.

Fluorescent molecular probes include "always on" agents that rely on target binding in tissues or "activatable" agents that report molecular interactions by signal enhancement mechanisms. For "always on" agents, measured fluorescence intensity is

used as a measure of concentration in tissue, similar to nuclear imaging. An example would be a ligand for an up-regulated receptor that bears a near-infrared (NIR) dye such as IS750. This contrast agent has a high affinity for the $\alpha v \beta 3$ integrin receptor (ABIR) and has been used in experimental animal models for imaging tumors. Activatable probes used in fluorescence-based imaging are optically invisible or at least display reduced fluorescence until molecular activation at the disease site. These include enzyme substrates with fluorescent dyes in close proximity which often employ fluorescence resonance energy transfer (FRET) in addition to other quenching mechanisms (Berezin and Achilefu). The enhancement of fluorescence intensity at the site of disease may be great enough in intensity for visualization, but may not totally reflect molecular events within the disease site. Measurement of fluorescence lifetime alteration can be additionally utilized to verify that the observed fluorescence is indeed mediated by a molecular target and not from other processes(Chang et al.).

Fluorescence lifetime is an intrinsic property of fluorescent reporters that is not dependent on concentration but can reflect changes in the environment. Often, the quantum yield is directly related to the fluorescence lifetime: quenching of the fluorescent reporters in an enzyme activatable probe results in lower quantum yield and shortening of the molecular probe's fluorescence lifetime. In the intact FRET pair, the quantum yield and the lifetime of the donor are lower due to the transfer of the excitation energy of the donor to the acceptor (Berezin and Achilefu). Both the quantum yield and the lifetime are subsequently restored to the free dye values after proteolysis leading to an increase in fluorescence intensity and lifetime values of the donor.

Figure 5.1 shows a schematic of the mechanism of action of enzyme activatable probe such as the one used in this study. The donor (D) is a NIR fluorescent reporter attached via a cleavable peptide linker to an acceptor (A) molecule. The absorption properties of the acceptor overlap with the emission properties of the donor attenuating fluorescence and shortening lifetime of the donor. Upon enzyme-mediated hydrolysis, the emission properties of the donor are restored. Previously reported protease activatable molecular FRET probes have shown to improve the tumor detection sensitivity using the intensity signal (Mahmood and Weissleder; Scherer, McIntyre and Matrisian). In this report, we demonstrate that fluorescence lifetime measurement confirms that the observed fluorescence in the syngeneic tumor is, in part, a result of MMP-mediated hydrolysis and subsequent liberation of the proteolytic fragments from close proximity that caused the initial quenching.
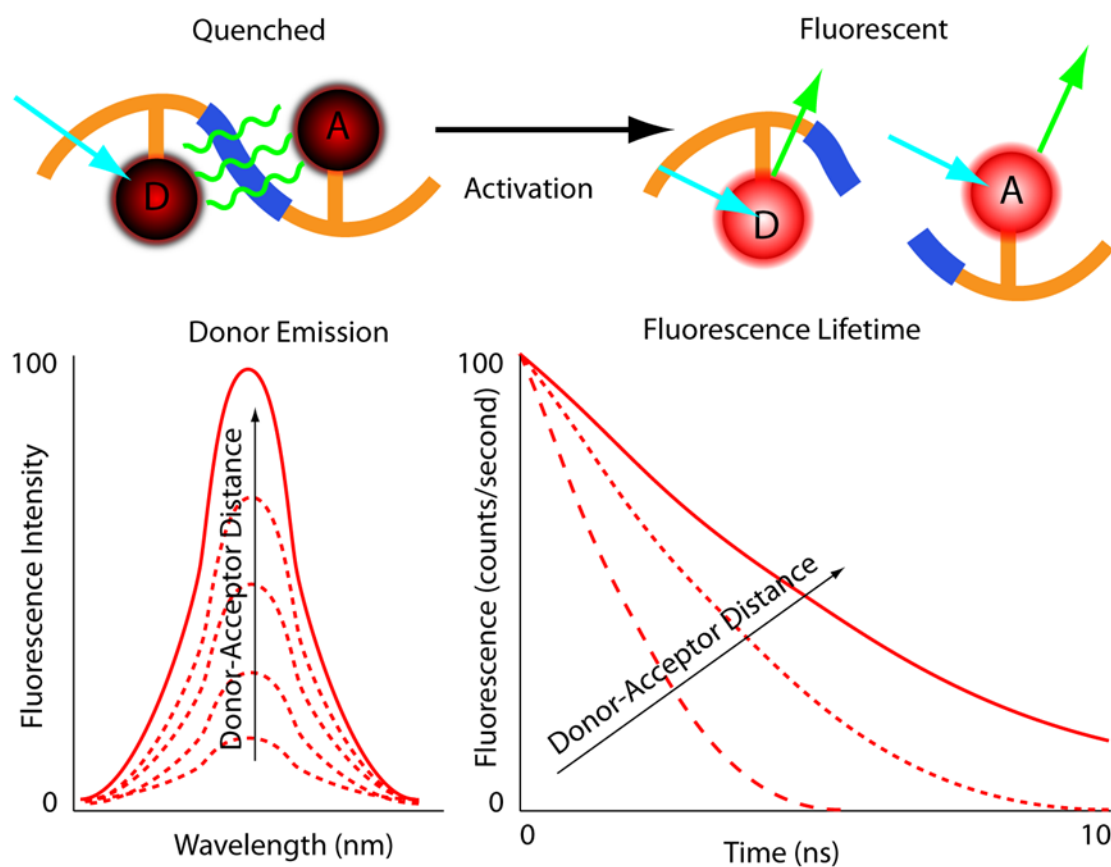
Figure 5.1: Cartoon of FRET-based fluorescent molecular probe and restoration of fluorescence after enzyme mediated hydrolysis of the connecting peptide by protease enzymes. The fluorescence quantum yield and fluorescence lifetime of the donor are increased as the donor and acceptor are separated. In the case of MMP750, the donor and acceptor are identical fluorophores.

Herein, we examined an MMP-sensitive activatable fluorescent construct and an "always-on" ABIR-targeted fluorescent probe in a murine orthotopic breast cancer model using both fluorescence intensity and fluorescence lifetime imaging. While both agents produced good tumor contrast in this model, only the activatable probe showed a significant increase in fluorescence lifetime validating the upregulated enzyme activity due to presence of the tumor. This study demonstrates the potential of fluorescence

lifetime imaging for improving the knowledge of whether the molecular events that are observed are actually target related with FRET-based activatable probes.

5.2 Methods

5.2.1 in vitro Spectroscopy In vitro Spectroscopy

IntegriSense 750 (IS750) and MMPSense 750 FAST (MMP750) were purchased from VisEn Medical (Bedford, MA) and prepared according to manufacturer's instructions. IntegriSense750, MMP750 and MMP-activated MMP750 were diluted in 4% (w/v%) bovine serum albumin (BSA) in phosphate buffered saline (PBS) for spectroscopy. A 20 μL MMP750 solution was then added and incubated at 37 ºC for 3 hr. Activation of MMP750 was confirmed by an increase in fluorescence intensity in cuvettes (ex/em: 740/755-900 nm) of the activated solution relative to the control solution under identical conditions. Fluorescence lifetime (FLT) measurements were performed with using 780 nm NanoLed® (impulse repetition rate 1 MHz) excitation at 90º to the a time-correlated single-photon-counting detector at 820 nm, 26 nm bandpass (Horiba). The fluorescence lifetime was recorded on a 50 ns scale until a peak of 5,000 counts. The instrument response function was obtained using a Rayleigh scatter of Ludox-40 (0.05% in water) in an acrylic transparent cuvette at 780 nm emission. Decay analysis software (DAS6 v6.1; Horiba) was used for lifetime calculations. The goodness of fit was judged by $\chi 2$ values, Durbin–Watson parameters, as well as visual observations of fitted line, residuals, and autocorrelation functions.

5.2.2   In vivo Imaging

All animal studies were performed according to protocols approved by at Washington University School of Medicine Animal Studies Committee for humane care and use of laboratory animals. Luciferase-transfected 4T1 mouse mammary carcinoma cells (4T1luc, Sibtech, Brookfield, CT) cultured in DMEM media were injected subcutaneously into left and right mammary fat pads.

Mice were anesthetized with ketamine (85 mg/kg) and xylazine (15 mg/kg), IP for depilation, intravenous injections and initial post-injection imaging. For extended and subsequent imaging, isoflurane gas (2% v/v in 100% O2) was delivered via nosecone for maintenance of anesthesia. Imaging agents were administered according to manufacturer's recommendations, 1 nmol per mouse, via lateral tail vein of 6-8 week-old female balb/c nude mice (n=3) provided by NCI (NIH).

Time-domain diffuse optical imaging of living mice was performed using the eXplore Optix MX2 system (Advanced Research Technologies, Montreal, Canada) as reported previously (S. Achilefu, S. Bloch, et al.). Briefly, the animals were positioned supine on the heated imaging platform. Pre-injection scans were performed to assess background and autofluorescence signals. Scans were again performed immediately post-injection and at 4-6 hr and 24 hr post-injection. Regions of interest including tumor and non-tumor tissue were raster-scanned at 780 nm excitation with emission detection centered at 830 nm in 1.5 mm steps. Fluorescence intensity and lifetime values were determined by integration or single exponential fitting of the acquired temporal point spread function (TPSF) fluorescence decay curves for each measurement using Optiview software (Advanced Research Technologies). Images were created by mapping each

value to the corresponding location on a white light reference image of the mouse. Mean fluorescence intensity and lifetime values for tumor and non-tumor tissue regions of interest (ROI) for each mouse were selected and reported for analysis.

For reference and ex vivo fluorescence biodistribution assays, images were also captured using the Pearl NIR fluorescence imaging system (LiCor Biosciences, Lincoln, NE). The biodistribution of probes was assessed using the simple method described previously (S. Achilefu, R. B. Dorshow, et al.; Bugaj et al.). At 24 h post-injection, aliquots of blood and pieces of major organs (tumor, heart, kidney, lung, spleen, stomach, intestine, muscle, liver, skin and brain) were harvested and placed on a clear plastic petri dish for imaging. Fluorescence images were acquired as described above. Mean fluorescence intensity was determined for each tissue by ROI analysis and combined for each group for statistical analysis.

5.2.3 Statistical Analysis

Mean fluorescence intensity and FLT values of ROIs for each group were compared using student's t-test with $\alpha = 0.05$ set for significance. Fluorescence biodistribution ROI data were averaged for each organ tissue for IS750 and MMP750 and plotted together for comparison.

5.3 Results

The in vitro activation of MMP750 by the enzyme led to the significant (~2X) increase in fluorescence as shown in Figure 5.2A. Such increase in fluorescence was apparently due to the enzymatic cleavage of the peptide linker leading to the separation of the donor from the acceptor. As expected, a simultaneous increase of the decay slope

(Figure 5.2B) demonstrated an increase in the fluorescence lifetime from 0.58 ns to 0.73

ns, unequivocally demonstrating a reduction in FRET.
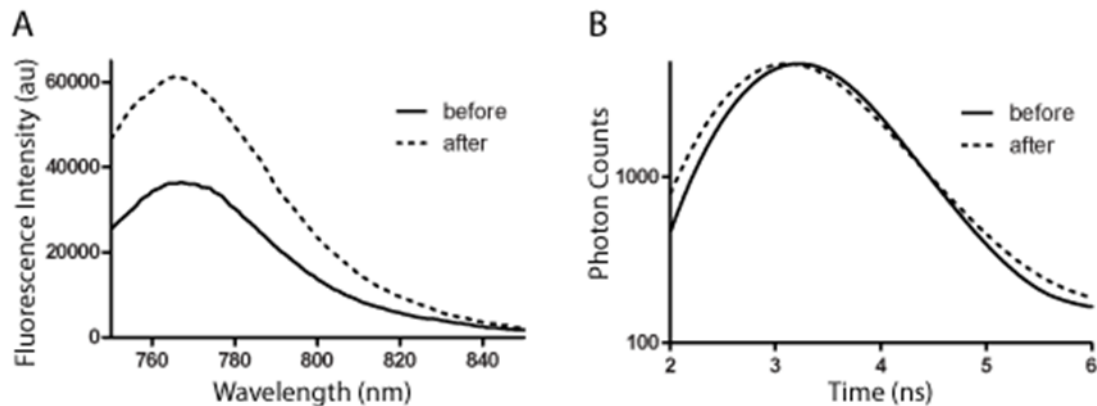

Figure 5.2: (A) Fluorescence steady state spectra of MMP750 before and after enzymatic activation by MMP-2 for 3 hr. The increase in fluorescence intensity confirmed partial activation by enzyme-mediated hydrolysis. (B) Fluorescence decays of MMP750 before and after MMP treatment demonstrating a shift in FLT from 0.58 ns to 0.73 ns due to decreased FRET efficiency after activation.

Having demonstrated the fluorescence lifetime increase in MMP750 upon interaction with MMP and stable fluorescence lifetime of IS750, we administered the probes into small animal tumor models for in vivo imaging. Both IS750 and MMP750 showed tumor-specific uptake in vivo by fluorescence intensity imaging (Figure 5.3A).
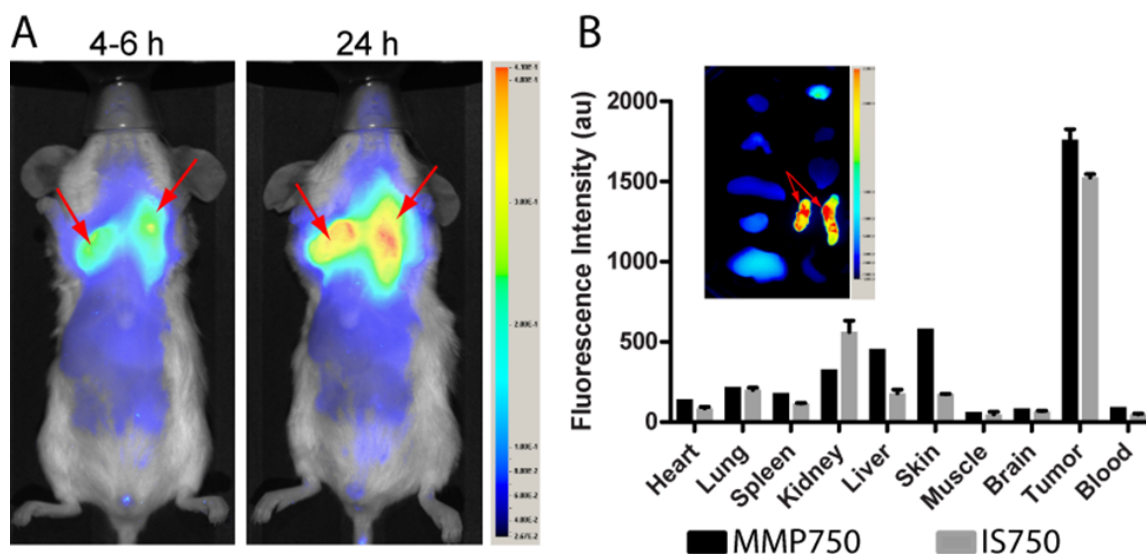
Figure 5.3: (A) Planar fluorescence imaging of mouse with orthotopic breast tumors at 6 and 24 hr after injection of MMP750. (B) Fluorescence biodistribution image (inset) and ROI data for organ tissues 24 hr after injection of either MMP750 or IS750. Arrows indicate 4T1luc tumors.

Fluorescence intensity values were highest for the ABIR-targeted probe immediately after injection in the tumor and non-tumor regions and decreased with time. In contrast, MMP750 was relatively silent after injection and fluorescence signal increased with time, particularly in the tumor regions. Ex vivo tumor fluorescence at 24 h post-injection was higher in the tumor than other tissues (Figure. 5.3B), with 20-fold higher than muscle for both probes (n=3). Autofluorescence and signal from the GI tract was less than 10% of

the signal after molecular probe administration and did not affect the measurement of fluorescence intensities or lifetimes.

Example fluorescence decay curves and nonlinear regression fits are given in Figure. 5.4. Laser power and integration time were automatically adjusted during scanning to ensure adequate photon counts for fitting. The tails of the TPSF curves were fit from 2-6 ns (Figure. 5.4, black lines) for image map construction.
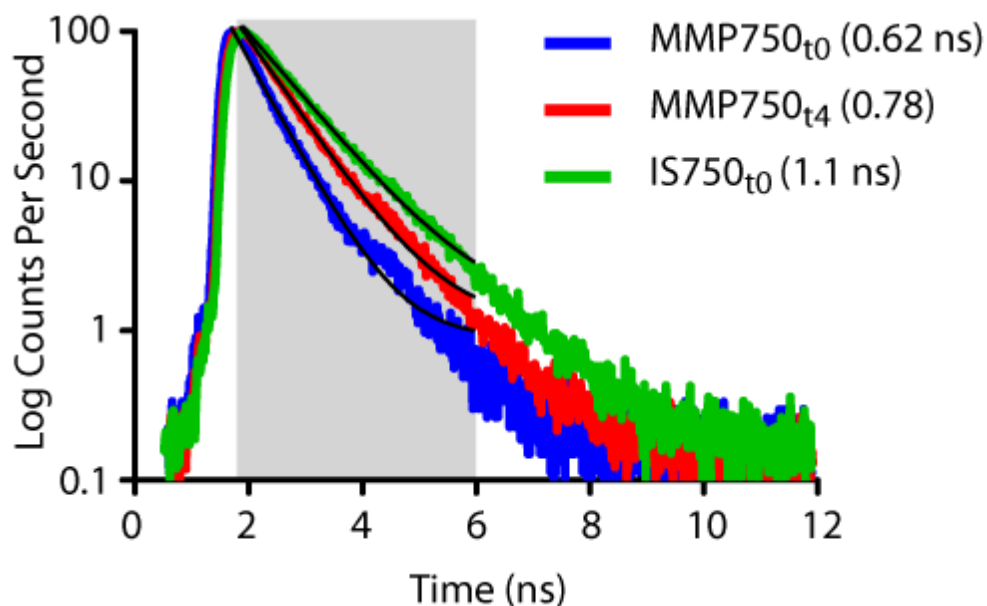
Figure 5.4: Representative normalized fluorescence decay curves (TPSF) in vivo FLT imaging tumor ROIs with single exponential least squares nonlinear regression (black line) from 2 ns to 6 ns (shaded) for MMP750 post-injection (MMP750t0) and 4 h post-injection (MMP750t0) and for IS750 post-injection (IS750t0).
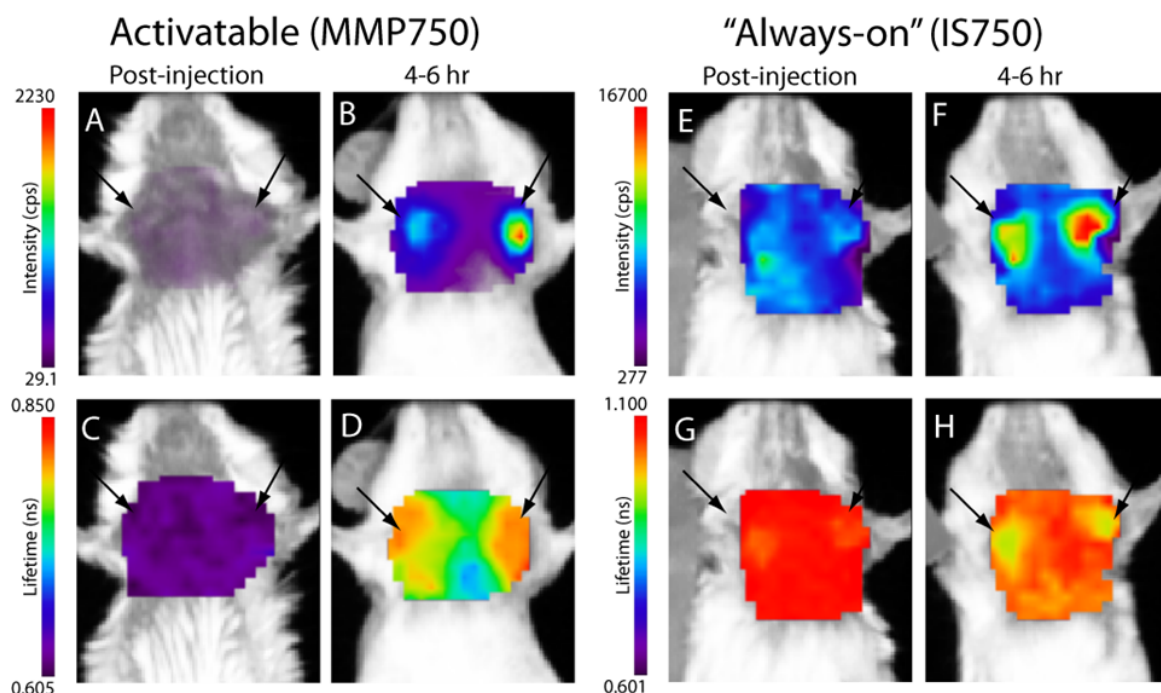
Figure 5.5: Fluorescence intensity and lifetime maps of mice with orthotopic 4T1luc breast tumors immediately after (A and C) and 4-6 hr after (B and D) injection of MMP750. The fluorescence intensity maps show low fluorescence immediately after injection (A) and high signal from the tumors at 4-6 hr after injection (B, arrows). The fluorescence lifetime map is relatively flat with average FLT of 0.63 ns immediately after injection (C). At 4-6 hr after injection, the tumor areas show a higher FLT (0.76 ns) relative to non-tumor regions. Corresponding image maps show different behavior for the "always on" probe. The fluorescence intensity maps show higher signal immediately after injection (E) and from the tumors at 4-6 hr after injection (F, arrows). The fluorescence lifetime map is relatively flat immediately after injection (G). At 4-6 hr after injection, the tumor areas show a shorter FLT relative to non-tumor regions (H).

Intensity maps created by integration of the fluorescence decay curves produced image maps showing good tumor contrast. The fluorescence intensity of MMP750 was very low immediately after injection and increased about 10-fold by 6 hr post-injection (Figure 5.5A and 5.5B, respectively). On the other hand, IS750 fluorescence was high immediately after injection (Figure 5.5E). Fluorescence signal from the tumor regions was significantly higher (P<0.01) for animals in both groups by 6 hour post-injection (Figure 5.5B and 5.5F).

In vivo FLT imaging showed that the measured tumors FLTs for MMP750 were elevated at 4-6 hour post-injection (Figure 5.5D) relative to earlier time points (Figure 5.5C). The FLT maps showed a more diffuse pattern than the intensity maps with increase in FLT in the tumor and peritumoral regions. For IS750, the FLT maps were relatively flat at corresponding time points (Figures 5.5G and 5.5H). FLT values from in vivo ROI analysis are shown in Figure 5.6.
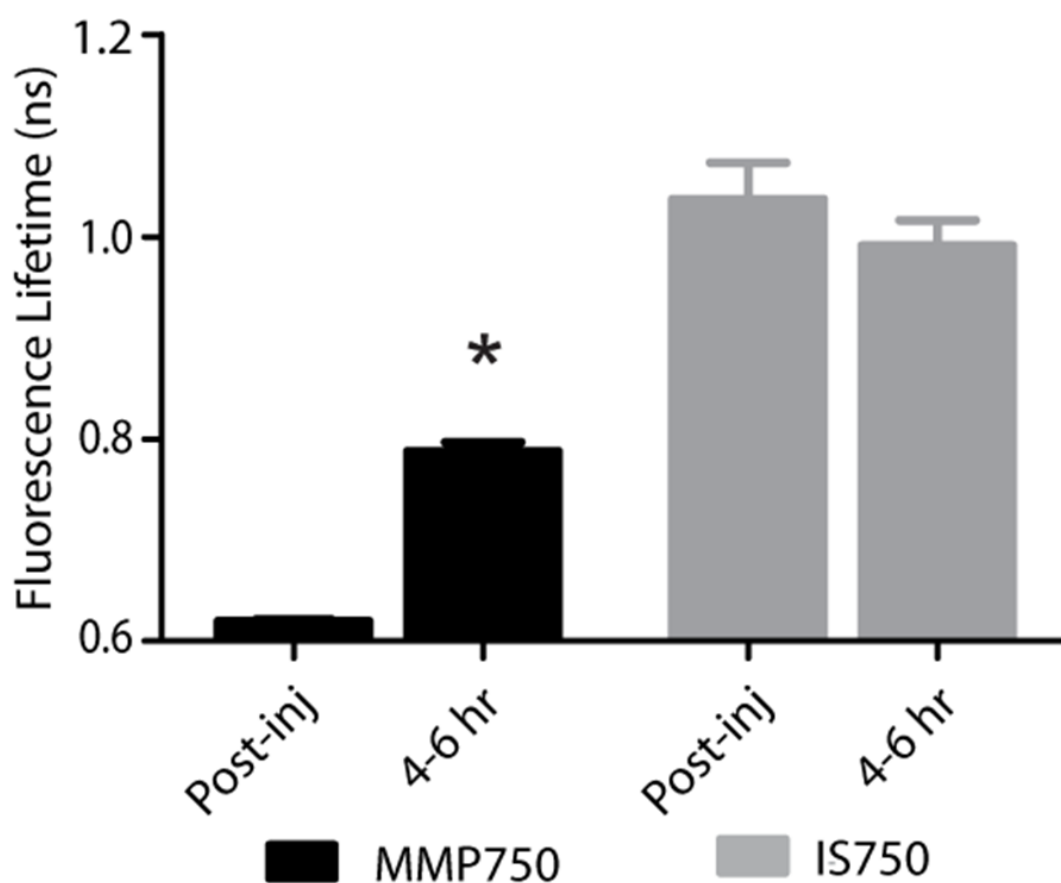
Figure 5.6: Graphical comparison of in vivo FLT values for tumor ROIs immediately after (post-inj) and at 4-6 hour after intravenous administration of NIR fluorescent molecular probes. The measured FLT values for MMPSense750 FAST at 4-6 hr were significantly higher (*P<0.01) than post-injection. FLT values were not significantly different for these time points with IntegriSense750.

For MMP750, the fluorescence lifetime was 0.63+/-0.02 ns immediately post-injection and increased with time. At 4-6 hr post-injection, the FLT had increased significantly (P<0.01) to (0.76+/-0.02 ns) in the tumor region. For IS750, the average FLT values did not change significantly (1.11+/-0.01 ns immediately post-injection and 1.10+/-0.03 ns at 4-6 h post-injection). In the tumor regions, FLT values were slightly lower (1.09+/- 0.03 ns) than non-tumor regions (1.11+/-0.03 ns). Expression of MMP-2 and MMP-9 in the 4T1luc tumor tissues was confirmed by immunohistochemistry (Figure 5.7).
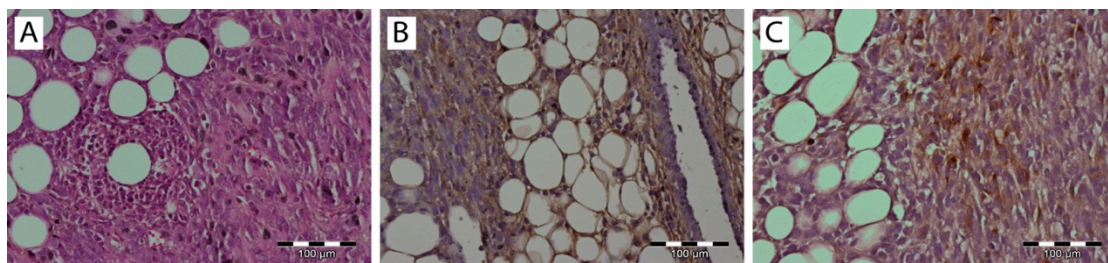
Figure 5.7: H&E stained section of orthotopic 4T1luc tumor tissue (A) and immunohistochemistry for MMP-2 (B) and MMP-9 (C). Brown color indicates areas with high MMP expression in these tumors.

5.4   Discussion

Enzyme activatable fluorescent probes promise higher disease-specific contrast relative to "always on" targeted molecular probes by fluorescence enhancement only within the tissue of interest. The contrast enhancement mechanism of fluorescence activation is unique to optical imaging. Detection of cancer-related enzyme activity using protease-activatable fluorescent probes has high potential for use in staging of primary cancers and detection of metastases.

In the current study, excellent tumor-specific contrast was achieved within 4-6 hr after injection with both the activatable MMP-sensitive and "always on" integrin-targeted NIR fluorescent molecular probes in the orthotopic breast cancer model. The orthotopic breast tumors developed from implanted 4T1 cells syngeneic to the balb/c mouse line are known to produce metastases to the lung and lymph nodes (Tao et al.). This aggressive tumor model is representative of fast-growing and invasive human breast cancer. MMP activity and ABIR expression are biomarkers of breast cancer considered to indicate the aggressiveness of the disease (Daniele et al.; McGowan and Duffy)..

The molecular targets, MMPs and ABIR, are ubiquitously expressed in both target and non-target tissues, although at unequal levels (Roy, Yang and Moses; Sloan et al.). Thus it is not surprising that some fluorescence signal is observed in non-target tissues. Enhancement of signal from the MMP probe was observed in these tissues and results in some fluorescent background rendering the tumor-to-normal contrast produced by this agent almost equal to that of the "always on" fluorescent probe. It is therefore imperative that the activation of this probe be established to distinguish enzyme activity from other modes of contrast including nonspecific accumulation. The activation of

MMP750 was confirmed in this study by the change in FLT that resulted from reduction in FRET as the peptide sequence was cleaved as depicted in Figure. 5.1. FLT imaging provides confirmatory evidence of activation by detecting changes in FRET.

Unsurprisingly, the FLT increase due to activation of MMP750 is seen in the tumor tissue and the surrounding mammary tissue as well (Figure. 5.5D). High MMP activity in the tumor periphery is expected as MMPs are expressed within the tumor stroma and on the invasive front (Roy, Yang and Moses). Thus the FLT map demonstrates the real MMP activity in tissue rather than just accumulation. This study shows that detection of molecular probe activation using FLT-based imaging has significant advantages over other strategies such as inclusion of a spectrally distinct, reference fluorescent reporter either co-injected (Baeten et al.) or as part of the probe construct (Scherer, McIntyre and Matrisian). The use of a single fluorophore as both donor and acceptor facilitates synthesis of activatable probes, providing that adequate quenching is established.

A shortcoming of enzyme-activatable probes, that is not often discussed, is whether there is significant tumoral accumulation of fluorescent proteolytic fragments that were activated distal to the tumor site. Accumulation of the proteolytic fragments might exaggerate the apparent enzyme activity within the tumor tissue. Further studies are needed to assess this type of nonspecific activation and the fates of the probe fragments within the body. Fluorescent probes with improved enzyme selectivity will improve detection and differentiation of cancer-related enzyme activity from other causes such as inflammation (Bremer, Tung and Weissleder). MMP750 resulted in exceptional tumor-specific contrast by fluorescence intensity that was apparently enzyme mediated. Good tumor-normal contrast was obtained within 4-6 hr after injection, a significant

improvement over larger, polymeric activatable probes which require 8-24 hr (Baeten et al.).

5.5   Conclusion

For quantitative measurement of enzyme activity, nonspecific activation must be minimized or other methods developed to separate the level of activation from that of concentration. Here we have presented FLT imaging as one possibility. FLT imaging has the potential for directly assessing changes in FRET due to enzyme activity and is relatively simple and inexpensive relative to other methods such as reference probe co-administration and multimodal imaging. Measurement of the change in FRET upon activation was performed using a single excitation/emission and simple data analysis. FLT imaging using NIR fluorescent FRET probes is a promising technique that has translational potential in regions accessible to optical imaging such as skin, GI and breast cancers. This technique may also be useful for fluorescence guidance of surgery.

References

Achilefu, S. "Lighting up Tumors with Receptor-Specific Optical Molecular Probes." <u>Technol Cancer Res Treat</u> 3.4 (2004): 393-409.

Achilefu, S., et al. "Synergistic Effects of Light-Emitting Probes and Peptides for Targeting and Monitoring Integrin Expression." <u>Proc Natl Acad Sci U S A</u> 102.22 (2005): 7976-81.

Achilefu, S., and R. B. Dorshow. "Dynamic and Continuous Monitoring of Renal and Hepatic Functions with Exogenous Markers." <u>Contrast Agents Ii</u> 222 (2002): 31-72.

Achilefu, S., et al. "Novel Receptor-Targeted Fluorescent Contrast Agents for in Vivo Tumor Imaging." <u>Invest Radiol</u> 35.8 (2000): 479-85.

Achilefu, S., et al. "Synthesis, in Vitro Receptor Binding, and in Vivo Evaluation of Fluorescein and Carbocyanine Peptide-Based Optical Contrast Agents." <u>Journal of Medicinal Chemistry</u> 45.10 (2002): 2003-15.

Achilefu, S., et al. "Development of Contrast Effectors for Optical and Multimodal Imaging of Tumors." <u>Abstracts of Papers of the American Chemical Society</u> 228 (2004): U824-U24.

Achilefu, Samuel I., et al. <u>Optical Molecular Probes for Biomedical Applications : 22 -24 January 2006, San Jose, California, USA</u>. Bellingham, Wash.: SPIE, 2006.

Akers, W., et al. "In Vivo Resolution of Multiexponential Decays of Multiple near-Infrared Molecular Probes by Fluorescence Lifetime-Gated Whole-Body Time-Resolved Diffuse Optical Imaging." <u>Mol Imaging</u> 6.4 (2007): 237-46.

Akers, W.J., and S. Achilefu. "Optical Molecular Imaging." <u>Handbook of Biomedical Optics</u>. Eds. D.A. Boas, C. Pitris and N. Ramanujam: CRC Press, 2010.

Alacam, B., and B. Yazici. "Direct Reconstruction of Pharmacokinetic-Rate Images of Optical Fluorophores from Nir Measurements." <u>IEEE Trans Med Imaging</u> 28.9 (2009): 1337-53.

Alacam, B., et al. "Analysis of Icg Pharmacokinetics in Cancerous Tumors Using Nir Optical Methods." <u>Conf Proc IEEE Eng Med Biol Soc</u> 1 (2005): 62-5.

---. "Analysis of Icg Pharmacokinetics in Cancerous Tumors Using Nir Optical Methods." <u>Conference proceedings : ... Annual International Conference of the IEEE Engineering in Medicine and Biology Society. IEEE Engineering in Medicine and Biology Society. Conference</u> 1 (2005): 62-5.

Alacam, B., et al. "Pharmacokinetic-Rate Images of Indocyanine Green for Breast Tumors Using near-Infrared Optical Methods." <u>Phys Med Biol</u> 53.4 (2008): 837-59.

Alacam, B., et al. "Reconstruction of Spatially Resolved Pharmacokinetic Rate Images of Fluorescence Agents in Fdot." <u>Conf Proc IEEE Eng Med Biol Soc</u> 1 (2006): 5627-30.

Alberini, J. L., et al. "Single Photon Emission Tomography/Computed Tomography (Spet/Ct) and Positron Emission Tomography/Computed Tomography (Pet/Ct) to Image Cancer." <u>Journal of Surgical Oncology</u> 103.6 (2011): 602-06.

Amoozegar, C. B., et al. "Dynamic Contrast-Enhanced Optical Imaging of in Vivo Organ Function." <u>J Biomed Opt</u> 17.9 (2012): 96003-1.

AN. Bashkatov, et al. "In Vivo and in Vitro Study of Control of Rat Skin Optical Properties by Acting of Osmotical Liquid." <u>Proc. SPIE</u> 4224 (2000).

Andersson-Engels, S., et al. "Preliminary Evaluation of Two Fluorescence Imaging Methods for the Detection and the Delineation of Basal Cell Carcinomas of the Skin." <u>Lasers Surg Med</u> 26.1 (2000): 76-82.

Arridge, S. R. "Optical Tomography in Medical Imaging." <u>Inverse Problems</u> 15.2 (1999): R41-R93.

Arridge, S. R., and J. C. Hebden. "Optical Imaging in Medicine: Ii. Modelling and Reconstruction." <u>Phys Med Biol</u> 42.5 (1997): 841-53.

Arridge, S. R., and J. C. Schotland. "Optical Tomography: Forward and Inverse Problems." <u>Inverse Problems</u> 25.12 (2009): -.

Arridge, S. R., and M. Schweiger. "Image Reconstruction in Optical Tomography." <u>Philosophical Transactions of the Royal Society B-Biological Sciences</u> 352.1354 (1997): 717-26.

Austin, T., et al. "Three Dimensional Optical Imaging of Blood Volume and Oxygenation in the Neonatal Brain." <u>NeuroImage</u> 31.4 (2006): 1426-33.

Badizadegan, K., et al. "Spectroscopic Diagnosis and Imaging of Invisible Pre-Cancer." <u>Faraday Discussions</u> 126 (2004): 265-79.

Baeten, J., et al. "In Vivo Investigation of Breast Cancer Progression by Use of an Internal Control." <u>Neoplasia</u> 11.3 (2009): 220-7.

Ballou, B., et al. "Cyanine Fluorochrome-Labeled Antibodies in Vivo: Assessment of Tumor Imaging Using Cy3, Cy5, Cy5.5, and Cy7." <u>Cancer Detection and Prevention</u> 22.3 (1998): 251-57.

Barber, W. C., et al. "Combined Fluorescence and X-Ray Tomography for Quantitative in Vivo Detection of Fluorophore." <u>Technol Cancer Res Treat</u> 9.1 (2010): 45-52.

Berezin, M. Y., and S. Achilefu. "Fluorescence Lifetime Measurements and Biological Imaging." <u>Chemical reviews</u> 110.5: 2641-84.

Berezin, M. Y., et al. "Rational Approach to Select Small Peptide Molecular Probes Labeled with Fluorescent Cyanine Dyes for in Vivo Optical Imaging." <u>Biochemistry</u> 50.13 (2011): 2691-700.

Berezin, M. Y., et al. "Radioactivity-Synchronized Fluorescence Enhancement Using a Radionuclide Fluorescence-Quenched Dye." <u>Journal of the American Chemical Society</u> 131.26 (2009): 9198-+.

Berezin, M. Y., et al. "Engineering Nir Dyes for Fluorescent Lifetime Contrast." <u>Conf Proc IEEE Eng Med Biol Soc</u> 1 (2009): 114-7.

Berezin, M. Y., et al. "Ratiometric Analysis of Fluorescence Lifetime for Probing Binding Sites in Albumin with near-Infrared Fluorescent Molecular Probes." <u>Photochem Photobiol</u> 83.6 (2007): 1371-8.

Bezerra, H. G., et al. "Intracoronary Optical Coherence Tomography: A Comprehensive Review Clinical and Research Applications." <u>Jacc-Cardiovascular Interventions</u> 2.11 (2009): 1035-46.

Bhaumik, S., J. Depuy, and J. Klimash. "Strategies to Minimize Background Autofluorescence in Live Mice During Noninvasive Fluorescence Optical Imaging." <u>Lab Animal</u> 36.8 (2007): 40-43.

Bloch, S., et al. "Whole-Body Fluorescence Lifetime Imaging of a Tumor-Targeted near-Infrared Molecular Probe in Mice." <u>Journal of Biomedical Optics</u> 10.5 (2005): 054003.

Blum, G., et al. "Noninvasive Optical Imaging of Cysteine Protease Activity Using Fluorescently Quenched Activity-Based Probes." <u>Nature Chemical Biology</u> 3.10 (2007): 668-77.

Boas, D. A., et al. "Imaging the Body with Diffuse Optical Tomography." <u>Ieee Signal Processing Magazine</u> 18.6 (2001): 57-75.

Boppart, S. A., et al. "Optical Coherence Tomography: Feasibility for Basic Research and Image-Guided Surgery of Breast Cancer." <u>Breast Cancer Res Treat</u> 84.2 (2004): 85-97.

Bouchard, M. B., et al. "Technical Considerations in Longitudinal Multispectral Small Animal Molecular Imaging." <u>J Biomed Opt</u> 12.5 (2007): -.

Bremer, C., C. H. Tung, and R. Weissleder. "In Vivo Molecular Target Assessment of Matrix Metalloproteinase Inhibition." <u>Nat Med</u> 7.6 (2001): 743-8.

Bugaj, J. E., et al. "Novel Fluorescent Contrast Agents for Optical Imaging of in Vivo Tumors Based on a Receptor-Targeted Dye-Peptide Conjugate Platform." <u>J Biomed Opt</u> 6.2 (2001): 122-33.

Bullok, K. E., et al. "Biochemical and in Vivo Characterization of a Small, Membrane-Permeant, Caspase-Activatable Far-Red Fluorescent Peptide for Imaging Apoptosis." <u>Biochemistry</u> 46.13 (2007): 4055-65.

Bullok, K., and D. Piwnica-Worms. "Synthesis and Characterization of a Small, Membrane-Permeant, Caspase-Activatable Far-Red Fluorescent Peptide for Imaging Apoptosis." <u>Journal of Medicinal Chemistry</u> 48.17 (2005): 5404-7.

Cao, L., and J. Peter. "Bayesian Reconstruction Strategy of Fluorescence-Mediated Tomography Using an Integrated Spect-Ct-Ot System." <u>Physics in Medicine and Biology</u> 55.9 (2010): 2693-708.

Celli, J. P., et al. "Imaging and Photodynamic Therapy: Mechanisms, Monitoring, and Optimization." <u>Chemical reviews</u> 110.5 (2010): 2795-838.

Cerussi, A. E., et al. "Frequent Optical Imaging During Breast Cancer Neoadjuvant Chemotherapy Reveals Dynamic Tumor Physiology in an Individual Patient." <u>Acad Radiol</u> 17.8: 1031-9.

Chance, B., et al. "Time-Resolved Spectroscopy of Hemoglobin and Myoglobin in Resting and Ischemic Muscle." <u>Analytical biochemistry</u> 174.2 (1988): 698-707.

Chang, C. W., et al. "Physiological Fluorescence Lifetime Imaging Microscopy Improves Forster Resonance Energy Transfer Detection in Living Cells." <u>J Biomed Opt</u> 14.6 (2009): 060502.

Cheong, W. F., S. A. Prahl, and A. J. Welch. "A Review of the Optical-Properties of Biological Tissues." <u>Ieee Journal of Quantum Electronics</u> 26.12 (1990): 2166-85.

Choe, R. "Diffuse Optical Tomography & Spectroscopy in Breast Cancer Characterization & Therapy Monitoring at Upenn (Invited Paper)." <u>Conf Proc IEEE Eng Med Biol Soc</u> 1 (2009): 6335-7.

Choe, R., et al. "Diffuse Optical Tomography of Breast Cancer During Neoadjuvant Chemotherapy: A Case Study with Comparison to Mri." <u>Med Phys</u> 32.4 (2005): 1128-39.

Choe, R., et al. "Differentiation of Benign and Malignant Breast Tumors by in-Vivo Three-Dimensional Parallel-Plate Diffuse Optical Tomography." Journal of Biomedical Optics 14.2 (2009): 024020.

Clauss, M. A., and R. K. Jain. "Interstitial Transport of Rabbit and Sheep Antibodies in Normal and Neoplas Tic Tissues." Cancer Research 50.12 (1990): 3487-92.

Cobleigh, M. A., et al. "Multinational Study of the Efficacy and Safety of Humanized Anti-Her2 Monoclonal Antibody in Women Who Have Her2-Overexpressing Metastatic Breast Cancer That Has Progressed after Chemotherapy for Metastatic Disease." J Clin Oncol 17.9 (1999): 2639-48.

Correia, T., et al. "Selection of Regularization Parameter for Optical Topography." Journal of Biomedical Optics 14.3 (2009): 034044.

Cubeddu, R., et al. "Fluorescence Lifetime Imaging of Experimental Tumors in Hematoporphyrin Derivative-Sensitized Mice." Photochem Photobiol 66.2 (1997): 229-36.

Cubeddu, R., et al. "Time-Gated Fluorescence Imaging for the Diagnosis of Tumors in a Murine Model." Photochem Photobiol 57.3 (1993): 480-5.

Cuccia, D. J., et al. "In Vivo Quantification of Optical Contrast Agent Dynamics in Rat Tumors by Use of Diffuse Optical Spectroscopy with Magnetic Resonance Imaging Coregistration." Appl Opt 42.16 (2003): 2940-50.

Culver, J., W. Akers, and S. Achilefu. "Multimodality Molecular Imaging with Combined Optical and Spect/Pet Modalities." Journal of nuclear medicine : official publication, Society of Nuclear Medicine 49.2 (2008): 169-72.

Culver, J. P., et al. "Three-Dimensional Diffuse Optical Tomography in the Parallel Plane Transmission Geometry: Evaluation of a Hybrid Frequency Domain/Continuous Wave Clinical System for Breast Imaging." Med Phys 30.2 (2003): 235-47.

Culver, J. P., et al. "Diffuse Optical Tomography of Cerebral Blood Flow, Oxygenation, and Metabolism in Rat During Focal Ischemia." J Cereb Blood Flow Metab 23.8 (2003): 911-24.

Culver, J. P., et al. "Optimization of Optode Arrangements for Diffuse Optical Tomography: A Singular-Value Analysis." Opt Lett 26.10 (2001): 701-3.

Culver, J. P., et al. "Volumetric Diffuse Optical Tomography of Brain Activity." Opt Lett 28.21 (2003): 2061-3.

Daniele, A., et al. "Expression of Metalloproteinases Mmp-2 and Mmp-9 in Sentinel Lymph Node and Serum of Patients with Metastatic and Non-Metastatic Breast Cancer." Anticancer Res 30.9: 3521-7.

Dehaes, M., et al. "Assessment of the Frequency-Domain Multi-Distance Method to Evaluate the Brain Optical Properties: Monte Carlo Simulations from Neonate to Adult." Biomedical optics express 2.3 (2011): 552-67.

Dehghani, H., et al. "Numerical Modelling and Image Reconstruction in Diffuse Optical Tomography." Philosophical Transactions of the Royal Society a-Mathematical Physical and Engineering Sciences 367.1900 (2009): 3073-93.

Dothager, R. S., et al. "Advances in Bioluminescence Imaging of Live Animal Models." Current Opinion in Biotechnology 20.1 (2009): 45-53.

Drexler, B., J. L. Davis, and G. Schofield. "Diaphanography in the Diagnosis of Breast-Cancer." Radiology 157.1 (1985): 41-44.

Eggebrecht, A. T., et al. "A Quantitative Spatial Comparison of High-Density Diffuse Optical Tomography and Fmri Cortical Mapping." NeuroImage 61.4 (2012): 1120-28.

El-Desoky, A., et al. "Experimental Study of Liver Dysfunction Evaluated by Direct Indocyanine Green Clearance Using near Infrared Spectroscopy." Br J Surg 86.8 (1999): 1005-11.

Erickson, S. J., and A. Godavarty. "Hand-Held Based near-Infrared Optical Imaging Devices: A Review." Medical engineering & physics 31.5 (2009): 495-509.

Even-Sapir, E., Z. Keidar, and R. Bar-Shalom. "Hybrid Imaging (Spect/Ct and Pet/Ct)-Improving the Diagnostic Accuracy of Functional/Metabolic and Anatomic Imaging." Seminars in Nuclear Medicine 39.4 (2009): 264-75.

Falk, G. W. "Autofluorescence Endoscopy." Gastrointest Endosc Clin N Am 19.2 (2009): 209-20.

Fang, Y. H., and R. F. Muzic, Jr. "Spillover and Partial-Volume Correction for Image-Derived Input Functions for Small-Animal 18f-Fdg Pet Studies." J Nucl Med 49.4 (2008): 606-14.

Fingleton, B. "Matrix Metalloproteinase Inhibitors for Cancer Therapy:The Current Situation and Future Prospects." Expert opinion on therapeutic targets 7.3 (2003): 385-97.

Flock, S. T., et al. "Optical-Properties of Intralipid - a Phantom Medium for Light-Propagation Studies." Lasers Surg Med 12.5 (1992): 510-19.

Flusberg, B. A., et al. "Fiber-Optic Fluorescence Imaging." Nature Methods 2.12 (2005): 941-50.

Franceschini, M. A., and D. A. Boas. "Noninvasive Measurement of Neuronal Activity with near-Infrared Optical Imaging." NeuroImage 21.1 (2004): 372-86.

Frangioni, J. V., et al. "Sentinel Lymph Node Mapping with Type-Ii Quantum Dots." Methods in molecular biology (Clifton, N.J.) 374 (2007): 147-59.

Gabor, D. "A New Microscopic Principle." Nature 161.4098 (1948): 777.

Gaudette, R. J., et al. "A Comparison Study of Linear Reconstruction Techniques for Diffuse Optical Tomographic Imaging of Absorption Coefficient." Phys Med Biol 45.4 (2000): 1051-70.

Giancotti, F. G. "Complexity and Specificity of Integrin Signalling." Nature Cell Biology 2.1 (2000): E13-E14.

---. "Integrin Signaling: Specificity and Control of Cell Survival and Cell Cycle Progression." Current Opinion in Cell Biology 9.5 (1997): 691-700.

Giancotti, F. G., and E. Ruoslahti. "Transduction - Integrin Signaling." Science 285.5430 (1999): 1028-32.

Gibson, A., and H. Dehghani. "Diffuse Optical Imaging." Philosophical Transactions of the Royal Society a-Mathematical Physical and Engineering Sciences 367.1900 (2009): 3055-72.

Gibson, A. P., J. C. Hebden, and S. R. Arridge. "Recent Advances in Diffuse Optical Imaging." Phys Med Biol 50.4 (2005): R1-43.

Gioux, S., et al. "Three-Dimensional Surface Profile Intensity Correction for Spatially Modulated Imaging." <u>J Biomed Opt</u> 14.3 (2009): 034045.

Gocheva, V., et al. "Distinct Roles for Cysteine Cathepsin Genes in Multistage Tumorigenesis." <u>Genes & Development</u> 20.5 (2006): 543-56.

Goetz, M., et al. "In Vivo Real-Time Imaging of the Liver with Confocal Endomicroscopy Permits Visualization of the Temporospatial Patterns of Hepatocyte Apoptosis." <u>Am J Physiol Gastrointest Liver Physiol</u> 301.5 (2011): G764-72.

Goiffon, R. J., et al. "Dynamic Noninvasive Monitoring of Renal Function in Vivo by Fluorescence Lifetime Imaging." <u>Journal of Biomedical Optics</u> 14.2 (2009).

Grosenick, D., et al. "Development of a Time-Domain Optical Mammograph and First in Vivo Applications." <u>Appl Opt</u> 38.13 (1999): 2927-43.

Gulsen, G., et al. "Congruent Mri and near-Infrared Spectroscopy for Functional and Structural Imaging of Tumors." <u>Technol Cancer Res Treat</u> 1.6 (2002): 497-505.

Guo, K., et al. "Near Infrared-Fluorescent and Magnetic Resonance Imaging Molecular Probe with High T-1 Relaxivity for in Vivo Multimodal Imaging." <u>Chemical Communications</u> 46.21 (2010): 3705-07.

Guo, W. J., and F. G. Giancotti. "Integrin Signalling During Tumour Progression." <u>Nature Reviews Molecular Cell Biology</u> 5.10 (2004): 816-26.

Haubner, R., et al. "Noninvasive Visualization of the Activated Alphavbeta3 Integrin in Cancer Patients by Positron Emission Tomography and [18f]Galacto-Rgd." <u>PLoS medicine</u> 2.3 (2005): e70.

Hebden, J. C., S. R. Arridge, and D. T. Delpy. "Optical Imaging in Medicine: I. Experimental Techniques." <u>Phys Med Biol</u> 42.5 (1997): 825-40.

Heiskala, J., et al. "Probabilistic Atlas Can Improve Reconstruction from Optical Imaging of the Neonatal Brain." <u>Optics express</u> 17.17 (2009): 14977-92.

Hillman, E. M., et al. "In Vivo Optical Imaging and Dynamic Contrast Methods for Biomedical Research." <u>Philos Transact A Math Phys Eng Sci</u> 369.1955 (2011): 4620-43.

Hillman, E. M., and A. Moore. "All-Optical Anatomical Co-Registration for Molecular Imaging of Small Animals Using Dynamic Contrast." <u>Nat Photonics</u> 1.9 (2007): 526-30.

Himelstein, B. P., et al. "Metalloproteinases in Tumor Progression: The Contribution of Mmp-9." <u>Invasion & metastasis</u> 14.1-6: 246-58.

Hoekstra, C. J., O. S. Hoekstra, and A. A. Lammertsma. "On the Use of Image-Derived Input Functions in Oncological Fluorine-18 Fluorodeoxyglucose Positron Emission Tomography Studies." <u>Eur J Nucl Med</u> 26.11 (1999): 1489-92.

Hojo, T., et al. "Evaluation of Sentinel Node Biopsy by Combined Fluorescent and Dye Method and Lymph Flow for Breast Cancer." <u>Breast</u> 19.3 (2010): 210-13.

Hsiung, P. L., et al. "Detection of Colonic Dysplasia in Vivo Using a Targeted Heptapeptide and Confocal Microendoscopy." <u>Nat Med</u> 14.4 (2008): 454-58.

Huang, D., et al. "Optical Coherence Tomography." <u>Science</u> 254.5035 (1991): 1178-81.

Hyde, D., et al. "A Statistical Approach to Inverting the Born Ratio." <u>Ieee Transactions on Medical Imaging</u> 26.7 (2007): 893-905.

Imaeda, Hiroyuki, et al. "Autofluorescence Videoendoscopy System Using the Safe-3000 for Assessing Superficial Gastric Neoplasia." Blackwell Publishing Asia. 706-11. Vol. 25.

Intes, X., et al. "Projection Access Order in Algebraic Reconstruction Technique for Diffuse Optical Tomography." Physics in Medicine and Biology 47.1 (2002): N1-N10.

Intes, X., et al. "In Vivo Continuous-Wave Optical Breast Imaging Enhanced with Indocyanine Green." Med Phys 30.6 (2003): 1039-47.

Janin, A., et al. "Cd95 Engagement Induces Disseminated Endothelial Cell Apoptosis in Vivo: Immunopathologic Implications." Blood 99.8 (2002): 2940-7.

Joseph, D. K., et al. "Diffuse Optical Tomography System to Image Brain Activation with Improved Spatial Resolution and Validation with Functional Magnetic Resonance Imaging." Applied Optics 45.31 (2006): 8142-51.

Kapteijn, B. A., et al. "Validation of Gamma Probe Detection of the Sentinel Node in Melanoma." Journal of nuclear medicine : official publication, Society of Nuclear Medicine 38.3 (1997): 362-6.

Kimura, S., et al. "Indocyanine Green Elimination Rate Detects Hepatocellular Dysfunction Early in Septic Shock and Correlates with Survival." Crit Care Med 29.6 (2001): 1159-63.

Knappe, V., F. Frank, and E. Rohde. "Principles of Lasers and Biophotonic Effects." Photomedicine and Laser Surgery 22.5 (2004): 411-17.

Koyama, Y., et al. "Spectral Fluorescence Molecular Imaging of Lung Metastases Targeting Her2/Neu." Clin Cancer Res 13.10 (2007): 2936-45.

Kukreti, S., et al. "Characterization of Metabolic Differences between Benign and Malignant Tumors: High-Spectral-Resolution Diffuse Optical Spectroscopy." Radiology 254.1 (2010): 277-84.

Kukreti, S., et al. "Intrinsic near-Infrared Spectroscopic Markers of Breast Tumors." Dis Markers 25.6 (2008): 281-90.

Laforest, R., et al. "Measurement of Input Functions in Rodents: Challenges and Solutions." Nucl Med Biol 32.7 (2005): 679-85.

Lee, B. T., et al. "The Flare Intraoperative near-Infrared Fluorescence Imaging System: A First-in-Human Clinical Trial in Perforator Flap Breast Reconstruction." Plastic and reconstructive surgery 126.5 (2010): 1472-81.

Lee, H., et al. "Complementary Optical and Nuclear Imaging of Caspase-3 Activity Using Combined Activatable and Radio-Labeled Multimodality Molecular Probe." Journal of Biomedical Optics 14.4 (2009): 040507.

Leff, D. R., et al. "Diffuse Optical Imaging of the Healthy and Diseased Breast: A Systematic Review." Breast Cancer Res Treat 108.1 (2008): 9-22.

Li, A., et al. "Tomographic Optical Breast Imaging Guided by Three-Dimensional Mammography." Applied Optics 42.25 (2003): 5181-90.

Li, C. Q., et al. "Simultaneous Pet and Multispectral 3-Dimensional Fluorescence Optical Tomography Imaging System." Journal of Nuclear Medicine 52.8 (2011): 1268-75.

Licha, K., et al. "Synthesis, Characterization, and Biological Properties of Cyanine-Labeled Somatostatin Analogues as Receptor-Targeted Fluorescent Probes." Bioconjug Chem 12.1 (2001): 44-50.

Licha, K., et al. "Hydrophilic Cyanine Dyes as Contrast Agents for near-Infrared Tumor Imaging: Synthesis, Photophysical Properties and Spectroscopic in Vivo Characterization." Photochem Photobiol 72.3 (2000): 392-8.

Liu, X., et al. "Imaging of Indocyanine Green Perfusion in Mouse Liver with Fluorescence Diffuse Optical Tomography." Ieee Transactions on Biomedical Engineering 58.8 (2011).

Ludwig, J. A., and J. N. Weinstein. "Biomarkers in Cancer Staging, Prognosis and Treatment Selection." Nature Reviews Cancer 5.11 (2005): 845-56.

Mahmood, U., and R. Weissleder. "Near-Infrared Optical Imaging of Proteases in Cancer." Molecular Cancer Therapeutics 2.5 (2003): 489-96.

Marquez, G., et al. "Anisotropy in the Absorption and Scattering Spectra of Chicken Breast Tissue." Applied Optics 37.4 (1998): 798-804.

McGowan, P. M., and M. J. Duffy. "Matrix Metalloproteinase Expression and Outcome in Patients with Breast Cancer: Analysis of a Published Database." Ann Oncol 19.9 (2008): 1566-72.

McIntyre, J. O., and L. M. Matrisian. "Molecular Imaging of Proteolytic Activity in Cancer." Journal of cellular biochemistry 90.6 (2003): 1087-97.

---. "Optical Proteolytic Beacons for in Vivo Detection of Matrix Metalloproteinase Activity." Methods in molecular biology (Clifton, N.J.) 539 (2009): 155-74.

McIntyre, J. O., R. L. Scherer, and L. M. Matrisian. "Near-Infrared Optical Proteolytic Beacons for in Vivo Imaging of Matrix Metalloproteinase Activity." Methods in molecular biology (Clifton, N.J.) 622: 279-304.

Milstein, A. B., K. J. Webb, and C. A. Bouman. "Estimation of Kinetic Model Parameters in Fluorescence Optical Diffusion Tomography." Journal of the Optical Society of America a-Optics Image Science and Vision 22.7 (2005): 1357-68.

Monici, M. "Cell and Tissue Autofluorescence Research and Diagnostic Applications." Biotechnology annual review 11 (2005): 227-56.

Monsees, B., J. M. Destouet, and W. G. Totty. "Light Scanning Versus Mammography in Breast Cancer Detection." Radiology 163.2 (1987): 463-5.

Nahrendorf, M., et al. "Hybrid Pet-Optical Imaging Using Targeted Probes." Proceedings of the National Academy of Sciences of the United States of America 107.17 (2010): 7910-15.

Nicholson, S., et al. "Epidermal Growth Factor Receptor (Egfr); Results of a 6 Year Follow-up Study in Operable Breast Cancer with Emphasis on the Node Negative Subgroup." Br J Cancer 63.1 (1991): 146-50.

Niedre, M. J., G. M. Turner, and V. Ntziachristos. "Time-Resolved Imaging of Optical Coefficients through Murine Chest Cavities." Journal of biomedical optics 11.6 (2006): 064017.

Niemz, Markolf H. Laser-Tissue Interactions: Fundamentals and Applications. 3rd enlarged ed. ed: Springer, 2003.

Nilsson, A. M., R. Berg, and S. Andersson-Engels. "Measurements of the Optical Properties of Tissue in Conjunction with Photodynamic Therapy." <u>Applied Optics</u> 34.21 (1995): 4609-19.

Nothdurft, R. E., et al. "In Vivo Fluorescence Lifetime Tomography." <u>Journal of Biomedical Optics</u> 14.2 (2009): 024004.

Ntziachristos, V., C. Bremer, and R. Weissleder. "Fluorescence Imaging with near-Infrared Light: New Technological Advances That Enable in Vivo Molecular Imaging." <u>Eur Radiol</u> 13.1 (2003): 195-208.

Ntziachristos, V., et al. "Fluorescence Molecular Tomography Resolves Protease Activity in Vivo." <u>Nat Med</u> 8.7 (2002): 757-60.

Ntziachristos, V., et al. "Planar Fluorescence Imaging Using Normalized Data." <u>J Biomed Opt</u> 10.6 (2005): -.

Ntziachristos, V., and R. Weissleder. "Charge-Coupled-Device Based Scanner for Tomography of Fluorescent near-Infrared Probes in Turbid Media." <u>Med Phys</u> 29.5 (2000): 803-09.

---. "Experimental Three-Dimensional Fluorescence Reconstruction of Diffuse Media by Use of a Normalized Born Approximation." <u>Optics Letters</u> 26.12 (2001): 893-5.

---. "Experimental Three-Dimensional Fluorescence Reconstruction of Diffuse Media by Use of a Normalized Born Approximation." <u>Opt Lett</u> 26.12 (2001): 893-5.

Ntziachristos, V., et al. "Mri-Guided Diffuse Optical Spectroscopy of Malignant and Benign Breast Lesions." <u>Neoplasia</u> 4.4 (2002): 347-54.

O'Neill, K., et al. "Bioluminescent Imaging: A Critical Tool in Pre-Clinical Oncology Research." <u>Journal of Pathology</u> 220.3 (2010): 317-27.

Odonkor, C. A., and S. Achilefu. "Differential Activity of Caspase-3 Regulates Susceptibility of Lung and Breast Tumor Cell Lines to Paclitaxel." <u>Open Biochem J</u> 2 (2008): 121-8.

---. "Modulation of Effector Caspase Cleavage Determines Response of Breast and Lung Tumor Cell Lines to Chemotherapy." <u>Cancer Invest</u> 27.4 (2009): 417-29.

Ogasawara, J., et al. "Lethal Effect of the Anti-Fas Antibody in Mice." <u>Nature</u> 364.6440 (1993): 806-9.

Ott, P. "Hepatic Elimination of Indocyanine Green with Special Reference to Distribution Kinetics and the Influence of Plasma Protein Binding." <u>Pharmacology & Toxicology</u> 83 (1998): 7-48.

Palmer, G. M., et al. "Non-Invasive Monitoring of Intra-Tumor Drug Concentration and Therapeutic Response Using Optical Spectroscopy." <u>Journal of Controlled Release</u> 142.3 (2010): 457-64.

Patterson, M. S., B. Chance, and B. C. Wilson. "Time Resolved Reflectance and Transmittance for the Non-Invasive Measurement of Tissue Optical Properties." <u>Appl Opt</u> 28.12 (1989): 2331-6.

Patwardhan, S., et al. "Time-Dependent Whole-Body Fluorescence Tomography of Probe Bio-Distributions in Mice." <u>Opt Express</u> 13.7 (2005): 2564-77.

Patwardhan, S. V., et al. "Quantitative Small Animal Fluorescence Tomography Using an Ultrafast Gated Image Intensifier." <u>Conf Proc IEEE Eng Med Biol Soc</u> 1 (2006): 2675-8.

Patwardhan, S. V., et al. "Time-Dependent Whole-Body Fluorescence Tomography of Probe Bio-Distributions in Mice." <u>Opt Express</u> 13.7 (2005): 2564-77.

Patwardhan, S. V., and J. P. Culver. "Quantitative Diffuse Optical Tomography for Small Animals Using an Ultrafast Gated Image Intensifier." <u>J Biomed Opt</u> 13.1 (2008): 011009.

---. "Quantitative Diffuse Optical Tomography for Small Animals Using an Ultrafast Gated Image Intensifier." <u>Journal of Biomedical Optics</u> 13.1 (2008): 011009.

Paulick, M. G., and M. Bogyo. "Application of Activity-Based Probes to the Study of Enzymes Involved in Cancer Progression." <u>Current opinion in genetics & development</u> 18.1 (2008): 97-106.

Pogue, B. W., et al. "Fluorescence Imaging in Vivo: Raster Scanned Point-Source Imaging Provides More Accurate Quantification Than Broad Beam Geometries." <u>Technol Cancer Res Treat</u> 3.1 (2004): 15-21.

Pogue, B. W., et al. "Quantitative Hemoglobin Tomography with Diffuse near-Infrared Spectroscopy: Pilot Results in the Breast." <u>Radiology</u> 218.1 (2001): 261-6.

Proulx, S. T., et al. "Quantitative Imaging of Lymphatic Function with Liposomal Indocyanine Green." <u>Cancer Research</u> 70.18 (2010): 7053-62.

Ramanujam, N., et al. "Fluorescence Spectroscopy: A Diagnostic Tool for Cervical Intraepithelial Neoplasia (Cin)." <u>Gynecologic oncology</u> 52.1 (1994): 31-8.

Raymond, S. B., et al. "Lifetime-Based Tomographic Multiplexing." <u>Journal of Biomedical Optics</u> 15.4: 046011.

Reynolds, J. S., et al. "Imaging of Spontaneous Canine Mammary Tumors Using Fluorescent Contrast Agents." <u>Photochem Photobiol</u> 70.1 (1999): 87-94.

Richards-Kortum, R., and E. Sevick-Muraca. "Quantitative Optical Spectroscopy for Tissue Diagnosis." <u>Annu Rev Phys Chem</u> 47 (1996): 555-606.

Ross, J. S., and J. A. Fletcher. "Her-2/Neu (C-Erb-B2) Gene and Protein in Breast Cancer." <u>Am J Clin Pathol</u> 112.1 Suppl 1 (1999): S53-67.

Ross, J. S., et al. "Her-2/Neu Testing in Breast Cancer." <u>Am J Clin Pathol</u> 120 Suppl (2003): S53-71.

Ross, J. S., et al. "Targeted Therapy in Breast Cancer: The Her-2/Neu Gene and Protein." <u>Mol Cell Proteomics</u> 3.4 (2004): 379-98.

Roy, R., J. Yang, and M. A. Moses. "Matrix Metalloproteinases as Novel Biomarkers and Potential Therapeutic Targets in Human Cancer." <u>J Clin Oncol</u> 27.31 (2009): 5287-97.

Rzyman, W., et al. "Blue-Dye Intraoperative Sentinel Lymph Node Mapping in Early Non-Small Cell Lung Cancer." <u>European journal of surgical oncology : the journal of the European Society of Surgical Oncology and the British Association of Surgical Oncology</u> 32.4 (2006): 462-5.

Sampath, L., et al. "Detection of Cancer Metastases with a Dual-Labeled near-Infrared/Positron Emission Tomography Imaging Agent." <u>Transl Oncol</u> 3.5 (2010): 307-217.

Sampath, L., W. Wang, and E. M. Sevick-Muraca. "Near Infrared Fluorescent Optical Imaging for Nodal Staging." <u>J Biomed Opt</u> 13.4 (2008): 041312.

Scherer, R. L., J. O. McIntyre, and L. M. Matrisian. "Imaging Matrix Metalloproteinases in Cancer." <u>Cancer Metastasis Rev</u> 27.4 (2008): 679-90.

Schweiger, M., et al. "The Finite Element Method for the Propagation of Light in Scattering Media: Boundary and Source Conditions." Med Phys 22.11 (1995): 1779-92.

Schweiger, M., S. R. Arridge, and I. Nissila. "Gauss-Newton Method for Image Reconstruction in Diffuse Optical Tomography." Phys Med Biol 50.10 (2005): 2365-86.

Schweiger, M., A. Gibson, and S. R. Arridge. "Computational Aspects of Diffuse Optical Tomography." Computing in Science & Engineering 5.6 (2003): 33-41.

Seifalian, A. M., et al. "Effects of Hepatic Ischaemia/Reperfusion Injury in a Rabbit Model of Indocyanine Green Clearance." Clin Sci (Lond) 102.5 (2002): 579-86.

Sevick-Muraca, E. M., et al. "Imaging of Lymph Flow in Breast Cancer Patients after Microdose Administration of a near-Infrared Fluorophore: Feasibility Study." Radiology 246.3 (2008): 734-41.

Sharma, R., et al. "Quantitative Imaging of Lymph Function." Am J Physiol Heart Circ Physiol 292.6 (2007): H3109-18.

Sharma, R., et al. "New Horizons for Imaging Lymphatic Function." Lymphatic Continuum Revisited 1131 (2008): 13-36.

Sidransky, D. "Emerging Molecular Markers of Cancer." Nature Reviews Cancer 2.3 (2002): 210-19.

Sloan, E. K., et al. "Tumor-Specific Expression of Alphavbeta3 Integrin Promotes Spontaneous Metastasis of Breast Cancer to Bone." Breast Cancer Res 8.2 (2006): R20.

Sokolov, K., M. Follen, and R. Richards-Kortum. "Optical Spectroscopy for Detection of Neoplasia." Current opinion in chemical biology 6.5 (2002): 651-8.

Solomon, M., et al. "Detection of Enzyme Activity in Orthotopic Murine Breast Cancer by Fluorescence Lifetime Imaging Using a Fluorescence Resonance Energy Transfer-Based Molecular Probe." J Biomed Opt 16.6 (2011): 066019.

Solomon, M., et al. "Video-Rate Fluorescence Diffuse Optical Tomography for in Vivo Sentinel Lymph Node Imaging." Biomed Opt Express 2.12 (2011): 3267-77.

Solomon, Metasebya, et al. "Video-Rate Fluorescence Diffuse Optical Tomography for in Vivo Sentinel Lymph Node Imaging." Biomed. Opt. Express 2.12 (2011): 3267-77.

Srinivasan, V., H. C. Liu, and M. Halioua. "Automated Phase-Measuring Profilometry of 3-D Diffuse Objects." Appl Opt 23.18 (1984): 3105.

Swanson, E. A., et al. "In-Vivo Retinal Imaging by Optical Coherence Tomography." Opt Lett 18.21 (1993): 1864-66.

Takeda, M., and K. Mutoh. "Fourier Transform Profilometry for the Automatic Measurement of 3-D Object Shapes." Appl Opt 22.24 (1983): 3977.

Tao, K., et al. "Imagable 4t1 Model for the Study of Late Stage Breast Cancer." BMC Cancer 8 (2008): 228.

Tearney, G. J., et al. "In Vivo Endoscopic Optical Biopsy with Optical Coherence Tomography." Science 276.5321 (1997): 2037-9.

Tromberg, B. J., et al. "Assessing the Future of Diffuse Optical Imaging Technologies for Breast Cancer Management." Med Phys 35.6 (2008): 2443-51.

Troyan, S. L., et al. "The Flare Intraoperative near-Infrared Fluorescence Imaging System: A First-in-Human Clinical Trial in Breast Cancer Sentinel Lymph Node Mapping." <u>Annals of Surgical Oncology</u> 16.10 (2009): 2943-52.

Tuchin, V.V. <u>Tissue Optics: Light Scattering Methods and Instruments for Medical Diagnosis</u>. 2nd ed. Vol. Vol. PM166: SPIE Publications, 2007.

Tuttle, T. M., et al. "Subareolar Injection of Tc-99m Facilitates Sentinel Lymph Node Identification." <u>Annals of Surgical Oncology</u> 9.1 (2002): 77-81.

van den Hoff, J. "Principles of Quantitative Positron Emission Tomography." <u>Amino Acids</u> 29.4 (2005): 341-53.

van der Weerdt, A. P., et al. "Image-Derived Input Functions for Determination of Mrglu in Cardiac (18)F-Fdg Pet Scans." <u>J Nucl Med</u> 42.11 (2001): 1622-9.

Vishwanath, K., et al. "Quantitative Optical Spectroscopy Can Identify Long-Term Local Tumor Control in Irradiated Murine Head and Neck Xenografts." <u>Journal of Biomedical Optics</u> 14.5 (2009): 054051.

Vishwanath, K., et al. "Using Optical Spectroscopy to Longitudinally Monitor Physiological Changes within Solid Tumors." <u>Neoplasia</u> 11.9 (2009): 889-900.

Vo-Dinh, Tuan. <u>Biomedical Photonics Handbook</u>. CRC Press LLC, 2003.

VoDinh, T., et al. "Laser-Induced Differential Fluorescence for Cancer Diagnosis without Biopsy." <u>Applied Spectroscopy</u> 51.1 (1997): 58-63.

Vogel, C., et al. "First-Line, Single-Agent Herceptin(Trastuzumab) in Metastatic Breast Cancer: A Preliminary Report." <u>Eur J Cancer</u> 37 Suppl 1 (2001): S25-9.

Wang, L., S. L. Jacques, and L. Zheng. "Mcml--Monte Carlo Modeling of Light Transport in Multi-Layered Tissues." <u>Comput Methods Programs Biomed</u> 47.2 (1995): 131-46.

Wang, Lihong V. <u>Photoacoustic Imaging and Spectroscopy</u>. Optical Science and Engineering. Boca Raton: CRC, 2009.

Wang, Lihong V., and Hsin-I Wu. <u>Biomedical Optics: Principles and Imaging</u>. 1st ed: Wiley-Interscience, 2007.

Wax, Adam, and Vadim Backman. <u>Biomedical Applications of Light Scattering</u>. McGraw-Hill, 2010.

Weissleder, R., et al. "In Vivo Imaging of Tumors with Protease-Activated near-Infrared Fluorescent Probes." <u>Nat Biotechnol</u> 17.4 (1999): 375-8.

Welsher, K., S. P. Sherlock, and H. Dai. "Deep-Tissue Anatomical Imaging of Mice Using Carbon Nanotube Fluorophores in the Second near-Infrared Window." <u>Proc Natl Acad Sci U S A</u> 108.22 (2011): 8943-8.

White, B. R., et al. "Resting-State Functional Connectivity in the Human Brain Revealed with Diffuse Optical Tomography." <u>NeuroImage</u> 47.1 (2009): 148-56.

Willemsen, A. T., and J. van den Hoff. "Fundamentals of Quantitative Pet Data Analysis." <u>Curr Pharm Des</u> 8.16 (2002): 1513-26.

Wu, H. M., et al. "Factor Analysis for Extraction of Blood Time-Activity Curves in Dynamic Fdg-Pet Studies." <u>J Nucl Med</u> 36.9 (1995): 1714-22.

Wu, H. M., et al. "Derivation of Input Function from Fdg-Pet Studies in Small Hearts." <u>J Nucl Med</u> 37.10 (1996): 1717-22.

Xu, M. H., and L. H. V. Wang. "Photoacoustic Imaging in Biomedicine." <u>Review of Scientific Instruments</u> 77.4 (2006): -.

Xu, R. X., and S. P. Povoski. "Diffuse Optical Imaging and Spectroscopy for Cancer." Expert review of medical devices 4.1 (2007): 83-95.

Yalavarthy, P. K., et al. "Implementation of a Computationally Efficient Least-Squares Algorithm for Highly under-Determined Three-Dimensional Diffuse Optical Tomography Problems." Med Phys 35.5 (2008): 1682-97.

Yalavarthy, P. K., et al. "Weight-Matrix Structured Regularization Provides Optimal Generalized Least-Squares Estimate in Diffuse Optical Tomography." Med Phys 34.6 (2007): 2085-98.

Ye, Y., et al. "Design, Synthesis, and Evaluation of near Infrared Fluorescent Multimeric Rgd Peptides for Targeting Tumors." Journal of Medicinal Chemistry 49.7 (2006): 2268-75.

Yeh, A. T., et al. "Imaging Wound Healing Using Optical Coherence Tomography and Multiphoton Microscopy in an in Vitro Skin-Equivalent Tissue Model." Journal of Biomedical Optics 9.2 (2004): 248-53.

Zeff, B. W., et al. "Retinotopic Mapping of Adult Human Visual Cortex with High-Density Diffuse Optical Tomography." Proc Natl Acad Sci U S A 104.29 (2007): 12169-74.

Zhang, Q., et al. "Coregistered Tomographic X-Ray and Optical Breast Imaging: Initial Results." J Biomed Opt 10.2 (2005): -.

Zhang, Z., et al. "Activatable Molecular Systems Using Homologous near-Infrared Fluorescent Probes for Monitoring Enzyme Activities in Vitro, in Cellulo, and in Vivo." Mol Pharm (2009).

Zhang, Z. R., and S. Achilefu. "Spectral Properties of Pro-Multimodal Imaging Agents Derived from a Nir Dye and a Metal Chelator." Photochemistry and Photobiology 81.6 (2005): 1499-504.

Zhang, Z. R., et al. "Monomolecular Multimodal Fluorescence-Radioisotope Imaging Agents." Bioconjug Chem 16.5 (2005): 1232-39.

Zhu, C., et al. "Diagnosis of Breast Cancer Using Fluorescence and Diffuse Reflectance Spectroscopy: A Monte-Carlo-Model-Based Approach." Journal of Biomedical Optics 13.3 (2008): 034015.

Zhu, Q., et al. "Imager That Combines near-Infrared Diffusive Light and Ultrasound." Opt Lett 24.15 (1999): 1050-52.

Zhu, Quing, et al. "Benign Versus Malignant Breast Masses: Optical Differentiation with Us-Guided Optical Imaging Reconstruction 10.1148/Radiol.2371041236." Radiology 237.1 (2005): 57-66.